

Unsaturated characteristics of ballast fouling materials and fouled ballast

by

Robert R. Sherwood

B.S., Kansas State University, 2017

A THESIS

submitted in partial fulfillment of the requirements for the degree

MASTER OF SCIENCE

Department of Civil Engineering  
Carl R. Ice College of Engineering

KANSAS STATE UNIVERSITY  
Manhattan, Kansas

2020

Approved by:

Major Professor  
Stacey Kulesza

# **Copyright**

© Robert Sherwood 2020.

## **Abstract**

Fouling reduces ballast drainage and strength. Without detection and remediation, track geometry degrades and risk of train derailment increases; therefore, fouling must be managed. There is limited research about the characteristics of fouled ballast needed to improve detection and remediation methods. This research specifically focused on the water holding capacity of fouled ballast. Soil water characteristic curves (SWCCs) were measured on 14 ballast fouling specimens using a 66.0 mm tall 61.8 mm diameter flow cell and using the transient water release and imbibition method (TRIM). SWCCs were also calculated for 21 fouled ballast specimens using the Bouwer-Rice Large Particle Correction Procedure. Lastly, SWCCs were measured on two fouled ballast specimens (with aggregate sizes up 42.5 mm, nominal diameter) using a custom 178 mm tall 255 mm diameter flow cell and the TRIM. SWCCs of the ballast fouling specimens show that the presence of coal fines greatly influences water retention. Calculated results for the fouled ballast specimens show that the type of fouling material and the quantity of fouling material in a fouled ballast layer dominate several engineering properties of the layer (e.g., hydraulic conductivity and pore water content). The results in the custom larger cell validate the novel experimental testing plan with aggregates to support measuring SWCCs of fouled ballast. This research is the first step in characterizing these materials to support in situ identification of fouled ballast using ground penetrating radar (GPR). Future work correlating dielectric measurements to SWCC measurements of fouled ballast specimens is hypothesized to help uncouple water content and fouling conditions in GPR measurements.

# Table of Contents

List of Figures .....	vi
List of Tables .....	ix
Acknowledgements .....	xi
Dedication .....	xii
Chapter 1 - Introduction.....	1
Chapter 2 - Literature Review.....	6
2.1 Unsaturated Materials .....	6
2.2 Measurement of Soil Suction and Modeling the SWCC .....	13
2.3 Characterization of Fouled Ballast .....	21
Chapter 3 - Materials and Methodology .....	28
3.1 Overview .....	28
3.2 Materials .....	28
3.3 Sample Characterization & Classification.....	30
3.4 TRIM Testing .....	33
3.5 Theoretical SWCC of Fouled Ballast. ....	45
Chapter 4 - Results.....	47
4.1 Material Characterization .....	47
4.2 SWCC Results .....	51
SWCCs of Ballast Fouling Materials via the small TRIM .....	51
SWCCs of Fouled Ballast via the Bouwer-Rice Large Particle Correction Procedure.....	53
Proof of Concept: Use of Bouwer-Rice Large Particle Correction Procedure to Predict Fouled Ballast SWCCs. ....	57
Validation: Using the Large TRIM Apparatus to Measure SWCCs of Unsaturated Materials. ....	58
Measuring SWCCs of Fouled Ballast via the Large TRIM.....	59
Chapter 5 - Discussion .....	61
5.1 Ballast Fouling Materials.....	61
5.2 Fouled Ballast .....	65
5.3 General Insight and Application.....	67

Chapter 6 - Conclusions.....	71
Chapter 7 - References.....	74
Appendix A - A Comprehensive Record of Experimental Results .....	83
Contents: .....	83
A.1 Ballast Fouling Materials.....	84
GSD Curves for Ballast Fouling Materials .....	85
TGA Analysis on Fouling Materials Containing Coal Dust.....	88
Unsaturated Characteristics of Ballast Fouling Materials .....	91
A.2 Theoretical Fouled Ballast .....	95
GSD Curves for Theoretical Fouled Ballast Specimens.....	96
Bouwer-Rice Coefficients and Unsaturated Characteristics of Fouled Ballast .....	101
A.3 Fouled Ballast in the Large TRIM Device.....	106
A.4 Example Solution of Richards' Equation using a Backwards Implicate Finite Difference Method .....	107

## List of Figures

Figure 1.1: Diagram of Track Cross Section (not to scale). .....	1
Figure 2.1: SWCC with its parts. ....	8
Figure 2.2: Typical SWCCs for Sand, Silt, and Clay. Adapted from (Tuller, Or, & Hillel, 2004). .....	11
Figure 2.3: SWCCs of Road Base and RAP Materials, and Riprap Bedding.....	12
Figure 2.4: Example of Resilient Modulus correlation to Suction. Adapted from (Ba, Nokkaew, Fall, & Tinjum, 2013). ....	13
Figure 2.5: Diagram of capillary action in soils. ....	15
Figure 2.6: Diagram of axis translation technique.....	17
Figure 2.7: Comparison of Fredlund and Xing 1994 SWCC model to van Genuchten 1980 SWCC model.....	20
Figure 3.1: (Left-Right; Top-Bottom): clean ballast, fouling material, and fouled ballast; fouling materials separated from the fouled ballast: lean clay with coal, silty-sand, and silt. ....	29
Figure 3.2: a) Small TRIM flow cell and b) HAE disc in the base.....	34
Figure 3.3: Example Objective Function from TRIM. ....	38
Figure 3.4: Diagram of the TRIM, Drying State. Diagram Credit: (Wayllace & Lu, 2012) .....	42
Figure 3.5: a) Large & small TRIM cells, b) large cell with fouled ballast, c) sample ballast.....	43
Figure 3.6: Hydraulic Conductivity of Fouled Ballast verses Percentage Fouling (Wallace, 2003). .....	44
Figure 4.1: GSD curves of fouling materials. ....	47
Figure 4.2: Example GSD of Clean Ballast, SW, and a Ballasts 50% fouled with SW. ....	49
Figure 4.3: TGA results for fouling materials #10-#14. ....	51
Figure 4.4: SWCCs of Fouling Materials. ....	53
Figure 4.5: Theoretical SWCCs of 35% fouled ballast. Predicted using the Bouwer-Rice Large	
Figure 4.6: Theoretical SWCCs of 50% fouled ballast. Predicted using the Bouwer-Rice Large .....	56
Figure 4.7: Theoretical SWCCs of 60% fouled ballast. Predicted using the Bouwer-Rice Large	
Figure 4.8: Comparison of SWCCs of Fouled Ballast - Large TRIM Experiment to Brouwer-Rice .....	58

Figure 4.9: Large TRIM SWCCs, Validation of the Large TRIM Experiment.....	59
Figure 4.10: SWCCs of Fouled Ballast, Results of the Large TRIM Experiments.....	60
Figure 5.1: Coal Contaminated Fouling Materials: a) GSD, b) TGA, c) SWCCs.....	65
Figure 5.2: Fouled Ballast: a) GSD, b) SWCCs. ....	67
Figure 5.3: a) Estimated residual volumetric water content of highly fouled ballast versus ballast percent fouling. b) Estimated saturated volumetric water content of highly fouled ballast verses ballast percent fouling.....	69
Figure A.1: GSD of SW Fouling Materials. ....	85
Figure A.2: GSD of SP Fouling Materials.....	85
Figure A.3: GSD of SM (No. 8) and ML (No. 9) Fouling Materials.....	86
Figure A.4: GSD of SC-SM Fouling Materials with Coal Dust. ....	86
Figure A.5: GSD of CL Fouling Materials with Coal Dust. ....	87
Figure A.6: GSD of all Fouling Materials. ....	87
Figure A.7: TGA, Deriv. Weight (%/C) vs. Temp. (C) for the P40 Portion of Fouling Materials Containing Coal Dust.....	89
Figure A.8: TGA, Weight (mg) vs. Temp. (C) for the P40 Portion of Fouling Materials Containing Coal Dust.....	89
Figure A.9:TGA, Deriv. Weight (%/C) vs. Temp. (C) for the P40 and P200 Portions of the CL-2 Fouling Material.....	90
Figure A.10: TGA, Weight (mg) vs. Temp. (C) for the P40 and P200 Portions of the CL-2 Fouling Material.....	90
Figure A.11: SWCCs of SW Fouling Materials. ....	92
Figure A.12: SWCCs of SP Fouling Materials.....	92
Figure A.13: SWCCs of SM (8) and ML (9) Fouling Materials. ....	93
Figure A.14: SWCCs of SC-SM Fouling Materials with Coal Dust. ....	93
Figure A.15: SWCCs for CL Fouling Materials with Coal Dust.....	94
Figure A.16: SWCCs of Fouling Materials. ....	94
Figure A.17: GSD of Theoretical SW Fouled Ballast Specimens. ....	96
Figure A.18: GSD of Theoretical SP Fouled Ballast Specimens.....	96
Figure A.19: GSD of Theoretical SM Fouled Ballast Specimens. ....	97
Figure A.20: GSD of Theoretical ML Fouled Ballast Specimens. ....	97

Figure A.21: GSD of Theoretical SC-CM Fouled Ballast Specimens.....	98
Figure A.22: GSD of Theoretical CL-1 Fouled Ballast Specimens.....	98
Figure A.23: GSD of Theoretical CL-2 Fouled Ballast Specimens.....	99
Figure A.24: GSD Summary of 35% Fouled Ballast Specimens. ....	99
Figure A.25: GSD Summary of 50% Fouled Ballast Specimens. ....	100
Figure A.26: GSD Summary of 60% Fouled Ballast Specimens. ....	100
Figure A.27: Predicted SWCCs for SW Fouled Ballast Specimens. ....	102
Figure A.28: Predicted SWCCs for SP Fouled Ballast Specimens. ....	102
Figure A.29: Predicted SWCCs for SM Fouled Ballast Specimens. ....	102
Figure A.30: Predicted SWCCs for ML Fouled Ballast Specimens. ....	103
Figure A.31: Predicted SWCCs for SC-SM Fouled Ballast Specimens. ....	103
Figure A.32: Predicted SWCCs for CL-1 Fouled Ballast Specimens. ....	103
Figure A.33: Predicted SWCCs for CL-2 Fouled Ballast Specimens. ....	104
Figure A.34: SWCC Summary for 35% Fouled Ballast Specimens.....	105
Figure A.35: SWCC Summary for 50% Fouled Ballast Specimens.....	105
Figure A.36: SWCC Summary for 60% Fouled Ballast Specimens.....	105
Figure A.37: GSD of Fouled Ballast Tested in the Large TRIM.....	106
Figure A.38: SWCCs of Specimens Tested using the Large TRIM. ....	106
Figure A.39: Node diagram for the Backward Implicit Finite Difference solution of Richards' equation with a Neumann boundary condition at the surface and Dirichlet boundary condition at the bottom. ....	112
Figure A.40: Predicted and Measured Cumulative Bottom Flux vs Time. ....	114



## List of Tables

Table 2.1: Diagram of Suction: Total, Matric, and Osmotic (Fredlund & Rahardjo, 1993) .....	14
Table 2.2: SWCC Measurement Methods (ASTM D6836).....	15
Table 2.3: Selig Fouling Index (Selig & Waters, 1994) .....	21
Table 3.1: Hydraulic Properties of HAE Porous Discs (Soilmoisture Equipment Corp., 2020) ..	34
Table 4.1: Geotechnical Properties of Fouling Materials .....	48
Table 4.2: Example Geotechnical Properties of 50% Fouled Ballast. ....	49
Table 4.3: Saturated Hydraulic Conductivity measured on Fouling Materials. ....	49
Table 4.4: Geotechnical Properties of Clean Ballast .....	50
Table 4.5: Summary of Hydraulic Parameters of Fouling Materials.....	53
Table 4.6: Saturated and Residual Volumetric Water Contents, 35% Fouled Ballast.....	55
Table 4.7: Saturated and Residual Volumetric Water Contents, 50% Fouled Ballast.....	56
Table 4.8: Saturated and Residual Volumetric Water Contents, 60% Fouled Ballast.....	57
Table 4.9: Hydraulic Parameters for Ballast 50% fouled with SW: Measured and Predicted .....	58
Table 4.10: Hydraulic Parameters of Fouling Material SW, Validation of Large TRIM Experiment .....	59
Table 4.11: Hydraulic Parameters of Fouled Ballast, Results of the Large TRIM Experiments .	60
Table 5.1: Example Residual and Saturated Water Contents ( $\theta_r$ and $\theta_s$ , respectively) in Relation to the Degree of Fouling and Type of Fouling Material .....	70
Table A.1: Geotechnical Results.....	84
Table A.2: Permeability Methods and Results .....	84
Table A.3: Example of TGA System Information.....	88
Table A.4: TGA sample sizes .....	88
Table A.5: van Genuchten Hydraulic Parameters with Model Fit Statistics .....	91
Table A.6: Density and Porosity of TRIM Specimens .....	91
Table A.7: Geotechnical Data of Fouled Ballast .....	95
Table A.8: Geotechnical Data of Clean Ballast .....	95
Table A.9: Calculated Bouwer-Rice Correction Coefficients ( $V_R$ ) for Predicting Fouled Ballast SWCCs from Fouling Material SWCCs .....	101
Table A.10: Hydraulic and Specimen Parameters of Theoretical Fouled Ballast Specimens ....	101

Table A.11: Large TRIM Specimen Properties .....	106
Table A.12: van Genuchten Hydraulic Parameters with Model Statistics.....	106
Table A.13: Material Properties and van Genuchten Fitting Parameters .....	114

## **Acknowledgements**

My delight and my thanks to my advisor Dr. Stacey Kulesza for inviting me to be part of this project and for her valuable leadership, to my committee members Dr. Michelle Barry, and Dr. Gerard Kluitenberg, to my friends and colleagues, and to my family for your support and patience. We did it!

## **Dedication**

In dedication to my Friend who challenged me and joined me in this new adventure, to my Grandfather, John D. Sherwood, who believed I could do this work and who I kept in my heart along the way, and to my family who put aside their dreams for me so that I could pursue my vision of a MS degree and a career in Geotechnical Engineering.

# Chapter 1 - Introduction

There are nearly 278,000 km of track in the United States. Railway operations using these track support 1.1 million jobs and \$219 billion in output within the USA economy (Association of American Railroads, 2019). Most tracks are supported by a two- or three-layer foundation system: 1) ballast, 2) optional sub-ballast, and 3) natural subgrade (Armstrong, 1990). The track structure is illustrated by the diagram in Figure 1.1. Safe railroad operation is dependent on the integrity of this system. The research herein focuses on unsaturated characterization of the ballast layer. Ballasts are poorly graded aggregates that transfer the dynamic weight of railcars from the ties to the subgrade.

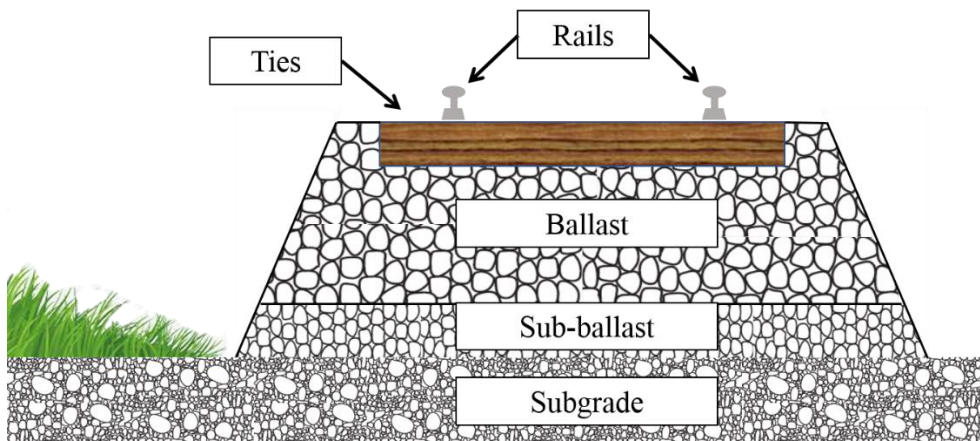


**Figure 1.1: Diagram of Track Cross Section (not to scale).**

Hay (1982) describes ballast as a “logical extension of the subgrade, a placing of the most select materials in the zone of maximum stress concentration”. Ballast are selected to be strong, tough, and durable materials like granite and dolomite: resistant to crushing, abrading, and weathering, capable of enduring railcar loads and adverse environments for a time (lifespan). Ballast are also selected to facilitate rapid drainage of water through and away from the track structure to mitigate the buildup of excess pore water pressure and to prevent destabilization of the track when subjected to cyclic loading (Raymond, 1985). Under normal operating conditions, the track foundation

system degrades. In the ballast layer, degradation is the active process of fouling: the filling of ballast voids with particles finer than 9.52 mm (Armstrong, 1990). Selig, DelloRusso and Laine (1992) investigated 35 rail sites across the USA to identify the sources and causes of ballast fouling; that research showed that fouling generally happens via five modes which are simplified here as two: 1) infiltration of fouling materials, and 2) the breakdown of ballast aggregate over time. Researchers have reported coal, clay, silt, sand, wood, and glass among other materials infiltrating the ballast layer (Raymond, 1985; Selig, DelloRusso, & Laine, 1992; Selig & Waters, 1994; Indraratna, Nimbalkar, & Tennakoon, 2010; Indraratna, Su, & Rujikiatkamjorn, 2011a; Sussmann, Ruel, & Chrismer, 2012); the most prevalent of which are sand, silt, clay and coal. Each material has unique and adverse effects on ballast behavior; generally, causing reductions of permeability, strength, and resiliency (resistance to settlement) (Sussmann, Ruel, & Chrismer, 2012; Indraratna, Su, & Rujikiatkamjorn, 2011a; Indraratna, Ngo, Rujikiatkamjorn, & Vinod, 2014; Ngo, Indraratna, & Rujikiatkamjorn, 2017; Wallace, 2003). As ballast fouling increases, the integrity and functionality of the foundation is increasingly compromised.

Risks associated with uncorrected or unmitigated ballast fouling include loss of track geometry and train derailment; therefore, much research has been conducted to improve assessment, management, and remediation of fouled ballast. The functional life of a ballast can be extended by implementing geosynthetic reinforcement (i.e., geogrid), but aid is limited to a degradation threshold: eventually the fouling condition will become bad enough that replacement of the foundation system becomes necessary (Indraratna, Khabbaz, Salim, & Christie, 2006; Indraratna, Ngo, & Rujikiatkamjorn, 2011b). The functional life of the track can be revived through proper maintenance: resurfacing, cleaning, or replacement of ballast (Hay, 1982; Armstrong, 1990; Selig & Waters, 1994). These maintenance efforts consume resources which

need to be allocated appropriately for sustainable railway operation (Selig & Waters, 1994; Bruzek, Stark, Wilk, Thompson, & Sussmann, 2016). To allocate resources for such maintenance, degradation must be continually monitored, and monitoring must be effective at detecting fouled ballast before that fouling causes catastrophe.

State-of-the-practice methods for detecting and quantifiably assessing fouled ballast are often destructive, costly, time consuming, and labor intensive (Sussmann, Ruel, & Chrismer, 2012; Bruzek, Stark, Wilk, Thompson, & Sussmann, 2016). Conversely, non-destructive methods (e.g., geophysical methods) are being used to qualitatively monitor track conditions such as track geometry, and the presence of water pockets and fouling in the foundation (Sussmann Jr, 1999; De Chiara, Fontul, & Fortunato, 2014), but the non-destructive methods are unreliable for quantifying conditions. Ground penetrating radar (GPR) is one geophysical method widely used by rail industries to identify the presence of fouling yet with significant limitations. GPR measurements are a function of the dielectric constant, which is heavily influenced by the moisture condition and fouling condition (Sussmann Jr, 1999; De Chiara, Fontul, & Fortunato, 2014). The influence of moisture and fouling is coupled in such a way that it is difficult to quantify fouling conditions. For example, highly fouled ballast that is dry may produce the same GPR measurement as a moderately fouled ballast that is saturated.

Sahin (2014) showed that correlations between dielectric constant and the soil water characteristic curve (SWCC) can aid reliable, quantitative GPR evaluation of volumetric water content in road base materials (Sahin, 2014). It is hypothesized that similar correlations between dielectric constant and the SWCC can help to uncouple moisture and fouling conditions in fouled ballast to improve in situ identification of fouling with GPR. SWCCs define the constitutive relationship between moisture condition and matric suction of geomaterials (like fouled ballast);

the SWCC is also correlated with engineering behavior (e.g., permeability, strength, and stiffness). SWCCs are influenced by grain size distribution, density, and minerology (factors associated with fouling conditions) (Vanapalli, Sillers, & Fredlund, 1998; Yang, Rahardjo, Leong, & Fredlund, 2004; Garven & Vanapalli, 2006; Fredlund & Houston, 2009). In parallel, ballast fouling conditions are also dominantly characterized using parameters of grain size distribution, density, and minerology (e.g., Selig & Waters, 1994; Feldman, Nissen, & others, 2002; Indraratna, Su, & Rujikiatkamjorn, 2011a; Tennakoon, Indraratna, Rujikiatkamjorn, Nimbalkar, & Neville, 2012) which suggests congruence between SWCCs and fouling conditions. Although the usefulness of SWCCs is well known in geotechnical engineering, the specimen sizes tested using the traditional equipment available have been limited to small diameters, consequently limiting particle size. Therefore, in order to apply similar techniques to fouled ballast, new equipment and testing methodologies are needed. The objectives of this research were to measure the SWCCs of fouled ballast and fouling materials and to validate a novel methodology for measuring the SWCCs of fouled ballast.

Fourteen samples of different fouling materials were grouped into five material categories using geotechnical and material properties, those categories being: sand (SP or SW), silty-sand (SM), silt (ML), clayey-silty-sand (SC-SM) with coal, and lean clay (CL) with coal. Two fouled ballast specimens (including ballast aggregate) were prepared using SP fouling material; each of the two fouled ballast specimens were prepared to a different degree of fouling (50% fouled and 22% fouled). The SWCCs of the two fouled ballast specimens were measured using a novel application of a method typically used for soils testing: the transient water release and imbibition method (TRIM). These TRIM tests on fouled ballast were performed using an enlarged testing apparatus (large TRIM). The testing method was validated for sandy soil by testing a sand



specimen (SP) using both methods (the original TRIM method and the novel TRIM method) and comparing the results. While the novel testing method was in development, 21 hypothetical fouled ballast specimens were designed and their SWCC's were predicted using the Bouwer-Rice Large Particle Correction Procedure. To assess accuracy of prediction results, one hypothetical fouled ballast specimen (a 50% SP fouled ballast) was replicated in the laboratory and tested using the large TRIM; then, the predicted SWCC was compared to the measured SWCC from the replicate specimen tested in the large TRIM. The Bouwer-Rice Large Particle Correction Procedure requires a minimum degree of fouling; therefore, it has limitations in its application, but the large TRIM can be used to test fouled ballast at all degrees of fouling.

Results highlight that there are measurable differences in SWCC shape for varied fouling conditions (i.e., quantity and type of fouling material), showing that SWCCs can be used to characterize fouled ballast. Results also show that SWCCs can be predicted for and measured on fouled ballast. This research is the first step needed to correlate GPR measurements with SWCCs. Correlations between dielectric constant and SWCCs are hypothesized to uncouple the effect of moisture and fouling conditions in a future project. This thesis is divided into six chapters. Following this introduction, Chapter 2 contains a review of literature pertaining to unsaturated characterization of geomaterials similar to fouled ballast (e.g., road base), state-of-the-practice methods for measuring SWCCs, and characterization of fouled ballast. The literature review is followed by research methods used in this study, which is followed by a summary of results (all results are disclosed in Appendix A). Discussion is presented next and followed by conclusions (Chapters 5 and 6, respectively).

## **Chapter 2 - Literature Review**

### **2.1 Unsaturated Materials**

Unsaturated soils are the part of the earth between the land surface and the ground water table also known as the vadose zone (U.S. Department of the Interior, U.S. Geological Survey, 2017); they are those soils subject to negative pore water pressure (Fredlund & Rahardjo, 1993). Much of railway infrastructure is constructed atop the natural subgrade and above the ground water table. The ballast layer becomes an extension of the subgrade; therefore, its surface becomes the new land surface (Hay, 1982; Armstrong, 1990). Fouled ballast can be dry in persistently arid regions of the globe, and it can be saturated during rain events or flooding (Bruzek, Stark, Wilk, Thompson, & Sussmann, 2016), but the majority of fouled ballast are exposed to fluctuating environmental conditions keeping most of the material in a wet state: drying or wetting (Bruzek, Stark, Wilk, Thompson, & Sussmann, 2016; Rahardjo, Kim, & Satyanaga, 2019). Research shows that materials similar to fouled ballast (e.g., in gradation and/or minerology) do experience negative pore water pressure under these drying and wetting conditions (Khaleel & Freeman, 1995; Gupta, Kang, & Ranaivoson, 2009; Ishikawa, Fuku, Nakamura, Momoya, & Tokoro, 2016). Therefore, a large portion of fouled ballast can be categorized as unsaturated material.

Research on unsaturated materials shows that engineering behavior can change as moisture conditions change (e.g., Likos & Lu, 2004; Sawangsuriya, 2006; Gupta, Ranaivoson, Edil, Benson, & Sawangsuriya, 2007; Fredlund & Houston, 2009; Nokkaew, Tinjum, & Benson, 2012; Ba, Nokkaew, Fall, & Tinjum, 2013; Azam, Cameron, Gabr, & Rahman, 2014; Rahardjo, Kim, & Satyanaga, 2019). Engineering behaviors include strength, stiffness, and permeability. These three behaviors are central to the ballast layer's functions (e.g., resist crushing and abrasion, behave elastic under load, and drain freely when clean). Studies show that as clean ballast become fouled

their behavior degrades and it becomes complex. For example, a ballast layer fouled with clay can behave elastically when dry (experiencing little to no permanent deformation after loading) and then plastically when wet (incurring measurable permanent deformation after loading) (Sussmann, Ruel, & Chrismer, 2012). The general nature of unsaturated material (knowing that the engineering properties change as moisture conditions change) helps to describe the complexity, but little research has been done to quantify unsaturated characteristics of fouled ballast (Kulesza, Sherwood, & Barry, 2019; Sherwood, Kulesza, & Bernhardt-Barry, 2020). Therefore, there are three reasons why fouled ballast need to be characterized using unsaturated methods: 1) fouled ballast commonly exists in an unsaturated state, 2) the engineering behavior of unsaturated materials (like fouled ballast) is complex in response to changing moisture conditions, and 3) little research has been done to characterize fouled ballast as unsaturated material.

The SWCC is a measurement central to characterizing unsaturated materials; it relates the stress states of an unsaturated soil (i.e., matric suction) to its moisture conditions (volumetric water content) (Fredlund & Rahardjo, 1993). The rest of this section is dedicated to the description of the SWCC (i.e., shape, key parameters, physical interpretation), an introduction to typical SWCC results for soils and unbound aggregate, and a review of some of the methods used to measure and model SWCCs. The SWCC is generally sigmoidal in shape and can be unimodal or bimodal (having one or more distinct steps in the ‘S’ shaped curve). The SWCC describes three conditions or phases of an unsaturated soil: the saturated condition, transition phase (i.e., drying or wetting condition), and residual condition. It also quantifies four parameters of interest to geotechnical engineers: saturated volumetric water content ( $\theta_s$ ), air entry ( $\alpha$ ), a parameter proportional to the distribution of pore size ( $n$ ), and the residual volumetric water content ( $\theta_r$ ). Figure 2.1 illustrates

a theoretical SWCC; the three phases and five parts of the SWCC are labeled in the figure and the SWCC is shown as a solid black ‘S’ shaped line.

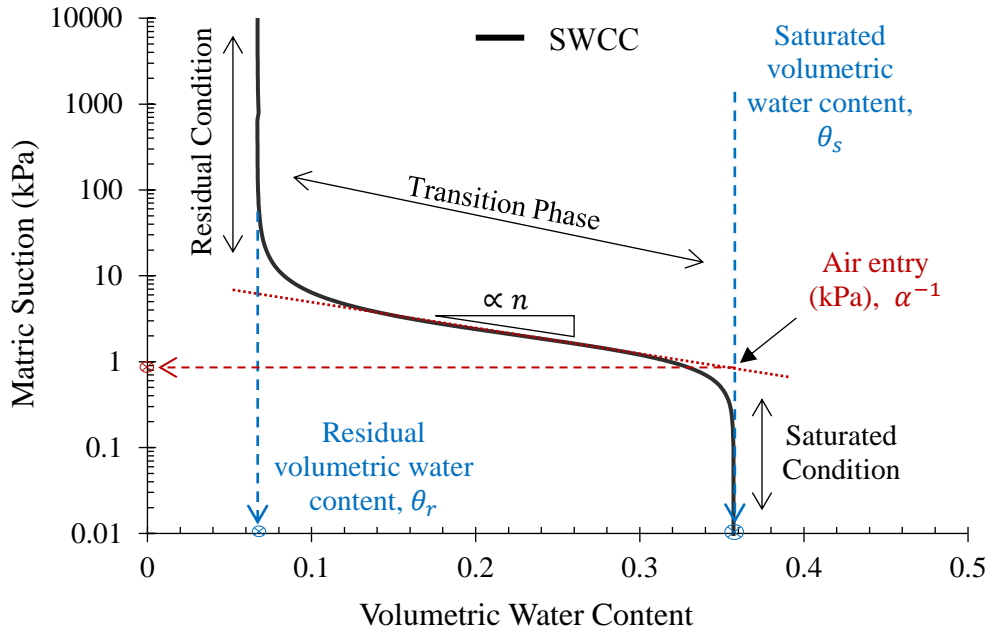


**Figure 2.1: SWCC with its parts.**

SWCCs can be measured as a material dries or as it wets; the curves will differ slightly depending on which one is measured. The details here follow the drying process, which was used for this research. The moisture conditions are described in terms of volumetric water content, which is the volume of water within the saturated soil’s pore network, divided by the total sample volume. Suction is described in units of kilopascals. At the far right of Figure 2.1, the vertical portion of the SWCC, spanning a range of low suction values (0.01 to 0.5 kPa), is the soil’s saturated phase. During this phase of the SWCC, the soil is saturated (most voids are filled with liquid phase water;  $\theta_s = 0.36$  in this example) even though it is experiencing negative pore water pressure. Air may exist as isolated pockets (discontinuous pockets) within the pore network, but liquid phase water will remain continuous (interconnected) within the pore network during this period. The combination of matric potential and an adequate supply of liquid water gives rise to

the saturated phase in the SWCC; that is, soil pores can have enough matric potential to retain sample saturation over a range of suction heads. Moving upward along the suction axis of the SWCC, eventually, the soil's potential to stay saturated is overcome: the SWCC begins to break or curl over to the left, air begins to displace the pore water and the sample starts to drain. The value of suction head at which this break occurs is the air entry value, and it is always correlated with saturated volumetric water content. The air entry value is evaluated at the intersection of two straight lines plotted tangent to 1) the saturated phase of the SWCC and 2) the slope of the transition phase. Therefore, air entry is the amount of suction head that initiates the transition phase (in this case, the draining phase).

The draining phase is the central portion of the SWCC; the slope may be shallow (as shown in Figure 2.1) or steeper. Liquid and gas phases are continuous through the soil's pore network during the transition phase; the continuity of each fluid phase facilitates the flow of each fluid: liquid water can flow out of the sample where liquid water is continuous and air into the sample where air is continuous. This flow takes place within a range of suction values in excess of air entry. The slope of the transition phase is proportional to the fitting parameter 'n' and is characteristic of the sample's pore size distribution. SWCCs with a small slope in the transition phase (i.e., nearly horizontal) are characteristic of samples having a narrow pore size distribution. In response, the sample's moisture condition will transition from the saturated condition to the residual condition over a narrow range of suction values.

The residual condition is characterized by a discontinuous liquid phase and continuous gas phase within the soil's pore network. During the residual phase, liquid water stops draining out of a sample; however, it may still leave the sample in the vapor state (Vanapalli, Sillers, & Fredlund, 1998). At the start of the residual phase, the SWCC breaks or curls upward to a near vertical

orientation and then continues over a range of the highest suction values in the plot. Soil in the residual condition will be highly sensitive to addition of water, readily taking in (imbibing) water whenever and wherever water is available (e.g., rain event). In parallel, small changes in liquid water content can cause large changes in suction when a soil is in the residual phase. The volumetric water content and suction pressure corresponding to the start of the residual phase are the residual volumetric water content and the residual suction pressure, respectively. Symmetric to air entry, they are located on the plot at the intersection of two straight lines drawn tangent to the transition phase of the SWCC and the residual phase. In summary of the SWCC, a soil sample experiences a series of suction states with a few characteristic features (residual and saturated volumetric water content, rate of transition, air entry pressure, and residual pressure) as it transitions from a saturated condition to a residual condition (or vice versa).

The SWCC is a function of many soil parameters controlling the pore network (e.g., material gradation and density). Research shows that as particle sizes decrease and as dry density increases, the air entry and residual pressures and residual volumetric content typically increase (e.g., Yang, Rahardjo, Leong, & Fredlund, 2004; Gupta, Ranaivoson, Edil, Benson, & Sawangsuriya, 2007; Benson, Chiang, Chalermyanont, & Sawangsuriya, 2014). As a result, the SWCC can be very distinctive in its form (i.e., shape and placement) depending on the soil parameters. The SWCC of a soil sample is a thumb print for the soils unsaturated behavior (Fredlund D. G., 2017). While each SWCC is unique, a few generalizations can be made for the major soil types. Typical shapes of SWCCs for sand, silt, and clay are shown in Figure 2.2. In general, sands have lower air entry and residual suction values as well as lower residual volumetric water contents compared to silts and clays. Sands also typically have a narrower pore size distribution or shallower sloping transition phase compared to silt and clay, meaning they drain

more completely over a lower and narrower range of suction heads compared to silt and clay. Clays typically have the highest air entry and residual conditions and the broadest distribution of pore sizes compared to sand and silt. Regarding mineralogy, clays have a net surface charge that interacts with the polar charge of water molecules increasing the clays affinity for water causing more water retention at higher suction heads.

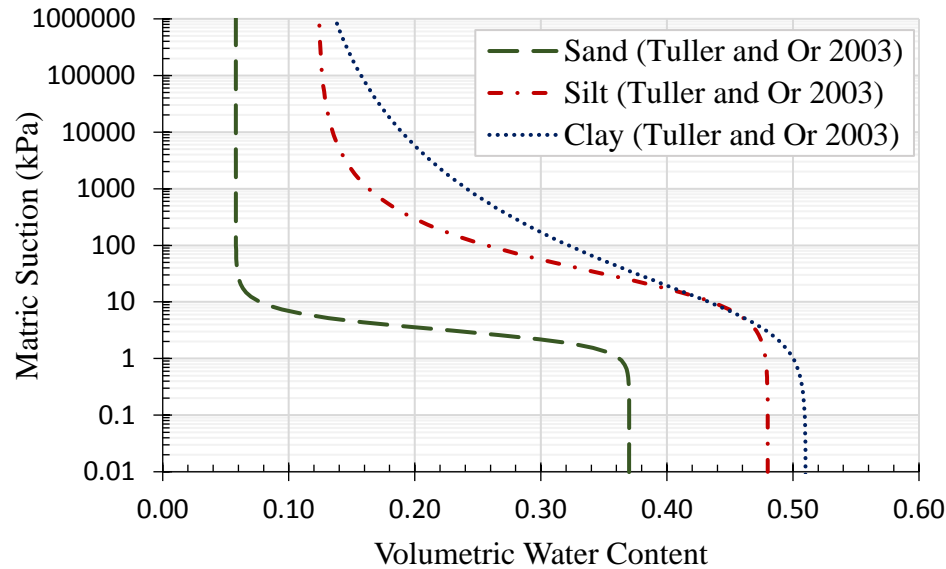


**Figure 2.2: Typical SWCCs for Sand, Silt, and Clay. Adapted from (Tuller, Or, & Hillel, 2004).**

Because a variety of finer materials are found in fouled ballast, the SWCCs are expected to exhibit different characteristics; this expectation applies to ballast having different types and/or different quantities of fouling.

Other near-surface materials similar to fouled ballast (e.g., road and riprap base, recycled concrete material, and recycled asphalt pavement) have been characterized as unsaturated material using SWCCs, and those SWCCs were used to estimate the materials engineering behavior (Gupta, Kang, & Ranaivoson, 2009; Ba, Nokkaew, Fall, & Tinjum, 2013; Bareither & Benson, 2013). Figure 2.3 shows some examples of SWCCs measured on road base materials (Basalt and Quartz), recycled asphalt pavement (RAP) and an alluvium sample (“D”). Similar to fouled ballast, all four

materials contained aggregates larger than 1cm and few fines (mass passing a 0.075 mm sieve): the RAP and alluvium contained less than 1% fines while the road base contained between 7% and 10% fines (Ba, Nokkaew, Fall, & Tinjum, 2013; Bareither & Benson, 2013). None of the coarse samples found in literature contained coal dust and few samples were reported to have fines content (Ba, Nokkaew, Fall, & Tinjum, 2013; Gupta, Kang, & Ranaivoson, 2009; Bareither & Benson, 2013; Azam, Cameron, Gabr, & Rahman, 2014). Because coal dust and fines are commonly found in fouled ballast; existing literature does not adequately capture the unsaturated characteristics of fouled ballast.

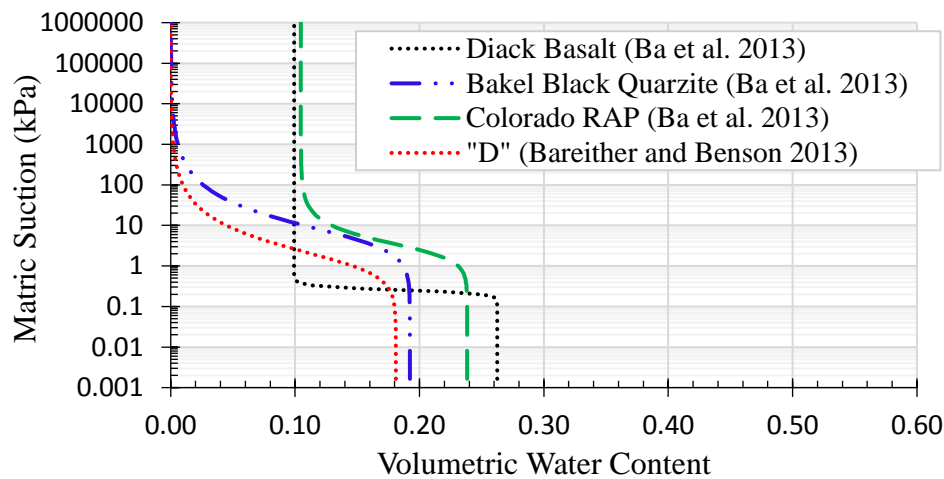


**Figure 2.3: SWCCs of Road Base and RAP Materials, and Riprap Bedding.**

Research in unsaturated road base materials shows that unsaturated characteristics have a predictable influence on road base performance: an increase in suction typically resulted in significant gains in stiffness (Gupta, Ranaivoson, Edil, Benson, & Sawangsuriya, 2007; Azam, Cameron, Gabr, & Rahman, 2014; Ba, Nokkaew, Fall, & Tinjum, 2013), while an increase in water content resulted in reduced shear strength and stiffness (Ba, Nokkaew, Fall, & Tinjum, 2013). The SWCCs in Figure 2.3 have been used to select materials for geotechnical engineering applications, and correlations between these SWCCs and the materials engineering behavior were used for engineering design. For example, Figure 2.4 shows correlations between suction and resilient



modulus of road material: resilient modulus ( $M_r$ ) is the ratio of cyclic axial stress to resilient axial strain, a key parameter used for pavement design. Engineers use such correlations (Figure 2.4) to design roads.

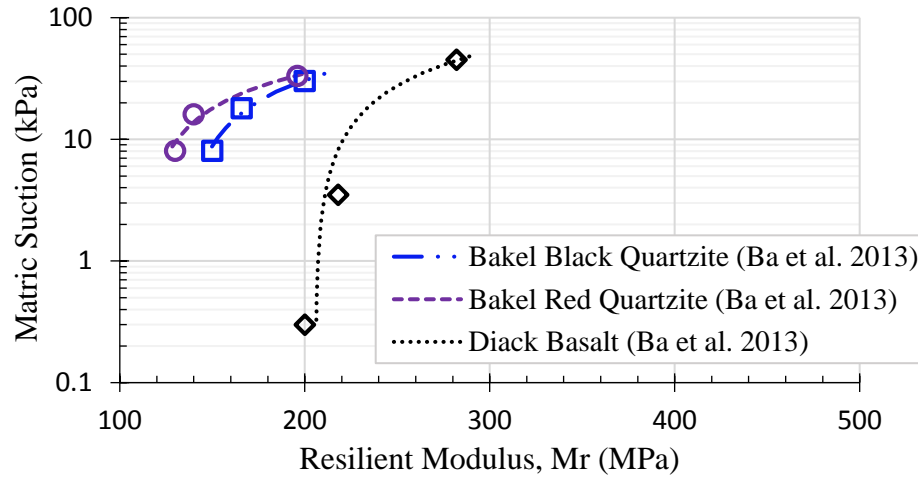


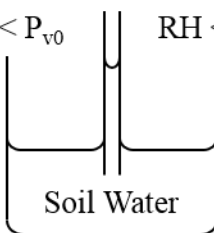
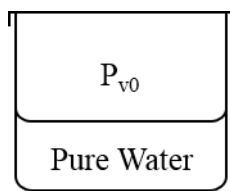
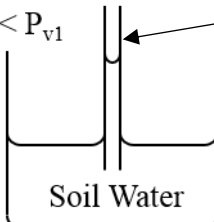
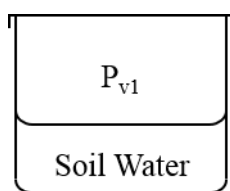
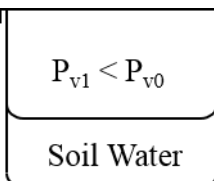
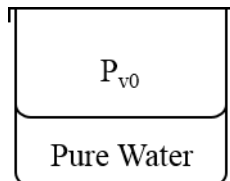
**Figure 2.4: Example of Resilient Modulus correlation to Suction. Adapted from (Ba, Nokkaew, Fall, & Tinjum, 2013).**

## 2.2 Measurement of Soil Suction and Modeling the SWCC

Soil suction is the free energy state of soil pore water (Edlefsen, Anderson, & others, 1943) and is quantified in terms of total suction. Total suction (also called total potential,  $\psi$ ) is derived from the partial pressure of the soil's pore-water vapor in equilibrium with the soil's pore water ( $P_v$  in Table 2.1) relative to the partial pressure of water vapor in equilibrium with a flat surface of pure water ( $P_{v0}$  in Table 2.1) (Aitchison, 1965). Total suction has two components: a matric component and an osmotic component. Matric suction ( $u_a - u_w$ ) is “the difference between the pore gas pressure ( $u_a$ ) and the pore water pressure ( $u_w$ )” (ASTM D6836). Matric suction is also called matric potential or capillary potential and is commonly illustrated by capillary action: water in a capillary tube rising above the surrounding water table. The pore network in soil is analogous to a series of interconnected capillary tubes because it facilitates the rise of pore water above the ground water table: intermolecular forces acting at the soil-water-air interface (surface tension forces,  $T_s$ )

draw water up through the soil pores and above the groundwater table and hold it there (Fredlund & Rahardjo, 1993). Capillary action within soil is illustrated in Figure 2.5. Osmotic suction ( $\pi$ ) is derived from the water vapor pressure in equilibrium with a flat surface of the soil's pore water ( $P_{v1}$  in Table 2.1) relative to the water vapor pressure in equilibrium with a flat surface of pure water ( $P_{v0}$  in Table 2.1) (ASTM D6836). Each suction type is illustrated by the diagrams listed in Table 2.1.

**Table 2.1: Diagram of Suction: Total, Matric, and Osmotic (Fredlund & Rahardjo, 1993)**

Suction	Measured System	Reference Medium
Total, $\psi$	$P_v < P_{v0}$ $RH < 100\%$ 	
Matric, $(u_a - u_w)$	$P_v < P_{v1}$ 	
Osmotic, $\pi$		

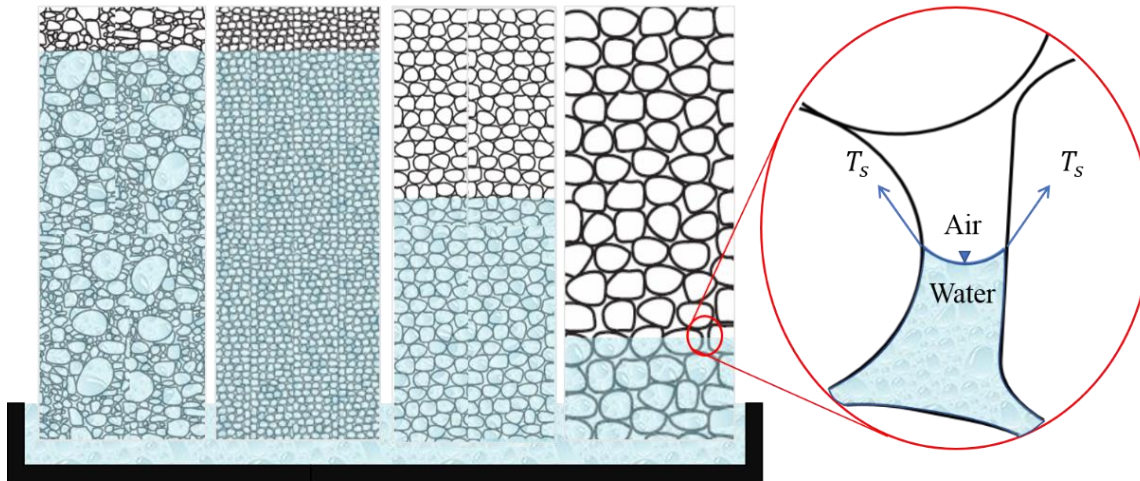


**Figure 2.5: Diagram of capillary action in soils.**

ASTM D6836 gives four methods of determining SWCCs via desorption (drying): the hanging column, pressure extractor, chilled mirror hygrometer, and centrifuge. Each method requires specialized equipment and each method is suitable for specific suction ranges and types of suction (total vs. matric vs. osmotic). Table 2.2 lists each method with its suitable suction range and the type of suction measured. For each method, one successful experiment yields one data point on the SWCC. The procedures of each experiment must be repeated over an array of suction values to collect a series of points in order to model the SWCC. Table 2.2 also lists the approximate time invested in measuring a single data point using each method. Most of the invested time is consumed in waiting for pressures to equilibrate (ASTM D6836).

**Table 2.2: SWCC Measurement Methods (ASTM D6836)**

Testing Method	Suction Range	Suction Type	Time (hrs.)
Hanging Column	0 – 80 kPa	Matric	48
Pressure Extractor	0 – 1500 kPa	Matric	24 to 96
Chilled Mirror Hygrometer	500 kPa – 100 Mpa	Total	24
Centrifuge	0 – 120 kPa	Matric	2

For example, the hanging column and pressure extractor methods use an axis translation technique where suction is imposed on unsaturated soil, and water potential is controlled by liquid

phase transfer through a saturated high air entry (HAE) membrane, like a HAE ceramic disc (Delage, Romero, & Tarantino, 2008). Suction is typically imposed by applying a pneumatic pressure from above which creates an artificial increase in atmospheric pressure around the sample. This offsets the equilibrium between pore air and pore water pressure forcing drainage. Water drains until the negative pore water pressure equilibrates with the new atmosphere. This technique is illustrated in Figure 2.6 where a diagram of a test specimen is shown (top) along with a simplified free body diagram of the experimental process applying the capillary tube analogy (bottom). The sample begins at the saturated state, and it may remain saturated at an air gauge pressure ( $u_a$ ) of zero as shown in stage one: the surface tension forces ( $T_s$ ) carry the weight of the column of water ( $W_{H_2O}$ ). In stage two, a small increase in air pressure is applied to the sample which works against the surface tension forces and causes release of water (reduction in  $W_{H_2O}$ ) to reestablish system equilibrium. This process continues as pressure is increased, stage 3. The HAE membrane is selected such that the imposed air pressure does not induce drainage of its (the HAE membrane's) pore water; therefore, all water leaving the system comes solely from the soil pores. Water is transferred through the HAE disc as the soil drains and the HAE disc remains saturated throughout the test. Therefore, the moisture state of the soil can be accurately tracked from the initial moisture condition by accounting for the water leaving the system. The final water content of the soil can then be correlated with the imposed suction to assess a point on the SWCC.

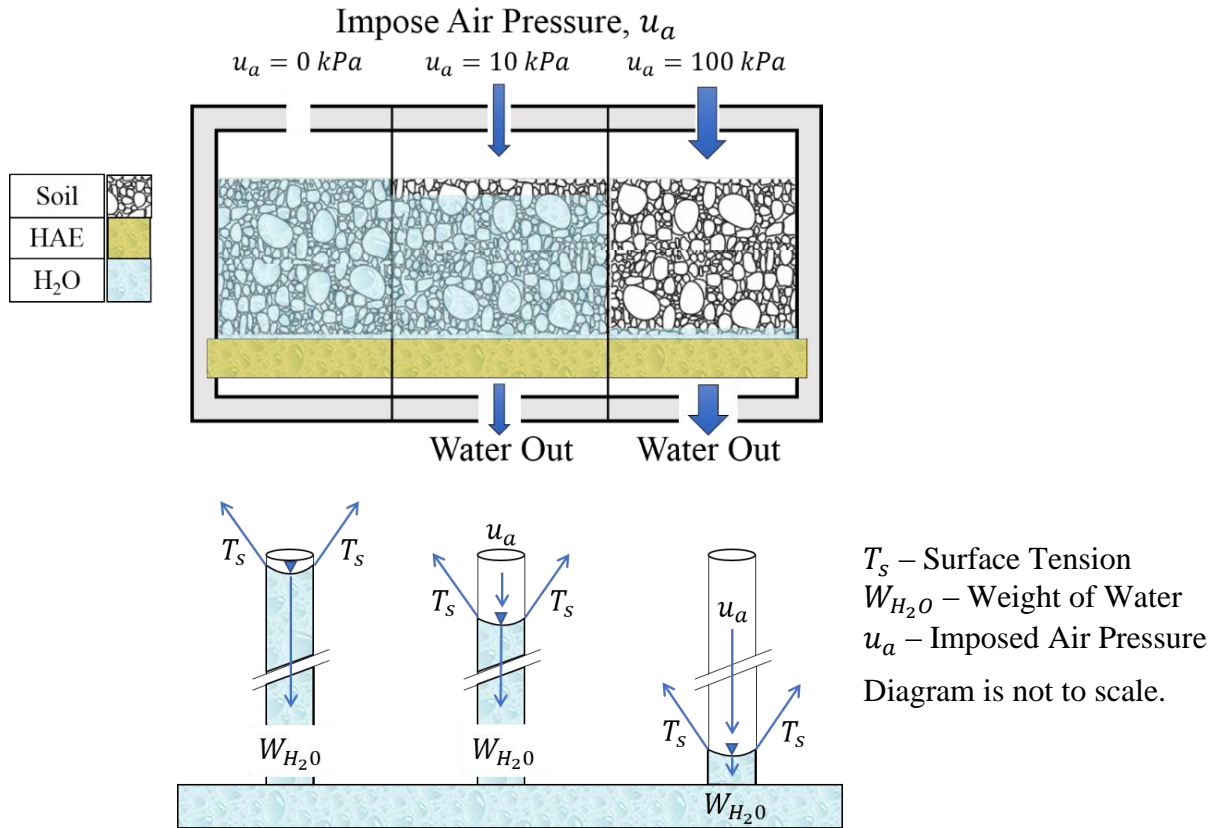


**Figure 2.6: Diagram of axis translation technique.**

The SWCC can also be determined using an inverse modeling method (Kool, Parker, & Van Genuchten, 1985; Eching & Hopmans, 1993; Chen, Hopmans, & Grismer, 1999; Hopmans, Šimunek, Romano, & Durner, 2002; Wayllace & Lu, 2012). Hopmans et al. (2002) defines inverse modeling as “a general mathematical method to determine unknown causes on the basis of observation of their effects, as opposed to modeling of direct problems whose solution involves finding effects on the basis of a description of their causes”. The axis translation technique is used in this method, but the data of interest are different from the ASTM D6836 methods. Unsaturated transient outflow data (i.e., the cumulative mass or volume of water released from a specimen), as a function of time and imposed suction, are the primary data of interest when using the inverse method whereas the final equilibrated suction/moisture states where the data of interest when using the ASTM D6836 methods. The transient outflow data are used as an objective function to

mathematically model the SWCC. A solution of Richards' equation for one dimensional flow (Richards, 1931) is fitted to the outflow data (the observed effect of soil suction) by optimizing parameters of the SWCC and hydraulic conductivity function (HCF) (the unknown cause of unsaturated flow behavior).

Wayllace and Lu (2012) proposed a transient water release and imbibition method that operates on the inverse modeling and axis translation principles. Their method can determine the SWCC for a sample within 84 to 114 hours (Wayllace & Lu, 2012). Non-uniqueness of inversely determined unsaturated parameters was a major concern in the development of the inverse method because more than one set of optimized fitting parameters could give a good fit to the objective function (Hollenbeck & Jensen, 1998; Russo, Bresler, Shani, & Parker, 1991). Research shows that unique parameters can be determined by carefully selecting the hydraulic model for flow simulations, applying appropriate boundary conditions, and analyzing data spanning an appropriate range of water content (the majority of the samples storage capacity) (Zachmann, Duchateau, & Klute, 1981; Zachmann, Du Chateau, & Klute, 1982; Kool, Parker, & Van Genuchten, 1985; Hopmans, Šimunek, Romano, & Durner, 2002; Wayllace & Lu, 2012). Several model parameters (e.g., permeability and saturated volumetric water content) can be measured in a lab, and typical values of fitting parameters (e.g., air entry value, the fitting parameter 'n' which reflects the pore size distribution, and residual water content) have been published for many soils and several models (e.g., Tuller, Or, & Hillel, 2004; Benson, Chiang, Chalermyanont, & Sawangsuriya, 2014). Therefore, the TRIM is a popular method for determining the unique SWCC of a soil.

Several hydraulic models have been proposed for inverse modeling of unsaturated soil hydraulic properties. Example models include: Mualem-van Genuchten (Van Genuchten, 1980),

Books and Corey (Brooks & Corey, 1966), and Gardner-Russo (Russo, 1988). Two common SWCC models are introduced in the following two paragraphs: the van Genuchten model (Van Genuchten, 1980) and the Fredlund and Xing model (Fredlund & Xing, 1994).

The van Genuchten model fits the behavior of most soils and is commonly used by soil physicists, agronomists, and geotechnical engineers to evaluate unsaturated soil behavior (e.g., Kool, Parker, & Van Genuchten, 1985; Hopmans, Šimunek, Romano, & Durner, 2002; Yang, Rahardjo, Leong, & Fredlund, 2004; Gupta, Kang, & Ranaivoson, 2009; Wayllace & Lu, 2012; Benson, Chiang, Chalermyanont, & Sawangsuriya, 2014). The van Genuchten model is defined as:

$$\theta(\psi) = \theta_r + (\theta_s - \theta_r) \left( \frac{1}{1 + (\alpha * \psi)^n} \right)^m \quad \text{Equation 2.1}$$

where,  $\theta(\psi)$  is the SWCC,  $\theta_s$  is the saturated volumetric water content,  $\theta_r$  is the residual volumetric water content,  $\alpha$ ,  $n$  and  $m$  are fitting parameters, and  $\psi$  (kPa) is any soil suction.

The Fredlund and Xing model also fits most soils and is also commonly used by geotechnical engineers working in the field of unsaturated soil mechanics (e.g., Yang, Rahardjo, Leong, & Fredlund, 2004; Fredlund & Houston, 2009; Gupta, Kang, & Ranaivoson, 2009; Bareither & Benson, 2013; Azam, Cameron, Gabr, & Rahman, 2014). The Fredlund and Xing model is defined as:

$$\theta(\psi) = \theta_s \left[ 1 - \frac{\ln(1 + \psi/\psi_r)}{\ln(1 + 10^6/\psi_r)} \right] \left[ \frac{1}{[\ln(e + (\psi/a)^n)]^m} \right] \quad \text{Equation 2.2}$$

where,  $\theta(\psi)$  is the SWCC,  $\theta_s$  is the saturated volumetric water content,  $a$ ,  $n$  and  $m$  are fitting parameters,  $e$  is Euler's number (i.e., 2.71828),  $\psi$  (kPa) is any soil suction, and  $\psi_r$  (kPa) is the soil suction corresponding to residual volumetric water content (Fredlund & Xing, 1994). The Fredlund and Xing SWCC model and the van Genuchten SWCC model differ in the assessment

of residual moisture conditions. Fredlund and Xing (1994) observed that soil moisture conditions tend to gravitate toward a value of zero as suction approaches  $10^6$  kPa. Therefore, their model forces the SWCC to converge on a value of zero moisture at a suction head of  $10^6$  kPa.

SWCCs modeled using the Fredlund and Xing model and van Genuchten model are compared for the same soil in Figure 2.7. The two SWCCs overlap throughout all phases of the SWCC except for the residual phase where the van Genuchten model assumes that the volumetric water content remains constant after residual state is achieved. The Fredlund and Xing model captures how a sample becomes nearly dry: the volumetric water content approaches a value of zero as the matric suction approaches one million kilopascals (Fredlund & Xing, 1994).

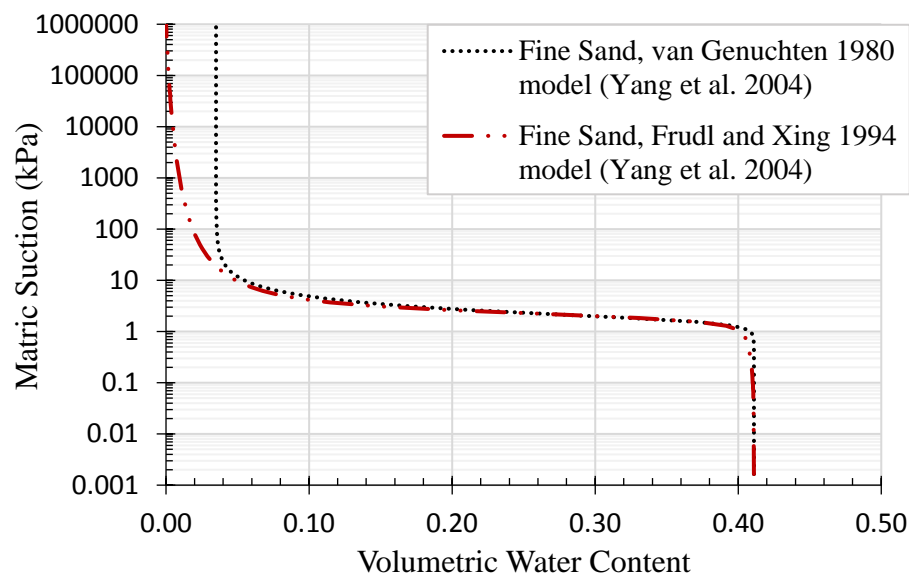


**Figure 2.7: Comparison of Fredlund and Xing 1994 SWCC model to van Genuchten 1980 SWCC model.**

The van Genuchten SWCC model uses the residual volumetric water content as a fitting parameter. The residual phase of the SWCC should not be used for interpretation of the soil's behavior outside of it being the “maximum amount of water in a soil that will not contribute to liquid flow” (Vanapalli, Sillers, & Fredlund, 1998). The Fredlund and Xing SWCC model is not currently available in public software as a modeling option for use in inverse methods, but the van



Genuchten model is programmed into the functionality of Hydrus 1D (Version 4.xx), a public modeling environment for various analysis and simulations including modeling of SWCCs using inverse methods (Simunek, et al., 1998). Therefore, the van Genuchten (1980) hydraulic model is currently the more readily available model for determining SWCCs via inverse methods.

## 2.3 Characterization of Fouled Ballast

Much research has been done to characterize fouled ballast in dry and saturated conditions. The following is a review of how engineers describe/quantify ballast fouling conditions, and how fouling (type and quantity) influences permeability, shear strength, and stiffness.

Several indices have been developed to describe in situ ballast fouling conditions (Selig & Waters, 1994; Feldman, Nissen, & others, 2002; Indraratna, Su, & Rujikiatkamjorn, 2011a; Tennakoon, Indraratna, Rujikiatkamjorn, Nimbalkar, & Neville, 2012). An intuitive measure of fouling is the percentage of fouling which is defined as: the ratio of the mass fraction passing the 9.52 mm sieve over the total dry sample weight. This method is simple to measure and simple in the insight it provides regarding ballast conditions. Selig and Waters (1994) proposed a more informative index parameter (F1) calculated as the sum of the mass fractions passing a No. 4 sieve and a No. 200 sieve. Selig and Waters (1994) developed a standard for assigning priority to ballast for repair called the Selig Fouling Index (SFI). The standard was developed through a series of empirical correlations between F1 and fouled ballast behavior (e.g., permeability), and it categorizes fouled ballast via ranges of F1 (Selig & Waters, 1994). Those categories and their ranges of F1 are listed in Table 2.3.

**Table 2.3: Selig Fouling Index (Selig & Waters, 1994)**

Clean	Moderately Clean	Moderately Fouled	Fouled	Highly Fouled
$F1 < 1$	$1 \leq F1 < 10$	$10 \leq F1 < 20$	$20 \leq F1 < 40$	$F1 \geq 40$

The SFI and F1 are commonly used to describe fouled ballast (Sadeghi, Motieyan-Najar, Zakeri, Yousefi, & Mollazadeh, 2018) but cannot distinguish between types of fouling materials (e.g., clay from coal dust) (Indraratna, Su, & Rujikiatkamjorn, 2011a). The Percent fouling and SFI indices do not provide information regarding how much of the ballast void space is filled with fouling. Addressing the latter, Feldman and Nissen (2002) created the percentage void contamination (PVC) which is the ratio of the total volume of fouling material over the volume of ballast voids. The PVC may overpredict fouling because it does not account for gradation; a coarse fouling material (e.g., coarse sand) could fill ballast voids without causing significant loss in ballast performance. Research shows that coarse fouling material would not significantly affect the ballast performance (e.g., Wallace, 2003; Indraratna, Nimbalkar, & Tennakoon, 2010). In this scenario, the PVC would indicate that the ballast is highly fouled while its performance would still be acceptable (close to that of the clean ballast). Indraratna et al. (2011a) proposed an alternative to the PVC which better represented the influences of material type and gradation compared to F1 and PVC, respectively. The new parameter was called the relative ballast fouling ratio (Rb-f), which is calculated as the ratio of the volume of fouling solids over the volume of ballast solids. Tennakoon et al. (2012) modified the PVC parameter creating the Void Contamination Index (VCI) which incorporated void ratio and specific gravity of the ballast and of fouling materials when evaluating fouling conditions. VCI is challenging to measure given void ratio and specific gravity are necessary inputs, but it is the most informative parameter of those found in literature. Percent fouling and F1, while less informative, are easy to measure and they are the most commonly used parameters.

Researchers have studied how ballast fouling affects ballast permeability (i.e., saturated hydraulic conductivity) and have characterized ballast permeability as a function of fouling (e.g.,

Selig & Waters, 1994; Wallace, 2003; Indraratna, Nimbalkar, & Tennakoon, 2010; Tennakoon, Indraratna, Rujikiatkamjorn, Nimbalkar, & Neville, 2012). Fluid flow through the ballast layer is facilitated by voids between aggregates and is therefore a function of void cross section area and connectivity. A clean ballast has an average permeability of 0.3 cm/s (Indraratna, Nimbalkar, & Tennakoon, 2010). As the voids between ballast fill up with particles finer than 9.52 mm, permeability is reduced. Research shows that the reduction in permeability varies by type of fouling material (gradation) as well as the quantity (volume). Regarding gradation, permeability rapidly degrades as the portion of fouling particles (finer than 9.52 mm) increase. Selig and Waters (1994) note that permeability rapidly degrades once fouling reaches an F1 of 30. Wallace (2003) noted that coarse fouling materials do not significantly affect the permeability of ballast; rather, clay and silt fines were the portions of fouling material that greatly reduced the permeability of ballast. Sand particles are large compared to silts and clays, so they create larger voids and are more permeable compared to silts and clays. This phenomenon is captured well by F1 through the emphasis given to the fraction of fines in a fouled ballast (passing No. 200 sieve). As the voids between ballast fill with fouling material, the pore structure becomes more defined by the fouling material and the fouling material begins to govern the permeability of the ballast layer.

Laboratory experiments on fouled ballast show that when the voids between ballast become 50% filled by fouling material (i.e., when the VCI of a fouled ballast is 50%) the permeability of the fouled ballast layer is reduced to that of the fouling material regardless of the type of fouling material (Tennakoon, Indraratna, Rujikiatkamjorn, Nimbalkar, & Neville, 2012). Therefore, voids between ballast do not need to be filled completely with fouling materials for permeability of the ballast layer to be reduced to that of the fouling material alone. In general, fouling of ballast reduces ballast permeability, and the fouling materials (i.e., kind and quantity) regulate the severity

of the reduction. Reduced permeability enhances the potential for pore water to become confined within and around the track foundation. When subject to cyclic loading, pore water pressure can develop compromising track integrity: reducing sub-ballast/subgrade bearing capacity, increasing settlement, and worsening fouling by causing pumping of subgrade. No literature was found characterizing the unsaturated flow properties of fouled ballast. Water contents spanning the full spectrum of moisture conditions (saturated to unsaturated to dry) have been observed in ballast in situ. Recall that fouled ballast are near surface geomaterials and tracks have been built in a variety of environments (from arid deserts to saturated swamps). An investigation of fouled ballast in an unsaturated state will provide a more complete description of fouled ballast hydraulic conductivity.

Limited research was found characterizing the strength and resiliency of fouled ballast (e.g., Tutumluer, Dombrow, & Huang, 2008; Tutumluer, et al., 2011; Rujikiatkamjorn, Indraratna, Ngo, & Coop, 2012; Indraratna, Ngo, Rujikiatkamjorn, & Vinod, 2014; Ishikawa, Fuku, Nakamura, Momoya, & Tokoro, 2016; Ngo, Indraratna, & Rujikiatkamjorn, 2017). Rujikiatkamjorn et al. (2012) tested dry ballast fouled with coal and showed a rapid reduction in peak friction as the VCI increased: small amounts of coal will lubricate the ballast aggregate surfaces keeping ballast aggregate from reaching their peak friction angle (Rujikiatkamjorn, Indraratna, Ngo, & Coop, 2012). Also, as VCI increases from zero to 100, more force is transferred from the stronger ballast aggregates to the weaker fouling materials causing reduction in strength (Indraratna, Ngo, Rujikiatkamjorn, & Vinod, 2014). Large scale triaxial tests performed on saturated clay-fouled ballast show similar results: clay, like coal, reduced ballast friction by lubricating ballast surfaces and by increasingly redistributing forces from between stronger ballast aggregate to the weaker clay materials as VCI increased (Ngo, Indraratna, & Rujikiatkamjorn, 2017). The loss of friction between ballast particles due to fouling allows ballast to rearrange more

easily leading to loss of layer stiffness resulting in settlement (Budiono, McSweeney, Dhanasekar, & Gurung, 2004; Indraratna, Ngo, & Rujikiatkamjorn, 2011b).

Ballast fouling will cause excessive settlement if the ballast section is not repaired (e.g., Hay, 1982; Budiono, McSweeney, Dhanasekar, & Gurung, 2004; Chrismer, 2008; Fortunato, Pinelo, & Fernandes, 2010; Indraratna, Ngo, & Rujikiatkamjorn, 2011b; Sussmann, Ruel, & Chrismer, 2012; Indraratna, Ngo, & Rujikiatkamjorn, 2013; Kashani, Ho, & Hyslip, 2018). Geogrids have been shown to mitigate loss of strength and resiliency by the addition of frictional surfaces and by additional confinement of aggregates (e.g., Konietzky, te Kamp, Groeger, & Jenner, 2004; McDowell & Stickley, 2006), but the benefits from geogrids were found to be limited by the extent of fouling (Indraratna, Ngo, & Rujikiatkamjorn, 2011b).

Tutumluer et al. (2008) and Ishikawa et al. (2016) characterized strength and resiliency of unsaturated fouled ballast (Tutumluer, Dombrow, & Huang, 2008; Ishikawa, Fuku, Nakamura, Momoya, & Tokoro, 2016). Tutumluer et al. (2008) conducted large scale direct shear tests on dry and on wet coal fouled ballast. They showed that the ballast friction angle is significantly reduced as F1 increased. Comparing wet fouled ballast to dry fouled ballast, wetting alone further reduced shear strength at each fouling degree (Tutumluer, Dombrow, & Huang, 2008; Tutumluer, et al., 2011). Ishikawa et al. (2016) reported strength and SWCC results for one fouling degree using a scaled-down clay fouled ballast (half mean grain sized ballast). Through strength testing, Ishikawa et al. determined that water content and fines fraction influence the peak strength of fouled ballast (both reduce strength) concluding that moisture content and fines fraction (i.e., fouling conditions) must be accounted for when evaluating mechanical properties of railroad ballast. Their SWCCs showed that fouling increased the residual water content of the ballast sample.

In general, the literature shows that dry, saturated, and unsaturated ballast fouling reduces contact between ballast aggregates, and/or lubricates aggregate surfaces, resulting in loss of strength and loss of resiliency. Regarding strength of unsaturated fouled ballast, Tutumluer et. al. (2008 and 2011) found that increased moisture at a fixed fouling condition caused reductions of strength in laboratory prepared fouled ballast samples. Three moisture conditions were evaluated using pure coal as a fouling material. Sussmann et al. (2012) reports that in field measurements of vertical track deflection (an indicator of in situ ballast performance) are greatly influenced by the moisture condition of the track, observing greater deflection when fouled ballast are wet compared to dry. As highlighted herein, there has been very limited research on unsaturated fouled ballast. There is currently a great need for characterization of fouled ballast strength and resiliency as a function of varied moisture and fouling conditions.

All losses (i.e., reduced permeability and strength, and increased differential settlement) can lead to train derailment. Therefore, it is important to continually monitor railroad ballast for fouling conditions so that necessary repairs can be scheduled appropriately (Hay, 1982; Armstrong, 1990; Selig & Waters, 1994; Fortunato, Pinelo, & Fernandes, 2010; Sussmann, Ruel, & Chrismer, 2012). There are several methods for detecting/identifying a fouled ballast in situ. The most reliable way to identify a fouled ballast is by excavation and analysis (i.e., measurements of F1 and/or VCI). This destructive method is costly, time consuming and labor intensive. It is also limited by the discrete nature of sampling: depending on sample location, an anomaly (e.g., a small pocket of fouled ballast in an otherwise clean section of track) could be missed. A less reliable method is to interpret geophysical measurements. Geophysical measurements are non-destructive, and many can be taken continuously or pseudo continuously. GPR is one geophysical method gaining ground as a fouled ballast detection method because it is currently used to monitor

other track conditions: depth of the ballast layer and pooling of water (e.g., Sussmann, 1999; De Chiara, Fontul, & Fortunato, 2014; Anbazhagan, Dixit, & Bharatha, 2016). The response of GPR is a function of the dielectric constant. The dielectric constant of fouled ballast is influenced by moisture content, the type of ballast and fouling materials, the density of the ballast section, and the degree of fouling (Sussmann, 1999; Clark, Gillespie, Kemp, McCann, & Forde, 2001; Sussmann, Selig, & Hyslip, 2003; Zhang, Gascoyne, & Eriksen, 2011; De Chiara, Fontul, & Fortunato, 2014). Chiara et al. (2014) noted that GPR measured dielectric constant increases as water content increases where fouling conditions are fixed and that the dielectric constant increases as  $R_f$  increases where water content is fixed.

GPR has been used to detect water, and to determine moisture content. Sahin et al. (2016) showed that GPR could be used to determine the volumetric water content of road base materials (comparable to fouled ballast) by correlating unsaturated characteristics (namely suction and water content relationships) to dielectric constant. Based on that research, it may be possible to use GPR to evaluate moisture and fouling conditions of a ballast layer. First, the unsaturated characteristics of fouled ballast are needed, and quantifying them is the objective of this research.

## **Chapter 3 - Materials and Methodology**

### **3.1 Overview**

The objective of this study is to characterize ballast fouling materials and fouled ballast using soil water characteristic curves (SWCC) and to validate a new method for measuring SWCCs on fouled ballast. Materials for this project were donated by BNSF Railway and Metrolink. All materials were characterized using geotechnical and materials testing methods. Testing methods for measuring SWCCs of fouling material were modified to enable measurements on fouled ballast. A theory-based correction procedure was also used to rapidly predict SWCCs of fouled ballast from the SWCCs of fouling materials. This chapter describes the materials and the testing methods used in this research.

### **3.2 Materials**

All samples were disturbed samples. They included: samples of ballast, fouling materials, and fouled ballast. The granitic ballast was collected from a quarry in Oklahoma. Seven one-gallon samples of fouling material were collected from fouled ballast. These samples of fouling material were made up of shards, chips, and granules broken off ballast aggregate. They (all seven fouling material samples) passed through a 9.54 mm sieve (3/8 in.) and were retained on a 0.074 mm sieve (No. 200). There were no ballast or fines in these seven samples. These fouling materials classified as poorly graded sand (SP) with gravel or as well graded sand (SW) with gravel.

Seven 5-gallon samples of fouled ballast were collected from main lines. These fouled ballast samples contained ballast aggregate, ballast breakdown, and fines (i.e. clay, silt, and coal). Main lines are commonly used to transport coal freight and the fines within five of these fouled ballast samples were dark grey in color suggesting the presence of coal. Therefore, those five fouled ballast samples likely contain coal. The other two samples were fouled with light brown



colored materials transported into the ballast by water flow; one of the two smelled strongly of fertile soil. Each of the seven fouled ballast samples were separated into ballast and fouling material by sieving and washing. The wash of each sample was retained, dried, and added back to the fouling materials. Each fouled ballast sample was processed separately. The fouling material samples retained through this process classified as either silty-sand, silt, clayey-silty sand, or lean clay. An example of each kind of sample (clean ballast, fouling material, fouled ballast, and fouling materials separated from the fouled ballasts) are shown in Figure 3.1.



**Figure 3.1: (Left-Right; Top-Bottom): clean ballast, fouling material, and fouled ballast; fouling materials separated from the fouled ballast: lean clay with coal, silty-sand, and silt.**

Twenty-one hypothetical fouled ballast specimens were designed by mixing fouling materials with AREMA #4 graded ballast (AREMA, 2019) to three degrees of fouling (35%, 50%, and 60% fouled). AREMA #4 gradation was used for ballast in this study because it is used throughout the USA as a standard for mainline ballast design (AREMA, 2019). Fouling conditions were regulated by controlling the percent mass passing a 9.52 mm (or 3/8 in.) sieve (i.e., the percent fouling).

Two more fouled ballast specimens were designed and prepared in the lab for testing in the large TRIM device; the specimens were designed using the same method as for the hypothetical

specimens. Poorly graded sand was used as the fouling material (SP). The percent fouling for each specimen was 50% fouled and 22% fouled. The total dry mass of both of the two specimens was 11.56 kg. The intricacies of fouled ballast design are included in the methods section of this report.

In summary, the total sample and specimen inventory included: 14 fouling material samples; approximately 100 kg of clean granitic ballast; 21 hypothetical ballast specimens (seven at 35% fouling, seven at 50% fouling, and seven more at 60% fouling); and two laboratory prepared ballast specimens (a 22% SP fouled ballast and a 50% SP fouled ballast).

### **3.3 Sample Characterization & Classification.**

The 14 fouling material samples were characterized or classified with the following: grain size distribution (ASTM D6913; D1140; D7928), Atterberg limits (as needed; ASTM D4318), specific gravity (ASTM D854), saturated hydraulic conductivity (ASTM D5856 and D5084; Wayllace and Lu, 2012), and Unified Soil Classification System (USCS) (ASTM D2487). Five fouling material samples suspected of coal content were characterized using thermogravimetry (Zhang, et al., 2015). All fouled ballast specimens (hypothetical and physical alike) were characterized by grain size distribution (ASTM C136 ;D6913; D1140; D7928) and specific gravity (ASTM C127; D854); then and classified using percent fouling, the SFI (Selig & Waters, 1994) and the VCI (Indraratna, Su, & Rujikiatkamjorn, 2011a). SWCCs were measured on specimens molded from each sample of fouling material using the TRIM (Wallace and Lu 2012). SWCCs were measured on the laboratory prepared fouled ballast specimens (the 50% SP fouled and 22% SP fouled ballast) using a novel method presented herein. All specimens were prepared to a target density, molding them by hand in a laboratory.

Thermogravimetric analysis (TGA) was used to identify coal in the five fouling materials expected to contain coal dust. TGA was conducted on the portion of each material passing the No.

40 sieve (0.42 mm) because coal dust/particles are generally small (Sapko, Cashdollar, & Green, 2007). One sample of material passing the No. 200 sieve (0.074 mm) was also tested to determine if any coal was clay or silt sized. For each of the five fouling materials, approximately 10 milligrams of their finer portion were heated in the TGA apparatus from ambient temperature to 850 °C at 10 °C per minute. A platinum massing tray was used to hold the material in the furnace, and the testing system was continually purged with Nitrogen gas to prevent ignition of materials. The balance purge flow and sample purge flow rates were set to 20 mL min.<sup>-1</sup> and 80 mL min.<sup>-1</sup>, respectively. Mass change of the sample (due to materials volatilizing) was recorded as a function of time and temperature. The first order derivative of the mass change vs. temperature was analyzed to identify temperatures which induced the greatest change in mass. The temperatures causing the greatest mass change were compared to the literature on coal to validate the presence of coal. The area under a percent-mass vs. temperature curve was evaluated between 300 and 800 °C to determine how much volatile material was in each of the five samples (and to help gauge the coal content).

As mentioned in the materials section of this report, several fouled ballast specimens (21 hypothetical and two laboratory prepared fouled ballast specimens) were designed in this study. Two parameters were used to control design: 1) the initial (clean) gradation of the ballast aggregates and 2) the final fouling condition. The ballast aggregates were initially graded to meet AREMA #4 standards (AREMA, 2019). AREMA #4 gradation is used throughout the USA as a standard for mainline ballast design (AREMA, 2019). Then a fouling material was added until a target fouling condition was met; fouling conditions were regulated by controlling the percent mass passing the 9.52 mm (3/8 in.) sieve (i.e., the percent fouling). The following describes the design of a 11 kg fouled ballast specimen for testing in the large TRIM cell. To make a fouled

ballast specimen that has a bulk dry mass of 11 kg and a percent fouling of 22% (using any fouling material), mix 8.58 kg of AREMA #4 graded ballast (78% of 11 kg) with 2.42 kg of fouling material (22% of 11 kg). In the case of hypothetical specimens, AREMA #4 graded ballast were mixed with seven of the fouling materials samples to three degrees of percent fouling (35%, 50%, and 60%). The seven fouling material samples were selected to best represent each kind of fouling material and to avoid unnecessary duplicates. In the case of laboratory tested specimens, AREMA #4 graded ballast were mixed with SP fouling material to two degrees of percent fouling (22% and 50%).

Theoretical fouled ballast specimens were designed for the Bouwer-Rice Large Particle Correction Procedure (discussed later). Phase-relationship calculations were used to determine the minimum measure of fouling material required to meet criteria for the procedure (also discussed later) and for the specimen to have a relative ballast density of 80.0 percent (the maximum density constructible in the Large TRIM without breaking the stone). The minimum fouling was calculated at 32.5% mass passing the 9.52 mm sieve (32.5% fouled); this was rounded up to 35% base on a trial sample prepared in the lab. Values of 50% and 60% fouled were chosen arbitrarily because relative density becomes a mute measurement at these levels of fouling: the ballast become suspended within the fouling material at these levels of fouling.

After design, all fouled ballast specimens were characterized using the SFI and the VCI. The Selig Fouling Index value ( $F_1$ ) (Selig and Waters 1994) is defined as:

$$F_1 = P_4 + P_{200} \quad \text{Equation 3.1}$$

where  $P_4$  is the percent mass passing the No. 4 sieve (4.75 mm), and  $P_{200}$  is the percent mass passing the No. 200 sieve (0.075 mm). The VCI (Indraratna, Su, & Rujikiatkamjorn, 2011a) is:

$$VCI = \frac{1 + e_f}{e_b} \cdot \frac{G_f}{G_b} \cdot \frac{M_b}{M_f} \quad \text{Equation 3.2}$$

where  $e_f$  is the void ratio of the fouling material,  $e_b$  is the void ratio of the ballast aggregate,  $G_f$  is the specific gravity of the fouling material,  $G_b$  is the specific gravity of the ballast aggregate,  $M_b$  is the mass of the ballast aggregates, and  $M_f$  is the mass of the fouling material.

### 3.4 TRIM Testing

The TRIM test (Wayllace & Lu, 2012) was used to measure SWCCs on: 14 specimens of fouling material (prepared from the 14 samples of fouling material, one each), on the 22% SP fouled ballast specimen, and on the 50% SP fouled ballast specimen. The size of the flow-cell that came standard with the TRIM was 66.0 mm tall and 61.8 mm in diameter. This 66.0 mm x 61.8 mm flow-cell will be called the ‘small cell’ throughout the rest of this thesis. The small cell was used to test specimens molded from the samples of fouling materials because the largest particle in the cell could be no bigger than 1/6<sup>th</sup> of the cell diameter for the physical and mechanical properties of the specimen to be independent of the specimen size, (Hu, et al., 2011). Particles that were too large were temporarily removed before the test. Details of the TRIM apparatus and testing procedure are provided by Wallace and Lu (2012).

In this study, two HAE ceramic discs were used in the TRIM: a 1-bar (~ 100kPa) high-flow disc and a 3-bar (~ 300kPa) standard disc (Soilmoisture Equipment Corp., 2020). The 1-bar disc had a higher permeability which facilitated faster testing for sand samples. The 3-bar disc had a higher air entry which enabled the use of higher testing pressures for testing clay and silt samples. The hydraulic properties for each HAE disc, as specified by the manufacturer, are listed in Table 3.1. Photographs of the small flow cell and one HAE disc are shown in Figure 3.2; where Figure 3.2a is the assembled small flow cell and Figure 3.2b shows the yellow colored HAE disk sitting in the base of the flow cell.

**Table 3.1: Hydraulic Properties of HAE Porous Discs (Soilmoisture Equipment Corp., 2020)**

Air Entry (bar)	van Genuchten Parameters				Saturated Hydraulic Conductivity (cm/s)
	$\alpha$ (1/cm)	n	$\theta_s$	$\theta_r$	
3	0.00015	7	0.34	0.07	2.5E-07
1	0.0008	7	0.45	0.07	8.6E-06

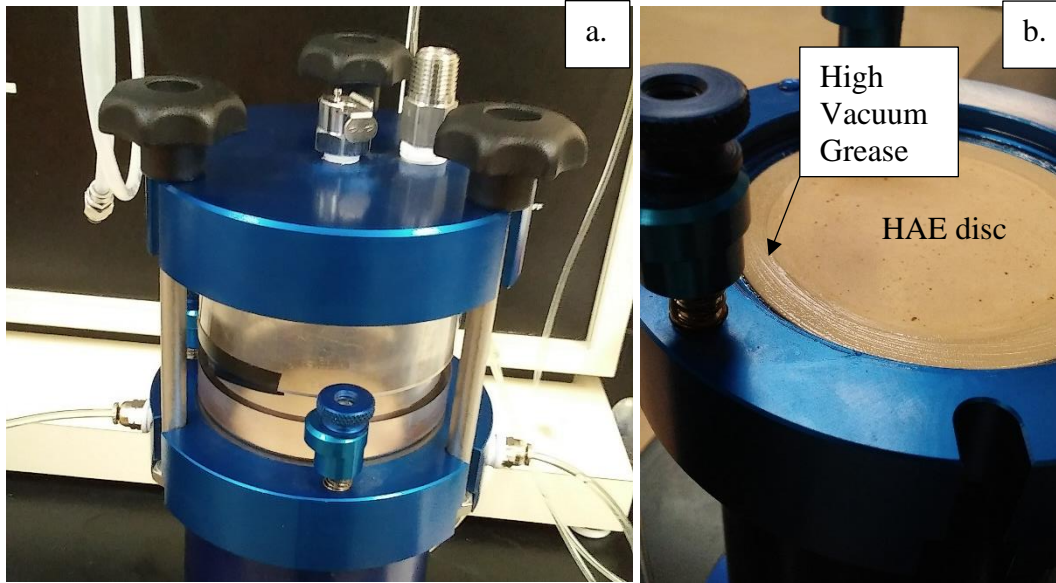


**Figure 3.2: a) Small TRIM flow cell and b) HAE disc in the base.**

Saturation of the HAE discs was confirmed by mass. The surface dry mass of each disc was measured at intervals of 4+ hours, and saturation was confirmed by a stable saturated-surface-dry mass. It was important to make sure all sealing surfaces were completely clean of debris to prevent leaks when assembling the flow cell. High vacuum grease was used to help prevent leaks (e.g., Figure 3.2b). A pass/fail leak test was performed before each test (Wayllace and Lu, 2012): the flow cell was gradually pressurized at 10-25 kPa increments over 20 min. intervals. If the mass of water on the balance (indicating water flow) was stable for a minimum of 20 minutes at each increment, then the flow cell passed the leak test. While conducting these leak tests, the cell pressure was never permitted to exceed 90% of the air entry pressure of the saturated HAE disc.

Specimens were prepared by compacting 170.0 g of dry ballast fouling material into the small cell and to a target dry density of  $1.65 \text{ g/cm}^3$ . This target value of dry density was selected by taking the average of the minimum dry density of the coarser materials (i.e. processed ballast breakdown) and maximum dry density of the finer materials (i.e., ballast fouling material removed from fouled ballast samples). The maximum density was the highest density achievable in the small cell without breaking the ceramic HAE disc. The minimum dry density of the ballast breakdown (sands) averaged  $1.52 \text{ g/cm}^3$ ; the maximum dry density of the fouling materials containing fines was  $1.79 \text{ g/cm}^3$ . Most of the sandy specimens could be compacted to the target density via patting the side of the flow cell by hand. The finer specimens required compaction in three lifts with a 25.4 mm diameter rod. Compacting specimens to a height of 34.0 mm made the dry density of most of the specimens near to the target dry density.

Dry soil placed in the TRIM had the potential to draw moisture out of the HAE disc. To prevent desaturation of the HAE disc during specimen compaction, a valve which controlled water flow between the balance reservoir and the flow-cell's base plate was left open. This allowed the compacted specimen to draw water from the balance reservoir through the HAE disc rather than drawing water out of the disc. This also allowed the mass of water imbibed by the dry specimen during compaction to be measured and recorded.

During specimen saturation, water was drawn from the mass balance reservoir via suction pressure; the suction pressure was supplied by a vacuum pump. The suction applied to the specimen was regulated through the pressure panel and never permitted to exceed 14 in. Hg ( $\sim 47 \text{ kPa}$ ) to avoid breaking the HAE disc. Permeant water was not deaired prior to specimen imbibement. The total mass of water imbibed by the specimen was monitored and recorded. To include the water imbibed by the dry specimen during compaction the mass balance was not tared

between completion of specimen compaction and the start of vacuum induced saturation. A thin film of water observed at the top of the specimen visually indicated complete saturation. Equation 3.3 was used to calculate the mass of water needed to saturate the specimen

$$M_{w-sat} = V_t \cdot \rho_w - \frac{M_s}{G_s} \quad \text{Equation 3.3}$$

where  $M_{w-sat}$  is the mass of water required to saturate the specimen (g),  $V_t$  is the total volume of the specimen in  $\text{cm}^3$ ,  $\rho_w$  is the density of water ( $0.9982 \text{ g cm}^{-3}$  at  $20^\circ\text{C}$ ),  $M_s$  is the mass of dry fouling material compacted into the flow cell (g), and  $G_s$  is the specific gravity of the fouling material. A similar calculation was performed to evaluate the saturated volumetric water content for each specimen; this was one of several hydraulic parameters used later in the procedures for modeling SWCCs.

The two-step transient outflow portion of the TRIM test was conducted following the testing procedures specified by Wayllace and Lu (2012). In this study, the first pressure step was never set below 0.6 kPa because the pressure regulator of the apparatus could not maintain a steady state pressure below 0.6 kPa. Pressures used during the first step ranged between 0.6 kPa and 7 kPa. The second pressure step was never permitted to exceed 90% of the air entry value of the HAE discs. From experience and some trial/error, pressures of 80 kPa and 250 kPa were most appropriate for the second step when using the 1-bar and 3-bar HAE discs, respectively. Each pressure step was terminated after the flux of water leaving the specimen had reduced to 0.05 g/hr (Eching & Hopmans, 1993). Most of the specimens drained quickly at the start of each pressure step; therefore, data were logged at 10 second intervals for the first hour of each step and then at every five minutes through to the end of each step. Specimens were tested only in the drying state. Quantifying hysteresis was determined to be outside of the scope of this project, but it may be of interest to future researchers. Outflow testing took three to seven days per specimen.



Transient outflow data were corrected for diffused air displacement as well as evaporation. Corrections for the diffused air are specified by Wayllace and Lu (2012), but evaporation is not. Under normal laboratory conditions, the rate of evaporation from the balance reservoir averaged 0.1 g/day. Given this environmental factor, and that most specimens released between 1.4 and 6.9 grams of water in the first pressure step over a half-day to three-day period. Ignoring evaporation when using the apparatus at K-State could result in erroneous measurements. Data collected at each pressure step after water flux reduced to 0.05 g/hr were trimmed off. After corrections and trimming, a minimum of 100 data points (typically 300+) were sampled from the corrected outflow data and used later as an objective function for modeling SWCCs via an inverse method. More points were sampled from areas of rapid mass change to preserve the shape of the curve. An example objective function is shown in Figure 3.3. The transparent 'x' marks are the sampled data points. This specimen had a saturated volumetric water content (Sat.) of approximately 37.0%. The specimen was forced to release a small portion of its pore water by applying the first pressure step. The second pressure step quickly drains the specimen to a near residual state (Res.). The horizontal part of each step shows that the volumetric water content had stabilized prior to changing the testing pressure. The darker parts of the curve show how a higher concentration of data points were used to accurately capture its shape.

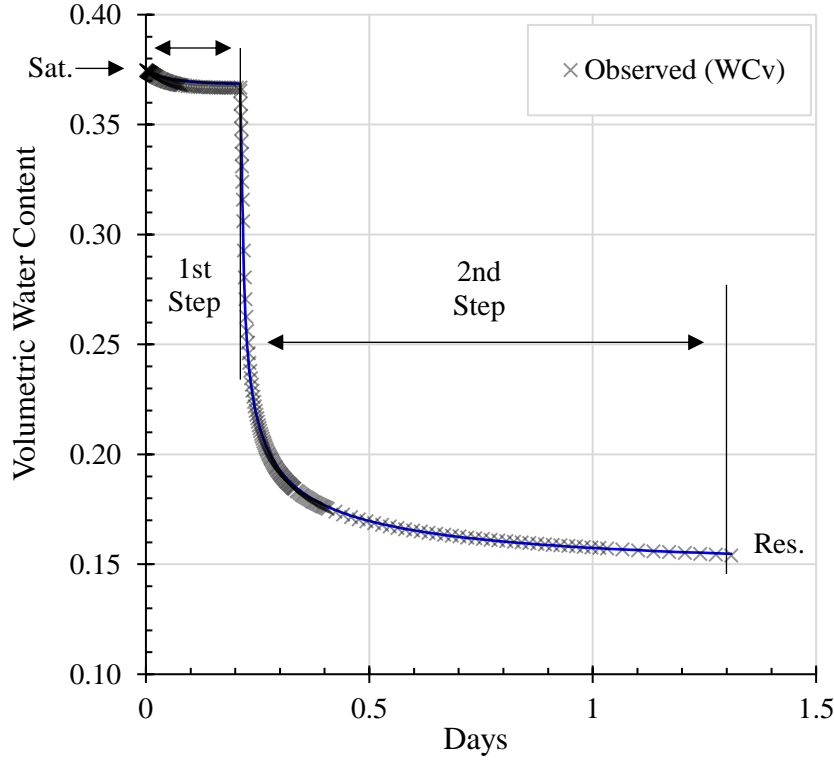


**Figure 3.3: Example Objective Function from TRIM.**

At the end of each transient outflow test, each specimen was removed from the small flow cell, and the gravimetric water content was measured following ASTM D2216. The gravimetric water content was later converted to volumetric water content using Equation 3.4:

$$\theta = \frac{w \cdot \rho_d}{\rho_w} \quad \text{Equation 3.4}$$

where  $\theta$  is the volumetric water content,  $w$  is the gravimetric water content,  $\rho_d$  is the dry density of the soil, and  $\rho_w$  is the density of water. This provided an exact volumetric water content of the specimen corresponding to the end of the second pressure step and served as the upper boundary for another hydraulic parameter used to model the SWCC: residual volumetric water content.

Saturated hydraulic conductivity was a third parameter used for modeling the SWCCs. Saturated hydraulic conductivity was measured on three representative fouling materials. Material #5 (a poorly graded sand which can be seen in Figure A.2 of Appendix A) was selected as a

representative for the sand materials and was tested in a rigid wall permeameter following ASTM D5856 with one deviation: the permeant water was not deaired. The specimen was prepared by compacting 788 g of dry material into a 63.5 mm diameter rigid wall permeameter to a dry density of 1.66 g/cm<sup>3</sup>. The 15 cm tall specimen was saturated by imbibement of tap water; water was drawn up through the base plate and porous stone. Permeation was conducted using the constant head method; the specimen was tested under  $60 \pm 2$  cm of head.

Materials #12 and #13 were selected in this study as representative materials for estimating the permeability of sands with fines and clay materials, respectively. They were tested in flexible wall permeameters in accordance with ASTM D5084 with no deviations from the standard. Due to the soils clay like behavior, the specimens from the TRIM test remained intact during removal from the TRIM. They also survived drying during the water content measurement; therefore, they were directly used for permeability measurements. Each thin wall permeameter was assembled while the specimen was completely dry. After assembly, the dry specimen was subject to a confining stress of 10 kPa. Deaired water was flushed through the bottom of each specimen, driving air out of the pores, out the top of the specimen, and to the back pressure (BP) sensor. The sensor's bleed port was left open to let air leave the system as water replaced it. A pressure head differential of 1.5 kPa was used across each specimen to flush out the air. After flushing the air from the specimens, they were subject to incrementally increased back pressure and cell pressure causing the remaining air in the specimen to dissolve into the permeant water. The B-value measurements for the respective specimens were 1.00 and 0.99 at back pressures of 584 and 565 kPa, respectively. Permeation of these specimens was conducted using the increasing tailwater pressure method (Method C, ASTM D5084). Flow was induced by hydraulic gradients of 5.1 and 19.5, respectively.

Inverse modeling of SWCC's was performed using Hydrus 1D software and the van Genuchten – Mualem model. The van Genuchten model is defined by Equation 3.5 and Equation 3.6 (Van Genuchten, 1980):

$$\theta(h) = \theta_r + \left[ \frac{\theta_s - \theta_r}{1 + (\alpha|h|)^n} \right]^m \quad \text{Equation 3.5}$$

$$K(h) = K_s \frac{[1 - |\alpha h|^{n-1}(1 + |\alpha h|^n)^{-m}]^2}{(1 + |\alpha h|^n)^{m/2}} \quad \text{Equation 3.6}$$

where  $\theta(h)$  is the SWCC,  $\theta_r$  is the residual volumetric water content,  $\theta_s$  is the saturated volumetric water content,  $h$  is the suction head (cm),  $K(h)$  is the hydraulic conductivity function,  $K_s$  is the saturated hydraulic conductivity (cm/s),  $n, m$  and  $\alpha$  are empirical fitting parameters where  $m$  and  $\alpha$  can be approximated with  $m = 1 - 1/n$  and  $\alpha = 1/(\text{air entry})$  (1/cm).

In general, the inverse modeling process followed the simplified three-step process described herein; a more detailed description of the process can be found in the TRIM Manual (SoilWater Retention LLC, 2018). The first step was to specify a hydraulic model to be used (e.g., the van Genuchten-Mualem Model) as well as to import data: the corrected outflow data and data describing the soil specimen and the HAE disc. All data for each HAE disc was taken from Table 3.1 except for the saturated hydraulic conductivity. The HAE disc saturated hydraulic conductivity was measured during each leak test in accordance with ASTM D5856. Data describing the fouling material included: porosity, specimen dimensions, and bounded hydraulic model parameters (i.e.,  $\theta_s, \theta_r, K_s, n$ , and  $\alpha$ ). In the second step, the hydraulic model and the imported data were used to obtain a numerical solution of Richards' Equation (Richards, 1931):

$$\frac{\partial \theta(h)}{\partial h} \frac{\delta h}{\delta t} = \frac{\delta}{\delta z} \left[ K(h) \frac{\delta h}{\delta z} \right] - \frac{\delta K(h)}{\delta z} \quad \text{Equation 3.7}$$

where  $\theta(h)$  is the SWCC,  $h$  is the suction head (cm),  $z$  is the depth into the soil (cm, oriented positive downward), and  $K(h)$  is the hydraulic conductivity function. Given appropriate boundary

conditions, the numerical solution of Richards' Equation can be used to predict the transient outflow of the specimen. An example finite difference solution of Richard's Equation is documented in Appendix A where a backward implicit method with explicate linearization was used to predict the transient outflow of one ballast fouling material. In the third step, the sum of squared errors (SSQ) between the predicted and measured objective functions was calculated. Steps two and three were executed iteratively while hydraulic parameters (i.e.,  $\theta_r$ ,  $K_s$ ,  $n$ ,  $m$  and  $\alpha$ ) were optimized between each iteration, minimizing variation between the two objective functions. Root mean squared error (RMSE) and the regression coefficient ( $R^2$ ) were also calculated at the end of optimization. For this study, an  $R^2$  value in excess of 0.95 was considered an ideal fit so long as the optimized fitting parameters were a close match to typical values found in literature (e.g., Kool, Parker, & Van Genuchten, 1985; Wayllace & Lu, 2012; Bareither & Benson, 2013). Fitting parameters were also verified with calculated/measured values (i.e., volumetric water contents and saturated hydraulic conductivity). Uniqueness of fit was confirmed by checking model dependency on the initial hydraulic parameters (those used to start the optimization process); if the model converged on the same results using different initial values of  $\theta_r$ ,  $K_s$ ,  $n$ ,  $m$  and  $\alpha$ , then results were considered unique (Wayllace & Lu, 2012).

Figure 3.4 summarizes the drying state TRIM procedures. In the diagram, the far left shows suction increments being applied to the specimen from above and water flowing out the bottom through the HAE stone. The second part shows that as the increments are applied, the water outflow ( $Q$ ) is recorded vs. time. Next, the data from the TRIM are used as inputs for numerical inverse modeling (i.e., the third part of the diagram), which produces the SWCCs (the last part of the diagram).

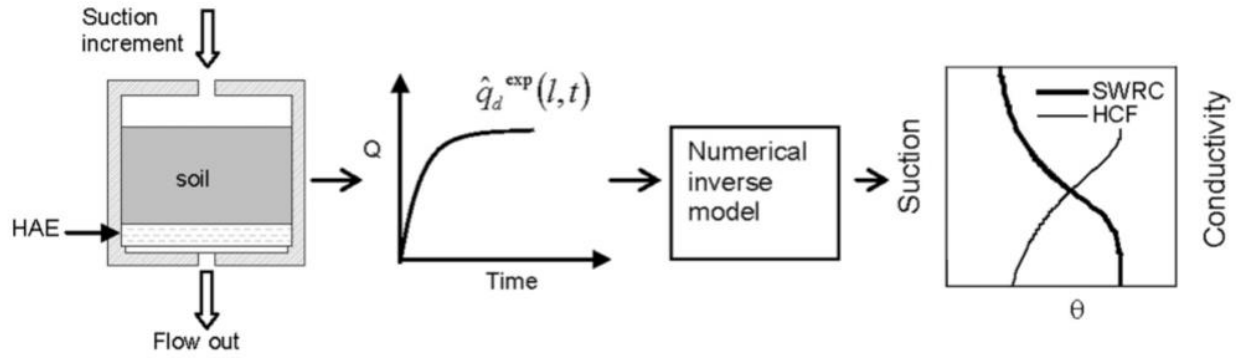


**Figure 3.4: Diagram of the TRIM, Drying State. Diagram Credit: (Wayllace & Lu, 2012)**

A custom TRIM apparatus was used to measure SWCCs of specimens with ballast aggregate; the apparatus and procedures used were like those used on fouling materials. Dissimilarities in the apparatus include: the use of a custom-built large flow-cell (Figure 3.5a and b), and the use of a higher capacity mass balance and balance reservoir. Procedures were different in two ways: an alternate method was used for molding specimens and a higher flux was used for termination of each pressure step. The large flow cell was 255 mm in diameter and 178 mm tall. Specimen height was restricted to 127 mm so that the specimen surface could be seen through the acrylic housing. Cell dimensions limit aggregate size to 42.5 mm (ASTM D5856 ; Hu, et al., 2011) which is appropriate for AREMA #4 graded ballast, where the largest nominal particle size is 38.1 mm (AREMA, 2019). Figure 3.5 shows the size of the large flow cell compared to the small cell (a) and compared to ballast aggregates (c); it also shows a fouled ballast being tested in the large apparatus (b).

Regarding the mass balance, the capacity of the first balance for the TRIM apparatus was 220 g. Typically, the total mass of water required to saturate large specimens was in excess of 2.00 kg. Therefore, the first balance was replaced with a balance having a 2.20 kg capacity. Inherent to this adjustment, precision was reduced from  $\pm 0.01$  g to  $\pm 0.1$  g. Measurement bias was calculated

at less than 0.05% of the total mass of effluent measured during the first step of the TRIM test and less than 0.01% during the second step which is not expected to hinder results.

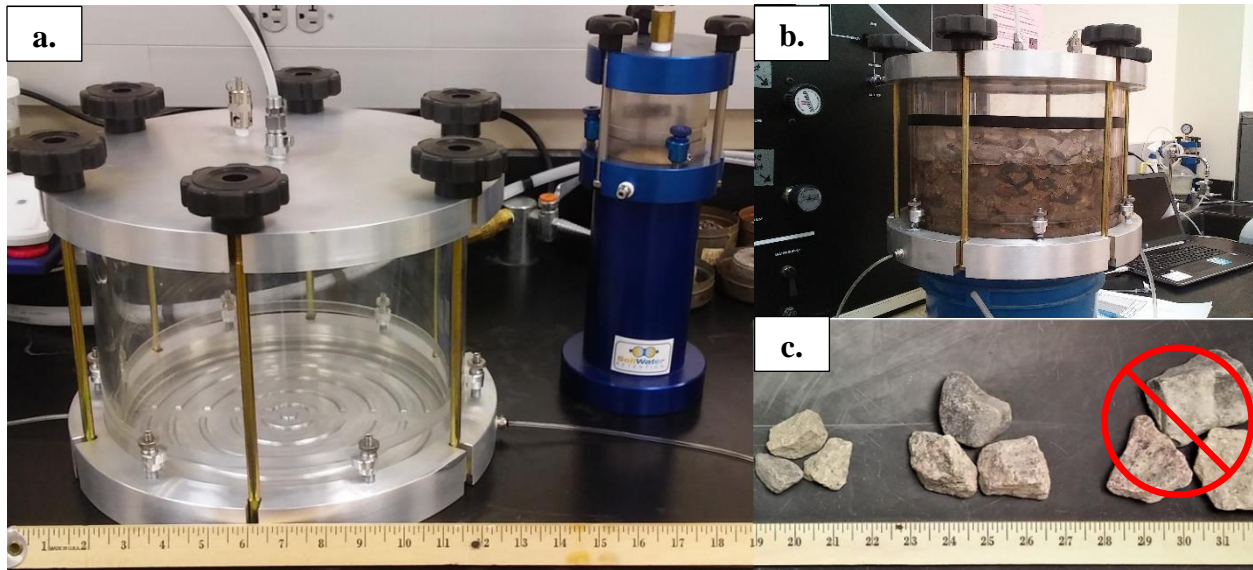


**Figure 3.5: a) Large & small TRIM cells, b) large cell with fouled ballast, c) sample ballast aggregate. Scale unit is inches.**

A specimen of ballast fouling material was tested in the large TRIM. The results were compared to that of the small TRIM test to validate the use of the large flow cell and new balance for coarse textured materials. The specimen was prepared by pouring approximately 10.8 kg. of dry fouling material into the large cell, 1 kg. at a time. The specimen compacted itself under its self-weight to an average dry density of  $1.73 \text{ g/cm}^3$ . The dry density of the specimen tested in the small cell was  $1.70 \text{ g/cm}^3$ . Saturation was facilitated by a vacuum pressure of 10 in. Hg ( $\sim 33.9 \text{ kPa}$ ); 2.11 kg. of water was required to saturate the specimen. The first pressure step was facilitated by gravity because the specimen drained without added pressure. The second step was set to 100 kPa (a 3-bar HAE stone was used for this test). Each pressure step was terminated when the flux condition measured less than 0.1 grams/hr. The elapsed time from the start of the first step to the end of the second step was 12 days. The entire specimen was used when measuring the final water

content, and finally, the SWCC measured using these methods was compared to the SWCC measured using the small cell.

After validation, the two fouled ballast specimens (22% SP fouled and 50% SP fouled ballast) were remolded in the large flow cell using dry materials. Each specimen was constructed in five lifts; each lift had a thickness of approximately 38.1 mm. Each lift was compacted to a target dry density by hand. The apparatus was not shaken, nor was the specimen tamped. Rather, the materials were slightly rolled and patted by hand until a target height (derived from the target density) was achieved. TRIM testing commenced after molding the specimen. Saturated hydraulic conductivity could not be measured directly on these specimens with the equipment available at K-State. Figure 3.6 was used to estimate the initial guess and boundary conditions of saturated hydraulic conductivity for both fouled ballast specimens and for modeling of the their SWCCs. While direct measurements of saturated hydraulic conductivity are best, the methods from Wallace (2003) worked well for estimating the saturated hydraulic conductivity of the TRIM tested fouled ballast.

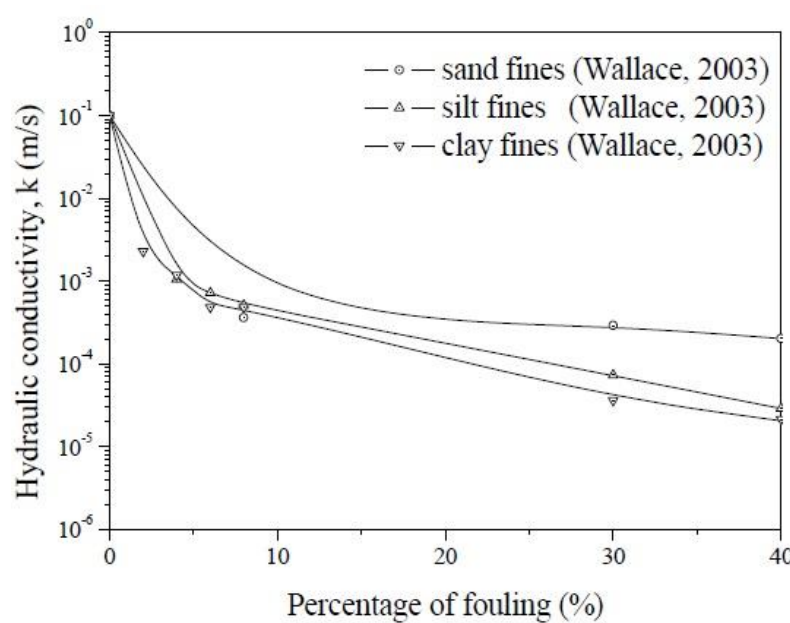


**Figure 3.6: Hydraulic Conductivity of Fouled Ballast versus Percentage Fouling (Wallace, 2003).**



### 3.5 Theoretical SWCC of Fouled Ballast.

Fouling conditions were selected using criteria of the Bouwer-Rice Large Particle Correction Procedure (Bareither & Benson, 2013). The procedure requires that ballast voids be filled with fouling material (i.e., VCI = 1.00), and that the dry density of fouling material in the ballast voids be the same as the fouling material tested in the TRIM (Bareither & Benson, 2013). Phase-relationship calculations were used to determine the minimum measure of fouling material required to meet these criteria for a specimen with an 80.0 percent relative density of ballast. The minimum was 32.5% fouling, or 48.1 percent of the clean ballast mass. The minimum was rounded up to 35% fouling base on constructability. Values of 50% and 60% fouling were chosen arbitrarily; relative density becomes a mute measurement at these levels of fouling due to the suspending of ballast within the fouling material. A relative density of 82.0% was the maximum feasible relative density achievable in the large TRIM without risk of breaking the large HAE disc in the base. A test specimen at each fouling degree was molded in the lab to confirm constructability; bulk density and voids in ballast were measured in accordance with ASTM C29, method A.

The specific gravity of coarse aggregates was measured according to ASTM C127 and the average specific gravity was calculated for the whole fouled ballast mixture using Equation 3.8:

$$G_{s,fb} = \frac{1}{\left(\frac{P_b}{G_{s,b}} + \frac{P_f}{G_{s,f}}\right)} \quad \text{Equation 3.8}$$

where  $G_{s,fb}$  is the average specific gravity of the fouled ballast,  $P_b$  is the mass percentage of the ballast fraction,  $P_f$  is the mass percentage of the fouling material fraction,  $G_{s,b}$  is the average specific gravity of the ballast fraction, and  $G_{s,f}$  is the average specific gravity of the fouling

material fraction. For determination of ballast density, the minimum and maximum dry density of AREMA #4 graded ballast was measured in accordance with ASTM D4253 and D4254.

Twenty-one SWCCs were calculated for highly fouled ballast using the Bouwer-Rice Large Particle Correction Procedure (Bouwer & Rice, 1984). The Bouwer-Rice Large Particle Correction Procedure uses Equation 3.9 to predict the volumetric water content of a fouled ballast ( $\theta_{fb}$ ) at any suction head (i.e., the SWCC),

$$\theta_{fb}(h) = (1 - V_R) \cdot \theta_f(h) \quad \text{Equation 3.9}$$

where  $\theta_{fb}(h)$  is the SWCC of the fouled ballast,  $V_R$  is the volumetric fraction of ballast aggregate in the total specimen volume, and  $\theta_f(h)$  is the SWCC of the fouling material.  $V_R$  is calculated by,

$$V_R = \frac{\frac{M_{s,b}}{\rho_w \cdot G_{s,b}}}{V_t} \quad \text{Equation 3.10}$$

where  $M_{s,b}$  is mass of the ballast aggregate solids (g),  $\rho_w$  is the density of water ( $\sim 0.998 \text{ g/cm}^3$ ),  $G_{s,b}$  is the specific gravity of the ballast fraction, and  $V_t$  is the total volume of the fouled ballast specimen ( $\text{cm}^3$ ). Bareither and Benson (2013) note that the Bouwer-Rice Large Particle Correction Procedure operates on three assumptions; first, the large aggregates (i.e., ballast in this study) are assumed to have negligible inter-particle moisture retention. Second, the aggregate voids are assumed to be filled completely with finer materials (i.e., fouling materials in this study). Third, the dry density of the finer materials in the bulk specimen (i.e., fouled ballast in this study) is assumed to be the same as the dry density of the finer materials measured on (i.e., ballast fouling materials in this study). A SWCC predicted using the Bouwer-Rice Large Particle Correction Procedure was validated with SWCC of a replicate specimen tested in the large TRIM.

## Chapter 4 - Results

### 4.1 Material Characterization

The grain size distribution (GSD) curves of fouling materials are shown in Figure 4.1. Refer to Table 4.1 for the USCS of each material shown in Figure 4.1.

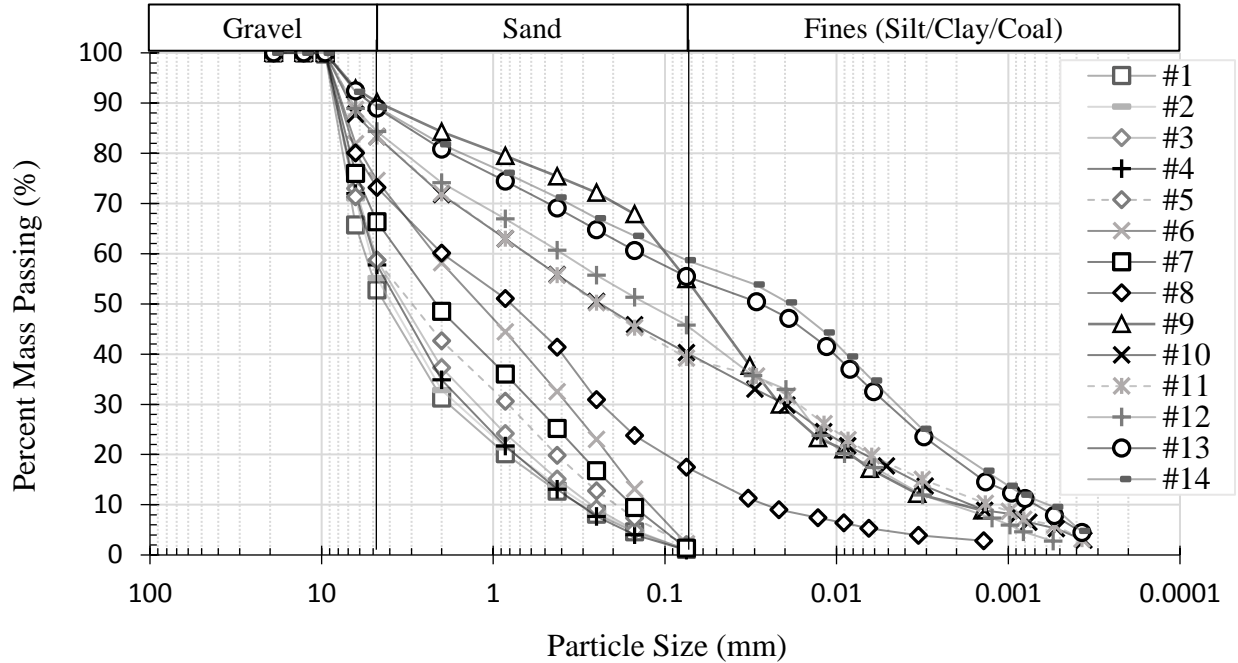


**Figure 4.1: GSD curves of fouling materials.**

The specific gravity ( $G_s$ ) of sands averaged 2.62 with a variance of 0.046. The specific gravity of materials No. 11 and 14 were low compared to the other materials (2.58 and 2.56, respectively). The USCS abbreviation and the measured specific gravity for each sample are listed in Table 4.1. Samples 10 through 14 behaved like clayey-silty-sand (SC-SM) or lean clay (CL), but they may be silty-sand or silt; the coal in them could produce their clayey behavior: plasticity and liquidity properties (Dombrow, Huang, & Tutumluer, 2009).

**Table 4.1: Geotechnical Properties of Fouling Materials**

<b>No.</b>	<b>1</b>	<b>2</b>	<b>3</b>	<b>4</b>	<b>5</b>	<b>6</b>	<b>7</b>
USCS	SW	SW	SW	SW	SP	SP	SP
$G_s$	2.66	2.63	2.63	2.60	2.62	2.62	2.63
<b>No.</b>	<b>8</b>	<b>9</b>	<b>10</b>	<b>11</b>	<b>12</b>	<b>13</b>	<b>14</b>
USCS	SM	ML	SC-SM	SC-SM	SC-SM	CL	CL
$G_s$	2.60	2.70	2.67	2.58	2.66	2.60	2.56

***Fouled Ballast***

While the large TRIM cell was being developed, 21 theoretical fouled ballast mixtures were designed for the Bouwer-Rice Large Particle Correction Procedure. The procedure was used to model theoretical SWCCs of fouled ballast. When the large TRIM cell was ready, two fouled ballast specimens were tested in it, a 22% and 50% SP fouled ballast. The 50% SP fouled ballast specimen was prepared to have essentially the same properties as one of the 21 theoretical ballast specimens... Figure 4.2 shows the GSD of an example theoretical fouled ballast, along with the gradation of the clean ballast and fouling material used in its design. The GSD curves for all the fouled ballast (theoretical and physical) are available in Appendix A. A representative fouling material was selected from each kind of fouling material based on their USCS and SWCCs, and each representative fouling material was used for the Bouwer-Rice Large Particle Correction Procedure. The geotechnical properties and fouling characteristics for three of the theoretical fouled ballast mixtures are listed in Table 4.2; the first fouled ballast listed in Table 4.2 describes the same fouled ballast shown in Figure 4.2. The specific gravity of all the fouled ballasts measured between 2.68 and 2.58; ballast with coal materials had the lowest specific gravity. The complete record of geotechnical and fouling properties of the fouled ballast is available in Appendix A.

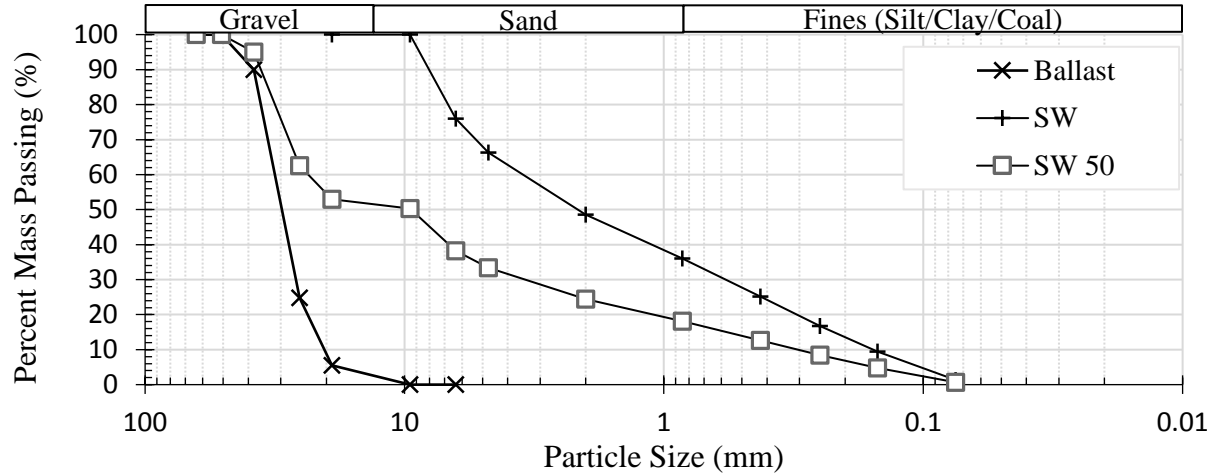


**Figure 4.2: Example GSD of Clean Ballast, SW, and a Ballasts 50% fouled with SW.**

**Table 4.2: Example Geotechnical Properties of 50% Fouled Ballast.**

No.	Percent Fines	$D_{50}$ (mm)	$D_{10}$ (mm)	$C_c$	$C_u$	$FI$ (%)	$G_s$
SW 50	0.6	8.60	0.315	1.86	75.2	34	2.64
SM 50	8.7	9.84	0.105	1.56	226	45	2.62
CL-2 50	29.4	9.65	0.00203	0.188	1170	74	2.60

Saturated hydraulic conductivity ( $K_s$ ) was measured on representative SP, SC-SM, and CL samples (i.e., fouling materials No. 5, 12, and 13). The  $K_s$  of the SP material was used as an approximate value for SW and SM. This approximation worked well for modeling the SWCCs of all three type of sands (i.e., SP, SW, and SM); therefore,  $K_s$  was not measured for the SW or SM materials. Poorly graded sand had a  $K_s$  approximately two to three orders of magnitude higher than that of the clayey-silty sand and lean clay, respectively. The results of the  $K_s$  measurements and each sample's dry density ( $\rho_d$ ) during testing are listed in Table 4.3.

**Table 4.3: Saturated Hydraulic Conductivity measured on Fouling Materials.**

USCS	$K_s$ (cm/s)	$\rho_d$ (g/cm <sup>3</sup> )
SP	6.90E-02	1.66
SC-SM	1.47E-04	1.68
CL	2.69E-05	1.67

Geotechnical properties of the clean ballast material are listed in Table 4.4: maximum and minimum dry unit weight ( $\gamma_d$ ) and void ratio ( $e$ ), and specific gravity ( $G_s$ ). The specific gravity of the ballast material is identical to that of the processed ballast breakdown (i.e., the SW and SP fouling materials).

**Table 4.4: Geotechnical Properties of Clean Ballast**

$\gamma_{d,max}$ (pcf)	$\gamma_{d,min}$ (pcf)	$e_{max}$	$e_{min}$	$G_s$
97.4	83.0	0.985	0.691	2.64

### ***Thermogravimetry***

The results of TGA for the three SC-SM and two CL samples are shown in Figure 4.3a and Figure 4.3b. Because these samples were collected from track where coal is frequently transported, they were suspected to be fouled with coal dust. Figure 4.3a shows the mass loss of each material in correlation to temperature. The results are normalized to a 10 mg sample size for eased comparison. Mass loss prior to 100°C is likely due to evaporation of water. The mass loss from the portion passing a No. 40 sieve (0.420 mm) of material No. 10 and No. 13 was each approximately 8.5%, while the mass loss for materials No. 11, 12, and 14 was approximately 10%, 12%, and 15%, respectively. Figure 4.3b shows the rate of mass loss peaking for all five materials at temperatures of 460°C and 690°C, approximately. These peaks indicate volatilizing of bituminous and anthracite coal (Sahu, Sarkar, Chakraborty, & Adak, 2010; Zhang, et al., 2015). Results of a test conducted on a sampled portion passing a No. 200 sieve (0.074 mm) showed that coal particles were dust sized (i.e., smaller than 0.074 mm); the results of the portion passing a No. 200 sieve is available in Appendix A.

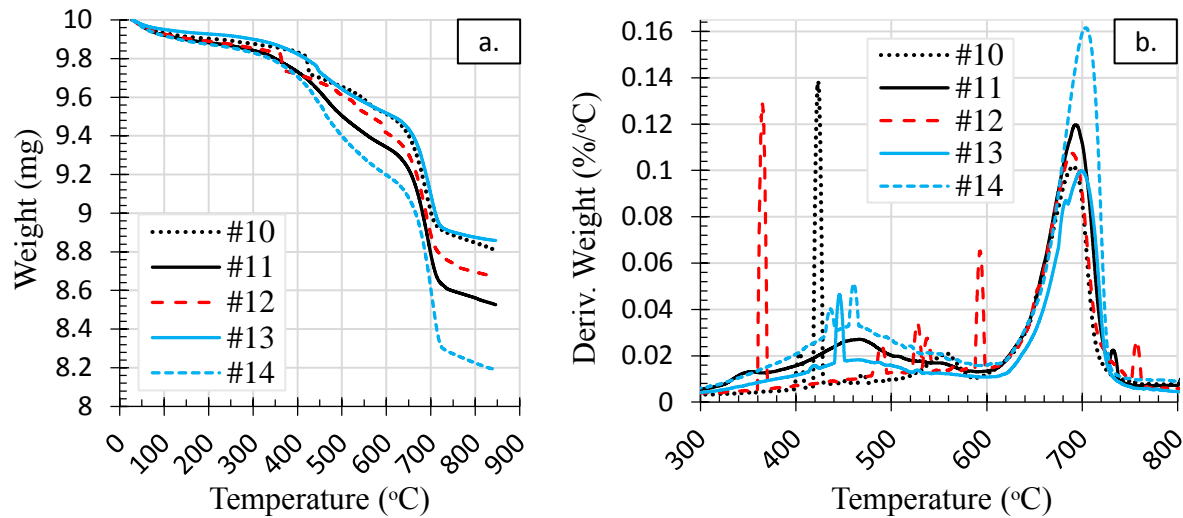


**Figure 4.3: TGA results for fouling materials #10-#14.**

## 4.2 SWCC Results

The SWCC results of the fouling materials (i.e., materials GSD shown previously in Figure 4.1) are presented first in this section, followed by the predicted SWCCs of theoretical fouled ballast (calculated via the Bouwer-Rice Large Particle Correction Procedure, example materials GSD shown previously in Figure 4.2). Lastly, the SWCCs measured directly on fouled ballasts via the large flow-cell and TRIM are presented (i.e., the physical specimens tested with ballast aggregate and fouling materials in them).

### *SWCCs of Ballast Fouling Materials via the small TRIM*

SWCCs were measured and modeled on 14 ballast fouling materials. The SWCCs of seven select fouling materials are shown in Figure 4.4; all 14 SWCCs are available in Appendix A along with a table of all their hydraulic parameters. The seven SWCCs shown in Figure 4.4 were selected to represent each USCS description available in the material inventory. Two CL specimens were included because the SWCC results varied greatly between the two despite their similar USCS description.

In Figure 4.4, the sand specimens (i.e., SP, SW, SM) show low resistance to drainage: the saturated phase of the SWCCs (right vertical side of the curves) transitions into a draining condition (horizontally oriented portion of the curves) at a relatively low suction heads compared to the other specimens. The average air entry of these materials was 1.04 kPa (~10.6cm H<sub>2</sub>O). The three sand specimens also drained more completely compared to the other specimens. In other words, the draining phase of their SWCCs transition into the residual phase (left vertical side of the curves) at lower volumetric water contents compared to the clayey-silty sands (SC-SM), low plasticity silt (ML), and lean clays (CL). The average residual volumetric water content of the sands was 6.44%.

All SC-SM and CL specimens had coal in them. The clayey-silty sands (SC-SM) with coal had a sharp (nearly horizontal) drainage phase like the well graded and poorly graded sands with gravel (SW and SP); however, these specimens required approximately six times the suction head to initiate drainage. The average air entry for the SC-SM with coal was 6.54 kPa (~66.8 cm H<sub>2</sub>O). They also held nearly three times more pore water than the SW and SP specimens in the residual phase. The average residual volumetric water content of the SC-SM with coal was 16.5 %. The second of the sandy lean clays (CL) with coal (CL-2 hereafter) and sandy low plasticity silt (ML) required even higher suction heads to begin the draining phase; their air entry values were 20.0 kPa (corresponding to a head of 2.03 m) and 44.5 kPa (~4.54 m), respectively. They did hold less residual pore water at the end of the draining phase; but only when exposed to high suction heads (15.5% and 12.1% at suction heads in excess of 1000 kPa). The SWCC of CL-1 looks more like that of the clayey-silty sand (SC-SM) with coal. The CL-1 specimen had an approximate coal content of 8.5% of P<sub>40</sub> materials whereas the CL-2 had an approximate coal content of 15%.



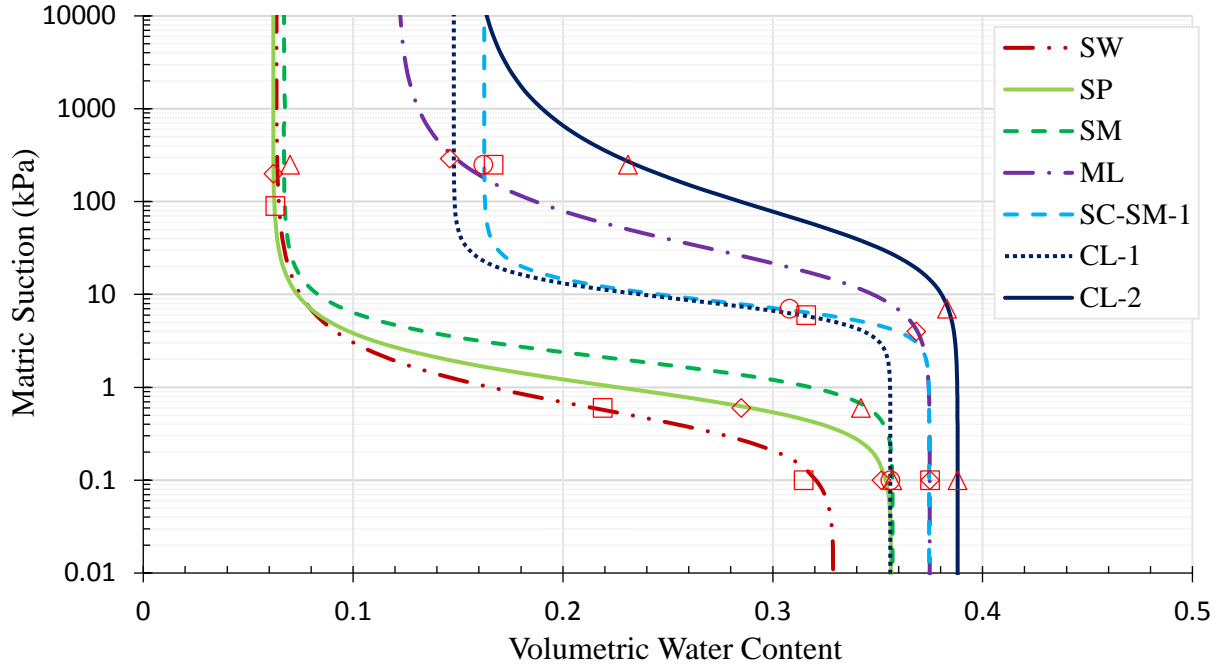


**Figure 4.4: SWCCs of Fouling Materials.**

The van Genuchten hydraulic parameters for the SWCCs shown in Figure 4.4 are listed in Table 4.5. The sandy specimens were the densest of the those tested, whereas the clayey specimens were the least dense. All specimens were within  $0.1 \text{ g/cm}^3$  of the target dry density ( $1.65 \text{ g/cm}^3$ ). The least dense specimens had the highest saturated volumetric water contents.

**Table 4.5: Summary of Hydraulic Parameters of Fouling Materials**

No.	$\theta_r$	$\theta_s$	$\alpha \text{ (cm}^{-1}\text{)}$	$n$	$m$	$K_s \text{ (cm/s)}$	$R^2$	$\rho_d \text{ (g/cm}^3\text{)}$
SP	0.063	0.329	0.238	1.98	0.496	2.56E-02	1.00	1.75
SW	0.062	0.356	0.128	2.26	0.557	6.39E-03	1.00	1.70
SM	0.067	0.357	0.0587	2.61	0.616	5.10E-04	1.00	1.70
ML	0.121	0.375	0.00492	1.82	0.451	8.70E-05	1.00	1.68
SC-SM-1	0.162	0.374	0.0130	3.50	0.714	9.52E-05	1.00	1.67
CL-1	0.148	0.356	0.0124	3.50	0.714	4.51E-05	0.99	1.67
CL-2	0.155	0.388	0.0022	1.61	0.379	3.50E-05	0.98	1.57

#### ***SWCCs of Fouled Ballast via the Bouwer-Rice Large Particle Correction Procedure.***

The seven representative fouling materials, whose SWCC's are shown in Figure 4.4, were used for the Bouwer-Rice Large Particle Correction Procedure. The predicted SWCCs are shown in

Figure 4.5 through Figure 4.7. The Bouwer-Rice Large Particle Correction Procedure assumes that the finer material within each bulk specimen (i.e., the fouling material in each fouled ballast) has the same suction properties as the scalped material (i.e., the fouling material tested without ballast). Therefore, the predicted SWCCs adopt the air entry pressure ( $1/\alpha$ ) and other fitting parameters (i.e.,  $n$  and  $m$ ) of their respective fouling material (Bouwer & Rice, 1984). While those properties remained constant, the saturated and residual volumetric water contents and the slope of the horizontal part of the SWCCs changed. The fluctuating features are highlighted here. Each figure is dedicated to a degree of ballast fouling:

In Figure 4.5, all the SWCCs for 35% fouled ballast are plotted over the same range of suction head as those in Figure 4.4, but they have shifted in position: toward the far-left side of the volumetric water content axis. The predicted  $\theta_s$  for all the specimens were between 14.0% and 19.0%. The ballast fouled with CL-2 had the highest  $\theta_s$  at 18.4%; SP had the lowest  $\theta_s$  at 15.0%. All specimens had a  $\theta_r$  less than 8.00%. The theoretical  $\theta_r$  for ballast fouled with clean sands (i.e., SP, SW) and silty sand (SM) are approximately the same at 2.91%. Ballast that were 35% fouled with SC-SM and CL-2 were predicted to have a  $\theta_r$  of roughly 7.50%. Predicted saturated and residual volumetric water contents for 35% fouled ballast are summarized in Table 4.6.

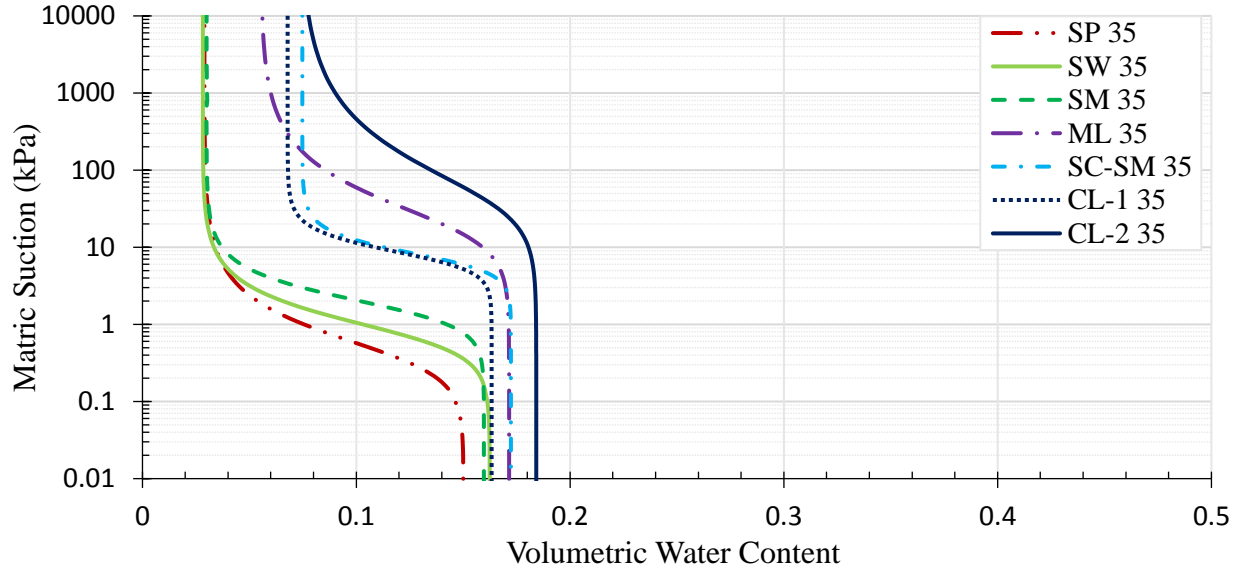


**Figure 4.5: Theoretical SWCCs of 35% fouled ballast. Predicted using the Bouwer-Rice Large Particle Correction Procedure.**

**Table 4.6: Saturated and Residual Volumetric Water Contents, 35% Fouled Ballast**

Name	SP 35	SW 35	SM 35	ML 35	SC-SM 35	CL-1 35	CL-2 35
$\theta_s$	0.150	0.162	0.160	0.172	0.172	0.163	0.184
$\theta_r$	0.0290	0.0283	0.0300	0.0555	0.0748	0.0679	0.0751

All the SWCCs for 50% fouled ballast in Figure 4.6 plot a little further to the right along the volumetric water content axis compared to the 35% fouled ballast. The ballast fouled with SP has the lowest  $\theta_s$  of all the 50% fouled ballast specimens, predicted at 20.1%. The three ballasts fouled with well and poorly graded sand (SP and SW) and silty sand (SM) were predicted to have the lowest  $\theta_r$ , averaging at 3.89%. The SWCC of the SC-SM fouled ballast was predicted to have the highest  $\theta_r$  of 9.96%. Lastly, the CL-2 fouled ballast was estimated to have the highest  $\theta_s$  at 24.3%, and a  $\theta_r$  of 9.92%, nearly the highest  $\theta_r$ . Predicted saturated and residual volumetric water contents for 50% fouled ballast are listed in Table 4.7. At a suction head of 1.00 kPa ( $\sim 10.2$  cm H<sub>2</sub>O), the SP and SW fouled ballast are predicted to release approximately half of their pore water where all the other fouled ballast are predicted to be either fully saturated or nearly saturated. At a suction head of 10.0 kPa (1.02 m H<sub>2</sub>O) the SP, SW, and SM fouled ballast were predicted to

be fully drained while the SC-SM and CL-1 fouled ballast specimens were predicted to release half of their drainable pore water. The ballast specimens fouled with CL-2 and ML were predicted to remain saturated at the same suction head. These draining trends are observed in the predicted SWCCs at each fouling degree predicted using the Bouwer-Rice Large Particle Correction Procedure.

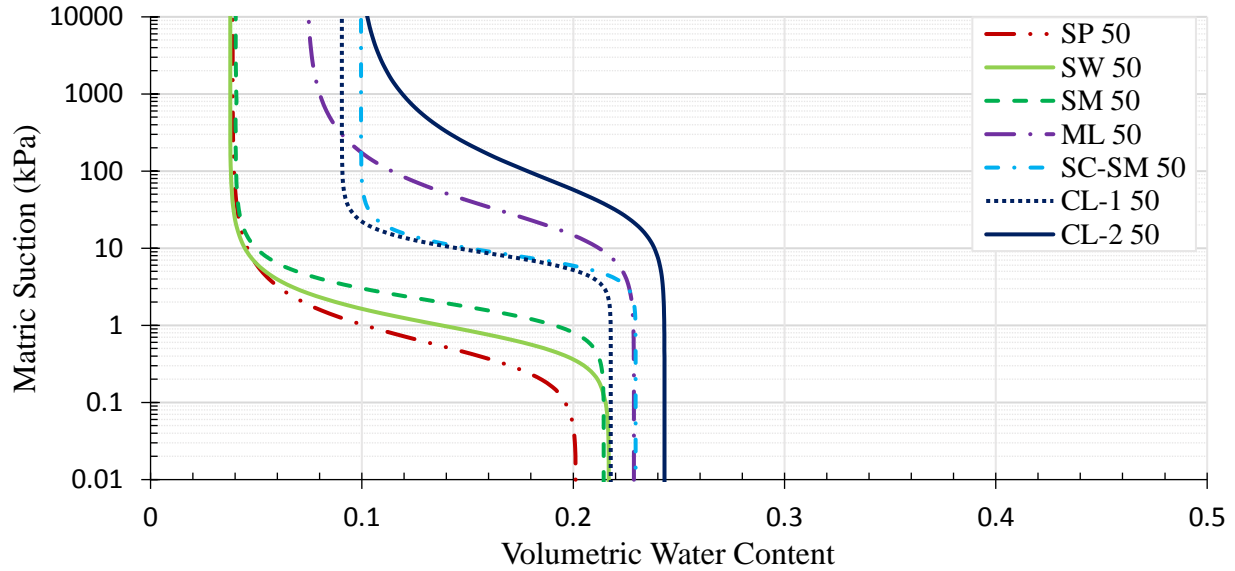


**Figure 4.6: Theoretical SWCCs of 50% fouled ballast. Predicted using the Bouwer-Rice Large Particle Correction Procedure.**

**Table 4.7: Saturated and Residual Volumetric Water Contents, 50% Fouled Ballast**

Name	SP 50	SW 50	SM 50	ML 50	SC-SM 50	CL-1 50	CL-2 50
$\theta_s$	0.201	0.217	0.214	0.229	0.230	0.218	0.243
$\theta_r$	0.0388	0.0377	0.0403	0.0741	0.0996	0.0905	0.0992

In Figure 4.7, all the SWCCs for 60% fouled ballast plot yet a little further toward the right along the volumetric water content axis compared to the lesser fouled ballasts: 35% and 50%. The predicted saturated and residual volumetric water contents for the SWCCs in Figure 4.7 are listed in Table 4.8. Seven additional plots are available in Appendix A; they show the SWCCs at 35%, 50%, and 60% fouling where each plot is dedicated to a single type of fouling material. These plots illustrate how the unsaturated behavior of a ballast changes as the percent fouling changes.

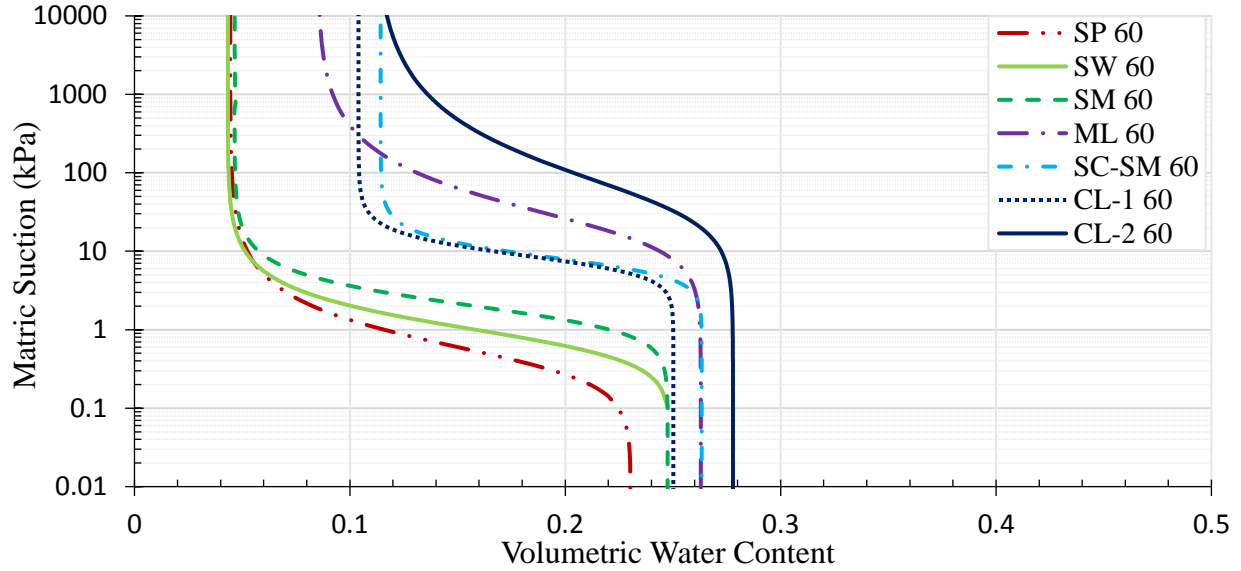


**Figure 4.7: Theoretical SWCCs of 60% fouled ballast. Predicted using the Bouwer-Rice Large Particle Correction Procedure.**

**Table 4.8: Saturated and Residual Volumetric Water Contents, 60% Fouled Ballast**

Name	SP 60	SW 60	SM 60	ML 60	SC-SM 60	CL-1 60	CL-2 60
$\theta_s$	0.230	0.249	0.247	0.263	0.263	0.250	0.278
$\theta_r$	0.0445	0.0434	0.0465	0.0852	0.114	0.104	0.113

***Proof of Concept: Use of Bouwer-Rice Large Particle Correction Procedure to Predict Fouled Ballast SWCCs.***

The SWCCs of two similar fouled ballast are shown in Figure 4.8: one from the Bouwer-Rice Large Particle Correction Procedure (blue dashed line) and another measured using the large TRIM apparatus (black solid line). Both were designed to a percent fouled condition of 50%. When molding the specimen into the large TRIM apparatus, care was not put into regulating the density of fines in the ballast voids; therefore, this is a rough comparison. Comparing results, the two SWCCs are similar in shape and are in the same general location within the plot. The fitted hydraulic parameters are summarized in Table 4.9. The two specimens had identical air entry values. The major difference between the two specimens are the saturated volumetric water content and bulk dry density. The differences calculate out to 4.8% volumetric water content and 0.13 g/cm<sup>3</sup>, respectively, with the TRIM specimen being the least dense.

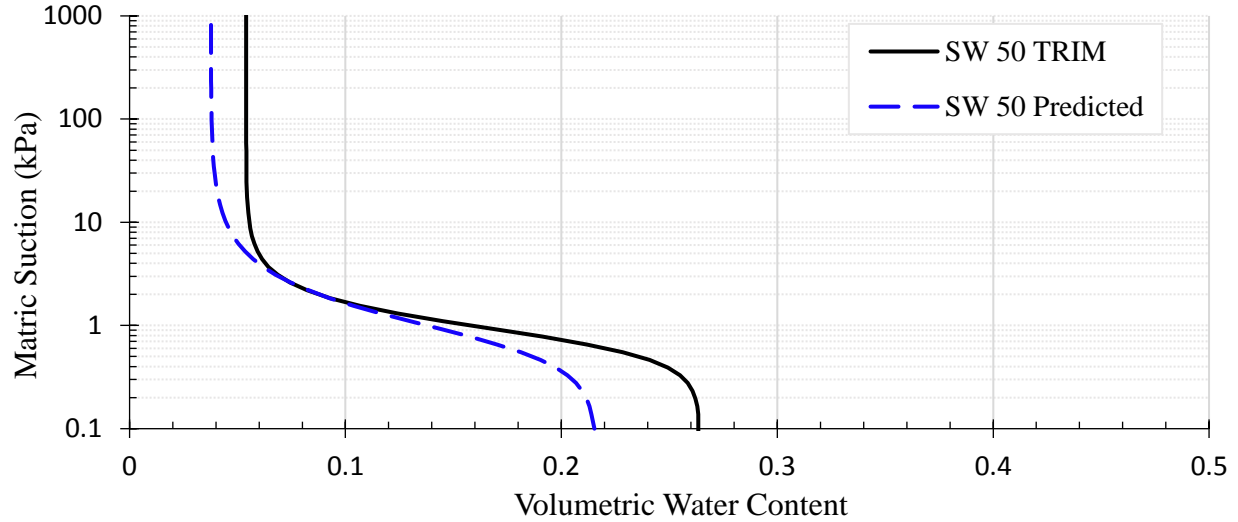


**Figure 4.8: Comparison of SWCCs of Fouled Ballast - Large TRIM Experiment to Brouwer-Rice Prediction.**

**Table 4.9: Hydraulic Parameters for Ballast 50% fouled with SW: Measured and Predicted**

No.	$\theta_r$	$\theta_s$	$\alpha \left( \frac{1}{cm} \right)$	$n$	$m$	$K_s \left( \frac{cm}{s} \right)$	$R^2$
TRIM	0.054	0.264	0.122	2.97	0.664	1.14E-02	1.00
Predicted	0.037	0.216	0.128	2.26	0.557	-	-
No.	$\rho_d \left( \frac{g}{cm^3} \right)$	$P_{3/8} \text{ (%)}$	$FI \text{ (%)}$	$VCI$			
TRIM	1.94	50	36	1.00			
Predicted	2.07	50	36	1.00			

**Validation: Using the Large TRIM Apparatus to Measure SWCCs of Unsaturated Materials.**

Results of the large TRIM were verified through comparison with results of the small TRIM apparatus. Two SWCCs for the well graded sand with gravel are shown in Figure 4.9. The green solid line is the SWCC measured using the small apparatus; the dashed black line is the SWCC measured using the large apparatus. The two SWCCs are sigmoidal in shape and have similar air entry values. The saturated and residual water content are different between the two specimens as is the density.

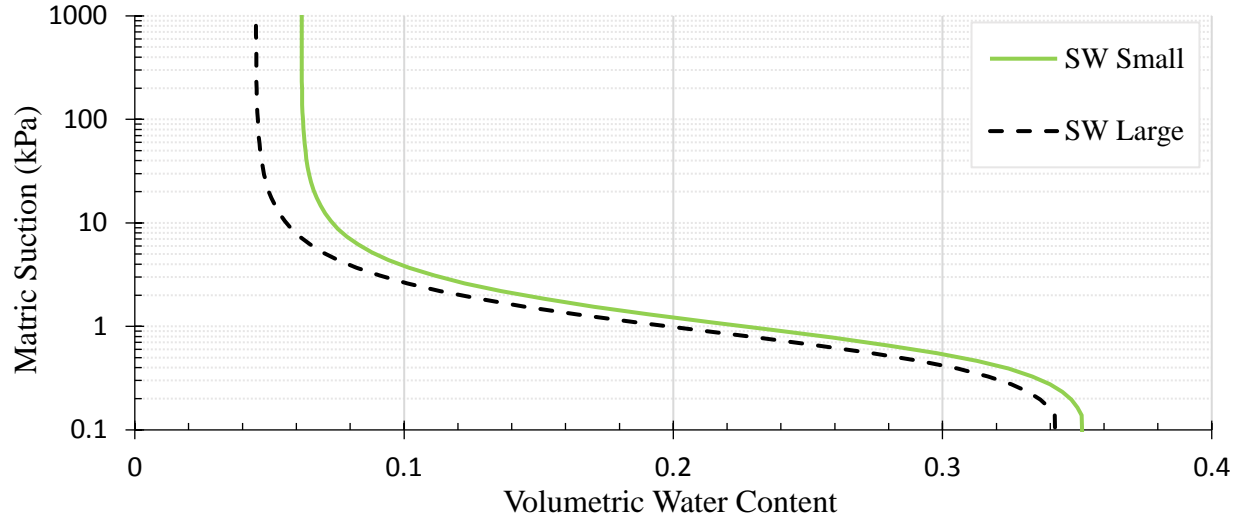


**Figure 4.9: Large TRIM SWCCs, Validation of the Large TRIM Experiment.**

The fitted parameters for the two SWCCs in Figure 4.9 are summarized in Table 4.10. All the fitting parameters are identical with one exception: the saturated hydraulic conductivity of the smaller specimen was 0.0063 cm/s, whereas that of the larger specimen was lower at 0.0018 cm/s. This was likely the result of reduced porosity and varied pore connectivity (i.e., increased specimen density and altered particle arrangement). The difference in average density between the two specimens was 0.04 g/cm<sup>3</sup>. Given the similarities between the two results, the large TRIM test worked for measuring the SWCC of the poorly graded sand (SP). It would be good to have additional tests on other materials to fully validate the method (e.g., on clay and silt).

**Table 4.10: Hydraulic Parameters of Fouling Material SW, Validation of Large TRIM Experiment**

No.	$\theta_r$	$\theta_s$	$\alpha \left( \frac{1}{cm} \right)$	$n$	$m$	$K_s \left( \frac{cm}{s} \right)$	$R^2$	$\rho_d \left( \frac{g}{cm^3} \right)$
SW Small	0.062	0.357	0.128	2.26	0.557	6.39E-03	1.00	1.70
SW Large	0.045	0.341	0.147	2.21	0.548	1.80E-03	1.00	1.74

#### ***Measuring SWCCs of Fouled Ballast via the Large TRIM.***

Three SWCCs were measured using the large apparatus and TRIM. One SWCC was for a fouling material. Two SWCCs were for fouled ballast: a 50% fouled ballast and a 22% fouled ballast. All three SWCCs are shown in Figure 4.10. The dashed line is the SWCC of the fouling material, a

poorly graded sand with gravel; this material was used to create both fouled ballast specimens. The dotted line and solid line are the SWCCs of the 22% and 50% fouled ballast, respectively. The three SWCCs are similar in shape; this is to be expected given that the same fouling material was used for each specimen. The 22% fouled ballast had an air entry value of 0.34 kPa (3.48 cm H<sub>2</sub>O) and a residual volumetric water content of 5.4% at approximately 2 kPa of suction head (20.4 cm H<sub>2</sub>O). The 50% fouled ballast had an air entry value of 0.80 kPa (8.20 cm H<sub>2</sub>O) and residual volumetric water content of 5.4% at a 9 kPa (91.8 cm H<sub>2</sub>O) of suction head. The fitted hydraulic parameters for the SWCCs in Figure 4.10 are listed in Table 4.11.

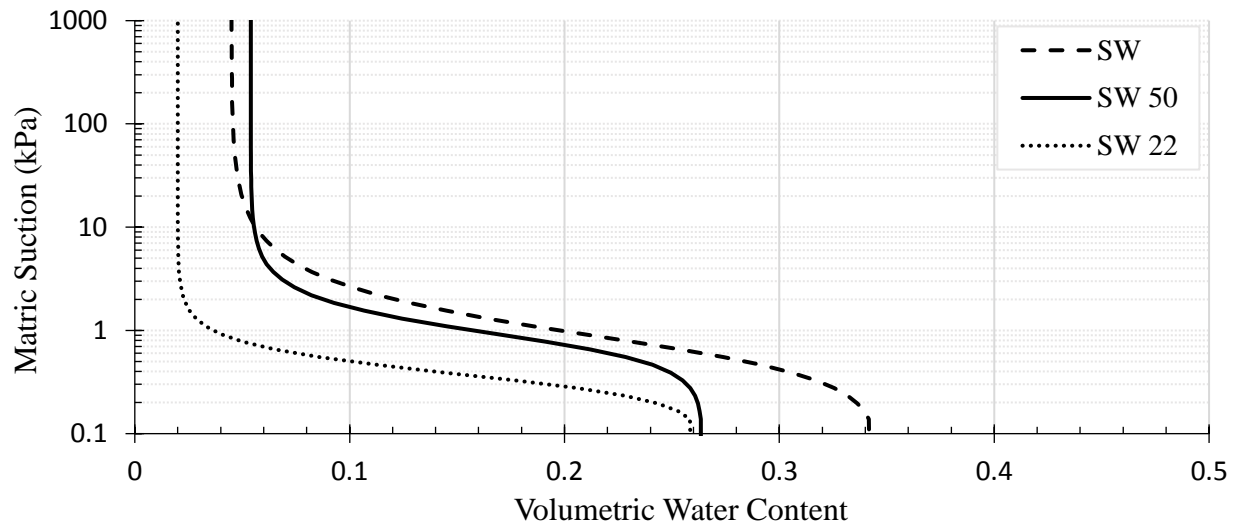


**Figure 4.10: SWCCs of Fouled Ballast, Results of the Large TRIM Experiments.**

**Table 4.11: Hydraulic Parameters of Fouled Ballast, Results of the Large TRIM Experiments**

No.	$\theta_r$	$\theta_s$	$\alpha \left( \frac{1}{cm} \right)$	$n$	$m$	$K_s \left( \frac{cm}{s} \right)$	$R^2$
SW	0.045	0.341	0.147	2.21	0.548	1.80E-03	1.00
SW 50	0.054	0.264	0.122	2.97	0.664	1.14E-02	1.00
SW 22	0.020	0.266	0.287	3.50	0.714	8.98E-03	0.99
No.	$\rho_d \left( \frac{g}{cm^3} \right)$	$P_{3/8}$ (%)	$FI$ (%)	$VCI$			
SW	1.74	NA	NA	NA			
SW 50	1.94	50	36	1.00			
SW 22	1.94	22	15	0.65			



## Chapter 5 - Discussion

### 5.1 Ballast Fouling Materials

Geotechnical analysis of the fouling materials show that the donated fouled ballasts were fouled with a wide variety of soil: fine gravel, sands, silts, and clays. Ballast history, color of fouling material, specific gravity, and TGA results strongly suggest that five of the ballast fouling materials contained coal dust. Suction properties of sands, silts, and clays are well established in geotechnical and environmental soil science literature. The SWCCs on SP, SW, SM, and ML materials presented in this Thesis are comparable to those measured on soils of the same USCS by previous researchers (e.g., Eching & Hopmans, 1993; Khaleel & Freeman, 1995; Wayllace & Lu, 2012; Bareither & Benson, 2013; Benson, Chiang, Chalermyanont, & Sawangsuriya, 2014). SWCCs of clean sand (i.e., SP, SW, SM in this study) typically drain over a low/narrow range of suction heads (0-10 kPa) (Benson, Chiang, Chalermyanont, & Sawangsuriya, 2014). Materials with fines in them (i.e., ML in this study) typically drain over a higher and wider range of suction heads than sands (10-1000 kPa) (Eching & Hopmans, 1993; Wayllace & Lu, 2012). Kool et al. (1985) notes that van Genuchten fitting parameters ( $\alpha$  and  $n$ ) range from 0.005 to 0.05 cm<sup>-1</sup> and 1.1 to 3.5 respectively for silt and clay specimens. The  $\alpha$  and  $n$  values for ML in this study were 0.005 cm<sup>-1</sup> and 1.82. Literature on unsaturated characteristics of sands with no fines (e.g., Benson, Chiang, Chalermyanont, & Sawangsuriya, 2014) shows that  $\alpha$  can range from 0.022 cm<sup>-1</sup> to 4.4 cm<sup>-1</sup> and  $n$  can range from 1.13 to 13.1. The average  $\alpha$  and  $n$  values for SP, SW, and SM in this study were 0.13 cm<sup>-1</sup> and 3.68. All the specimens had  $\alpha$  and  $n$  values within their respective ranges; therefore, the results are supported by the literature for these materials. All curves were sigmoidal in shape.

Fityus and Li (2006) showed bimodal suction characteristics of coal grains (size not specified) where interparticle water drains first over low suction heads and the intraparticle water begins to drain at a suction head ranging 60 to 90 kPa. Sharma et al. (1993) showed that mixing coal grains with soil increased the water holding capacity of sandy loam (SM in USCS) and had little effect on or decreased the water holding capacity of loam and silty clay loam (CL in USCS); 80% of the coal granules were larger than 0.5 mm and 7% were smaller than 0.10 mm. Unfortunately, no literature was found on suction characteristics for materials containing coal dust, i.e., coal particles finer than 0.074 mm. The SC-SM and CL materials tested in this research contained varied amounts of coal dust. All SWCCs of specimens with coal dust, except for CL-2, show a mixture of behaviors. Unsaturated SC-SM with coal and CL-1 (which had the least amount of coal) behaved like sand in terms of a narrow pore size distribution. Looking at their SWCCs (Figure 5.1a), they drain over a narrow range of suction heads. The three SC-SM specimens with coal and the CL-1 specimen with coal also have a high air entry value like that of clays and silts. The interparticle pore volume of the coal dust is negligible due to their small particle sizes thus ruling out bimodal suction and/or an increase in air entry due to such pores. In comparison to the sandy specimens (i.e., SP, SW, and SM) the increase in air entry can be partly explained by an increased quantity of fines (e.g., Fredlund & Rahardjo, 1993; Likos & Lu, 2004), but this doesn't explain the variations between SWCCs of materials CL-1 and CL-2 which had identical geotechnical properties.

Tutumluer, et al. (2011; 2008) found that coal has a high affinity for moisture. In connection with the results of CL-1 and CL-2, the more coal dust present in a specimen the more moisture the specimen will soak in and retain. Likos and Lu (2004) found that for idealized grains of uniform spheres, the nominal pore radius decreases as particles pack more closely. They

highlighted the effects of packing order on suction properties showing that theoretical SWCCs of uniform spheres systematically translate upward along the suction axis as particles arrange denser. While the particles in the materials tested in this study were not spherical, the coal has a low specific gravity compared to soil, and specimens with more coal in them can have values of specific gravity lower than those with less coal. Specimen CL-2 had 43% more volatile matter, yet the specific gravity was only slightly lower than CL-1 (specific gravity of 2.56 vs. 2.60, respectively). The reduced specific gravity will cause the particles in CL-2 to be geometrically arranged denser than CL-1 if they were compacted to the same dry density, but their densities were not the same: CL-2 was compacted to a lower dry density than CL-1:  $1.57 \text{ g/cm}^3$  vs.  $1.67 \text{ g/cm}^3$ , respectively. Based on Likos and Lu (2004) and because the gradation and specific gravity of the specimen made from CL-1 was similar to CL-2, the unsaturated behavior of CL-1 was expected to be similar to CL-2. If the SWCCs were not going to be similar, it was expected that CL-1 would have higher suction potential than CL-2 because CL-1 was compacted to a higher density, but both of these expectations were proven false by the observed SWCCs; the following discussion explains what was observed.

The SWCCs of fouling materials containing coal dust (Figure 5.1) suggest that coal dust significantly alters suction properties of unsaturated materials. All specimens containing coal dust were compacted to have similar volume of voids (controlled by dry density); as a result, any change between their SWCCs was primarily caused by changes in fines content (quantity and kind), and soil structure (i.e., particle arrangement). Out of the five specimens containing coal dust, a group of two and a group of three had similar gradations and USCS, while specific gravity fluctuated within the groups with similar gradation. Focusing in on materials CL-1 and CL-2, geotechnical measurements (e.g., Figure 5.1a) proved that the CL-1 and CL-2 specimens were highly similar in

their general quantity of fines (percent of fines being 56% and 59%, respectively) and their fines behavior (USCS being lean clay for both). CL-1 had a similar specific gravity to CL-2 (2.60 vs. 2.56, respectively). These two observations (gradation and specific gravity) suggested that CL-1 and CL-2 would have similar SWCCs. Then, CL-1 was compacted to a higher dry density than CL-2 ( $1.57 \text{ g/cm}^3$  vs.  $1.67 \text{ g/cm}^3$ , respectively) suggesting that CL-1 could have higher air entry and hold more water than CL-2. In Figure 5.1c, the SWCCs show that air entry for CL-1 was lower than CL-2, opposite of what was expected. The air entry of CL-1 is 82% lower than the air entry of CL-2 (7.9 kPa vs. 44 kPa, respectively) which was not expected. CL-1 held less volumetric water than CL-2: 32% less at 10 kPa (0.26 vs. 0.38, respectively) and 48% less at 100 kPa (0.15 vs 0.29, respectively); this is also opposite of what was expected. TGA results (Figure 5.1b) showed that the CL-1 material had 43% less volatile matter than CL-2 (8.5% mass loss vs 15% mass loss, respectively at temperatures between 300 °C and 800 °C). These observations suggest that the coal content had a strong influence on the material's suction characteristics like the air entry.

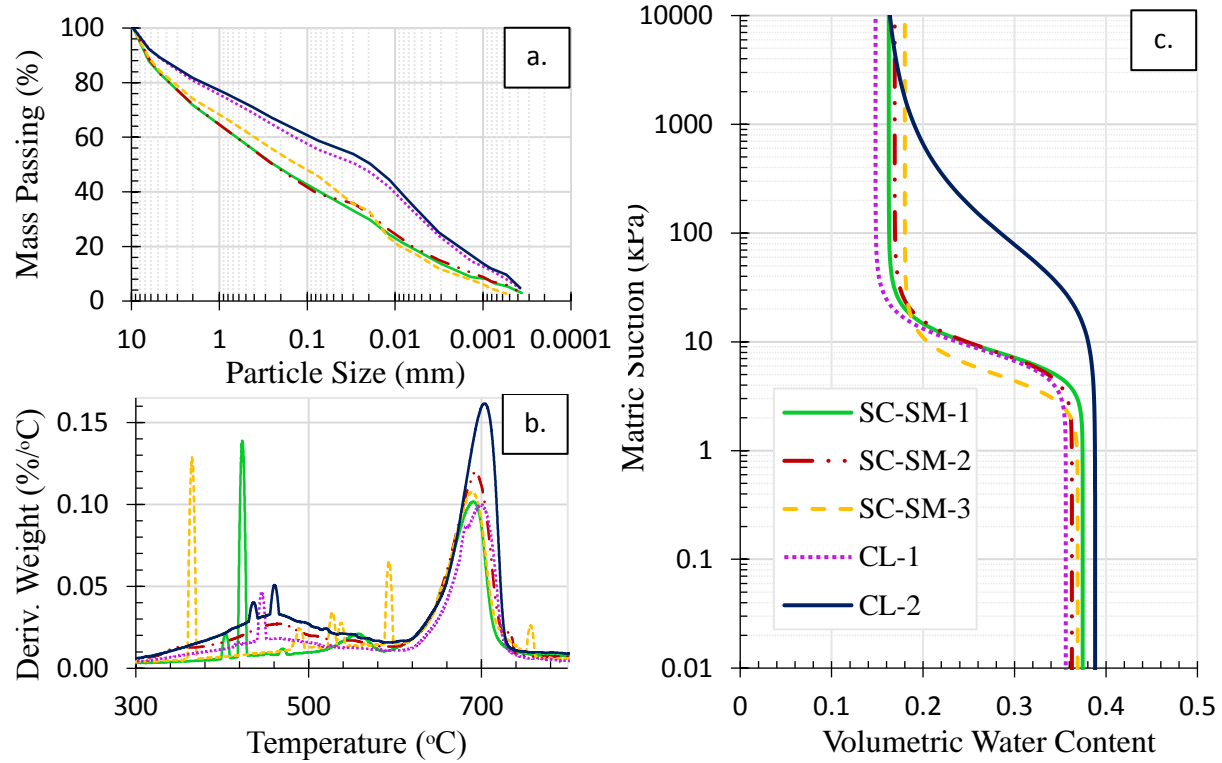


**Figure 5.1: Coal Contaminated Fouling Materials: a) GSD, b) TGA, c) SWCCs.**

## 5.2 Fouled Ballast

Theoretical SWCCs of fouled ballast show that suction properties of fouled ballast are controlled by the fouling material. The total mass and the gradation of ballast aggregate were kept constant within each degree of ballast fouling as shown in Figure 5.2a. All theoretical ballast specimens were designed to have the same void contamination index (1.00), and similar dry density of fouling materials. Therefore, changes in the SWCCs are a function of the degree of fouling and the suction properties of the fouling material (i.e., the type of fouling material). The predicted SWCCs for fouled ballast show that as the degree of fouling decreases in a fouled ballast, the bulk materials SWCC shifts toward lower water contents, and retains the general shape of the scalped fouling material. The granitic ballast have little to no interparticle voids; therefore, the specimen volume occupied by ballast has no pore volume. As a result, for cases where VCI measures 1.00 and the specimen density is kept constant between mixtures, the bulk specimen voids and the saturated

volumetric water content are controlled by the degree of fouling (or inversely, the amount of ballast materials) (e.g., Bareither & Benson, 2013). The degree of fouling controls how much water will saturate the specimen, and the type of fouling material governs the water release characteristics of the fouled ballast (water release characteristics such as the air entry and residual pressure, and the residual water content).

Fouled ballast specimens tested in the large TRIM (i.e., Figure 4.8) suggest that the SWCCs predicted using the Bouwer-Rice Large Particle Correction Procedure are a close approximation. The predicted SWCCs and the measured SWCCs show in theory and empirically that the hydraulic properties (air entry, and residual pressure) of the fouled ballast strongly reflect that of the fouling materials hydraulic properties. For example, the estimated SWCCs in Figure 5.2b show that a 60% fouled ballast will hold 54% more pore water than a 35% fouled ballast under saturated conditions; there is more pore space available in the more fouled ballast specimen where more volume is occupied by a porous network of fouling material as opposed to suspended granitic aggregate. A second example, the estimated SWCCs also show that when the VCI is 1.00 and the dry density of the fouling materials is near  $1.65 \text{ g/cm}^3$ , a ballast fouled with material CL-2 (known to have coal dust) will not begin to drain until exposed to a suction head of 10 kPa (102 cm H<sub>2</sub>O) regardless of the degree of fouling. Because the hydraulic nature of fouled ballast is inherited from the fouling material, the mechanisms altering SWCCs of fouling materials are also influencing the SWCCs of fouled ballast. The ballast fouled with SC-SM and CL (which all contained coal) had higher air entry than the sands (SP, SW, and SM). This is partly because of the increase number of fines but is also because those fines included coal dust. Coal affects the suction response of the fouled ballast as seen by the SWCCs of CL-1 and CL-2 fouled ballast in Figure 5.2b. Recall the previous discussion for fouling materials for a detailed description of the phenomena influencing SWCCs

of CL-1 and CL-2. Large TRIM tests on fouled ballast show that the Bouwer-Rice Large Particle Correction Procedure gives a close estimate of the unsaturated characteristics of these highly fouled ballast.

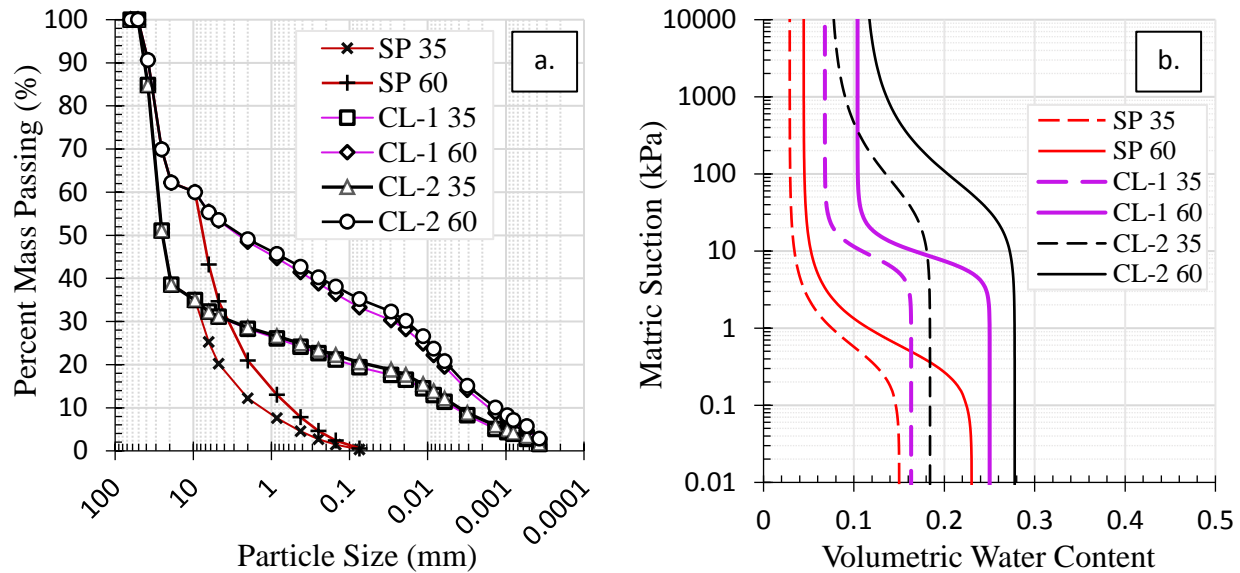


**Figure 5.2: Fouled Ballast: a) GSD, b) SWCCs.**

### 5.3 General Insight and Application.

The predicted and measured SWCCs for fouled ballast specimens (i.e., the Bouwer-Rice Predictions and the large TRIM test results) give insight to the variety of fouled ballast unsaturated characteristics. The SWCC of a 60% SP fouled ballast (solid red line in Figure 5.2b) shows that the specimen will be nearly dry (volumetric water content of 5% at a suction of 10 kPa. The SWCC of a 35% CL-2 fouled ballast with coal dust (dashed dark blue line in Figure 5.2b) shows that specimen will be fully saturated (volumetric water content of 18%) under the same conditions. The comparison of the two specimens applies only to fouled ballast in hydrostatic equilibrium, (an occasional condition in situ), none-the-less it still raises a question: because a 35% fouled ballast can retain more than three times the volumetric water of 60% fouled ballast and under the same geometric and environmental conditions, could their geophysical response be the same? GPR

dielectric measurements are influenced by both parameters: the water content and the fouling conditions: the dielectric response increases as water content increases and it increases as percent fouling increases. Therefore, there could be many combinations of ballast conditions where the dielectric responses could be identical, which supports the difficulties associated with using GPR to monitor fouled ballast. The dielectric measurements must be made to test for common responses at varied fouling and moisture conditions.

Figure 5.2b also shows how much influence the parent fouling material has on the overall unsaturated behavior of the ballast; most notably, how it changes the water holding potential of the specimen at any suction state. Consider specimens of identical fouling conditions, the 35% SP fouled ballast in comparison to the 35% CL-2 fouled ballast: the SP fouled ballast releases 87.5% of its pore water at a suction head of 10 kPa (1.02m H<sub>2</sub>O) while the CL-2 fouled ballast retains 97.8% of its pore water when exposed to an identical suction. Again, this comparison only applies to the hydrostatic state of each specimen: when the pore water has equilibrated with the surrounding environment, but still highlights the influence the type of fouling material has on unsaturated behavior of these specimens.

Results show that an increase in the percent fouling causes an increase in the residual volumetric water content of a fouled ballast specimen. Figure 5.3a and b show that for each fouling material a 60% fouled ballast is estimated to hold more water in the residual state than a 35% fouled ballast. For example, the 60% fouled ballast specimens hold an average of 39% more residual volumetric water than the 35% fouled ballast specimens. Therefore, the degree of fouling influences the residual volumetric water content of fouled ballast. Results also show that saturated volumetric water content increases as fouling increases for ballast specimens fouled to a VCI of 1.0, but this trend is expected to reverse for ballast having a VCI less than 1.0 (when ballast voids



are not filled by fouling material). By engineering intuition, the voids between ballast aggregate will make up the bulk of water storage space in lesser fouled ballast, and as fouling increases (as the voids fill with solids) that storage space will naturally decrease. Thus, saturated volumetric water content is expected to decrease as fouling increases where VCI is less than 1.0.

Figure 5.3 a shows that the type of fouling material influences the residual volumetric water content of a fouled ballast specimen: ballast fouled with ML, SC-SM, and CL are estimated to hold two to three times more residual water than ballast fouled with SP, SW, and SM (0.06 to 0.11 cm<sup>3</sup>/cm<sup>3</sup> retained in the former and 0.03 to 0.05 cm<sup>3</sup>/cm<sup>3</sup> in the latter). Example values from Figures 5.3a and b are listed in Table 5.1.

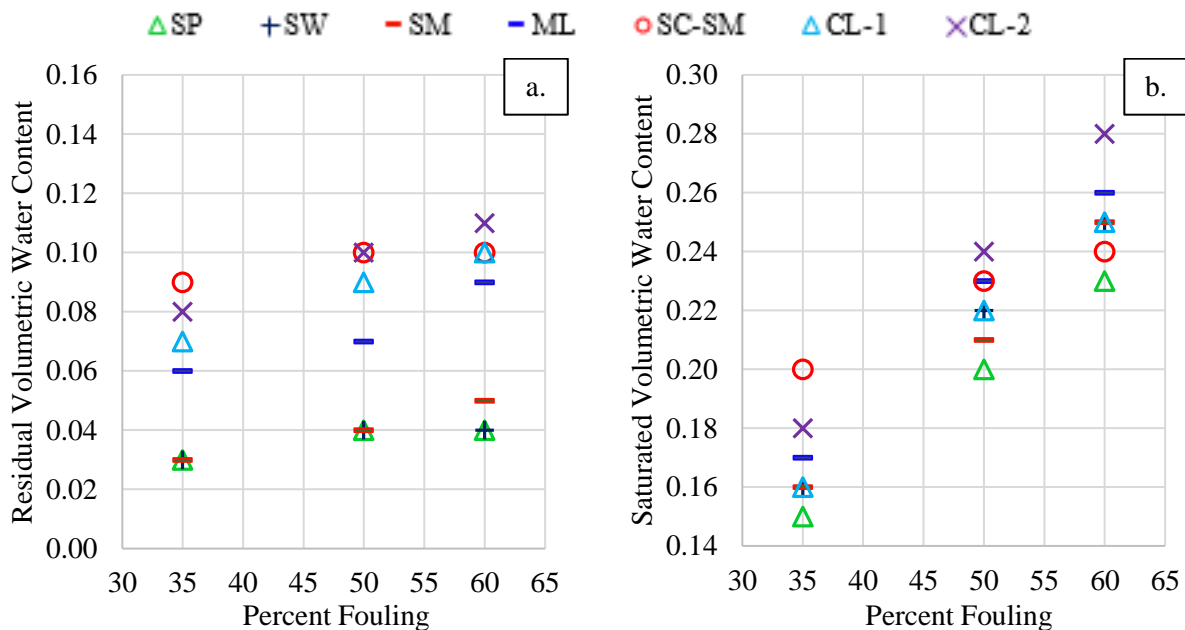


**Figure 5.3:** a) Estimated residual volumetric water content of highly fouled ballast verses ballast percent fouling. b) Estimated saturated volumetric water content of highly fouled ballast verses ballast percent fouling.

**Table 5.1: Example Residual and Saturated Water Contents ( $\theta_r$  and  $\theta_s$ , respectively) in Relation to the Degree of Fouling and Type of Fouling Material**

Degree of Fouling	Fouling Material	
	CL-2	SP
<b>60% Fouled</b>	$\theta_r = 0.11$ $\theta_s = 0.28$	$\theta_r = 0.04$ $\theta_s = 0.25$
<b>35% Fouled</b>	$\theta_r = 0.08$ $\theta_s = 0.18$	$\theta_r = 0.03$ $\theta_s = 0.16$

Based on these results, a ballast layer with high variability in fouling and environmental conditions will have highly variable ballast moisture conditions. This research helps to explain why in situ ballast conditions can yield identical GPR dielectric measurements, and that ambiguity in GPR results makes quantitative interpretations of ballast conditions impossible without additional information. Combined with future research efforts, these results are hypothesized to improve in situ identification of fouled ballast.

## Chapter 6 - Conclusions

Fouled ballast are often an unsaturated material, but have not yet been characterized as such. Therefore, there is need to characterize fouled ballast as unsaturated material. SWCCs are commonly used to characterize unsaturated geomaterials. SWCCs are hypothesized to be useful in decoupling the influence of water and fouling conditions on measured dielectric constant values which would improve in situ identification of fouling using GPR. Therefore, the TRIM (a proven method for measuring SWCCs of soils) was used to measure the SWCCs of ballast fouling materials. The Bouwer-Rice Large Particle Correction Procedure was used to predict the SWCCs of highly fouled ballast at three degrees of fouling for seven fouling materials. The procedure could only be used to predict SWCCs on fouled ballast having a VCI value of one; therefore, its application was limited to highly fouled ballast. A novel method for testing fouled ballast specimens using an enlarged TRIM cell is presented in this thesis; the method was validated by testing a known material and then used to measure one additional SWCC on a moderately fouled ballast (VCI was less than one). All SWCCs in this thesis are drying curves. Measuring wetting curves to quantify hysteresis was determined to be outside of the scope of this project, but it may be of interest to future researchers. In total, this thesis characterizes the unsaturated behavior of 14 fouling materials, 21 theoretical fouled ballast specimens, and two laboratory prepared fouled ballast specimens (a 50% SP fouled ballast and a 22% SP fouled ballast) in desorption (drying). In the future, if the Large TRIM can be validated for silt and clay soils, then it can be used to measure SWCCs of fouled ballast spanning a more comprehensive range of fouling degrees, fouling materials, and environmental conditions (wetting or drying).

SWCCs of fouling materials show that coal fines have measurable influence on water retention. The two CL specimens (known to contain coal) had measurably different SWCCs

because of their different volatile material contents. Estimated SWCCs of fouled ballast show that the unsaturated behavior (e.g., air entry and residual volumetric water content) of a highly fouled ballast (where  $VCI = 1.0$ ) is dominated by the type (e.g., sand, clay, coal) and quantity of fouling material in the ballast layer. As the overall quantity of fines increases in a highly fouled ballast layer, the air entry, water retention potential, and residual volumetric water content increases. Inherent to coal dust's effects on the unsaturated characteristics of the fouling materials, coal dust has a significant effect on the unsaturated behavior of highly fouled ballast. Namely, as the quantity of coal dust increases in a highly fouled ballast layer, the air entry, water retention potential, and residual water content also increases (even if the percent fouling in the layer does not change). Therefore, the unsaturated characteristics of a segment of highly fouled ballast, having similar gradation, could be measurably different throughout its length if it is coal fouled and if the coal content varies. Lastly, as the general quantity of fouling material increases in a highly fouled ballast layer, the residual and saturated water content of the fouled ballast increases.

Inherent to the nature of unsaturated soil in general, and to the findings of this research, a ballast layer with high variability in fouling, environmental and geometric conditions will have highly variable ballast moisture conditions. Because the dielectric constant measured by GPR is influenced by both the water content and the fouling conditions, it is easy to understand why monitoring ballast conditions using GPR is challenging. This research helps to explain why in situ ballast conditions can yield identical GPR dielectric measurements, and that ambiguity in GPR results makes quantitative interpretations of ballast conditions impossible without additional information. The uniqueness of the SWCC to each fouling material and fouled ballast and the differences in residual water content and general water holding capacity as a function of fouling are characteristics of key interest looking ahead. Further characterization of fouled ballast in

unsaturated conditions is hypothesized to decouple water content and fouling parameters for improved interpretation of GPR measurements for in situ identification of fouled ballast. There are questions left to be answered to reach the overarching goal of this research work. For example, how sensitive is GPR to variations of fouling and water content, and how different do the fouling and moisture conditions in a fouled ballast need to be in order to differentiate between conditions using GPR? These results do show promise for the potential of uncoupling the influence of each parameter (fouling conditions and water content). Combined with future research efforts, these results are hypothesized to improve in situ identification of fouled ballast.

All SWCCs presented in this thesis were made on specimens prepared to similar dry density and using a drying method. The dry density of fouled ballast will likely vary over the length of a track segment; the same goes for the wetted condition (i.e., drying or wetting). The materials tested are not a comprehensive evaluation of fouling material composition or fouling degree. The effect of specimen density on the SWCC is currently under investigation. Further research is recommended using a larger array of fouling materials and fouling conditions testing specimens with varied amounts of coal dust and including lower values of percent fouling (where VCI is less than 1.0). These two variables are of higher priority due to the effects of coal dust on fouled ballast and to meet the goal of detecting fouled ballast conditions before they become severely degraded. The next scheduled phase of this research will include instrumentation of the large TRIM cell in order to measure dielectric constant in fouled ballast as moisture changes. That research is hypothesized to enable the uncoupling of moisture content and fouling conditions improving GPR identification of ballast conditions. A desirable outcome of this future work would be an index correlating ranges of dielectric values to ranges of moisture conditions, each for ballast of different fouling conditions.

## Chapter 7 - References

- Aitchison, G. D. (1965). Moisture equilibria and moisture changes in soils beneath covered areas.
- Alsherif, N., Wayllace, A., & Lu, N. (2015). Measuring the Soil Water–Retention Curve Under Positive and Negative Matric Suction Regimes. *Geotechnical Testing Journal*, 38, 442–451.
- Anbazhagan, P., Dixit, P. N., & Bharatha, T. P. (2016). Identification of type and degree of railway ballast fouling using ground coupled GPR antennas. *Journal of Applied Geophysics*, 126, 183–190.
- AREMA. (2019, April). Chapter 1 Railway and Ballast. In *AREMA Manual for Railway Engineering*. American Railway Engineering and Maintenance-of-Way Association (AREMA).
- Armstrong, J. H. (1990). *The Railroad: What it is, What it Does. The Introduction to Railroading*.
- Association of American Railroads. (2019, July). *The Economic Impact of America's Freight Railroads*. Retrieved March 2020, from [www.aar.org](https://www.aar.org/wp-content/uploads/2018/05/AAR-Economic-Impact-US-Freight-Railroads.pdf): <https://www.aar.org/wp-content/uploads/2018/05/AAR-Economic-Impact-US-Freight-Railroads.pdf>
- ASTM C136 / C136M-19, *Standard Test Method for Sieve Analysis of Fine and Coarse Aggregates*, ASTM International, West Conshohocken, PA, 2019, [www.astm.org](http://www.astm.org)
- ASTM C29 / C29M-17a, *Standard Test Method for Bulk Density ("Unit Weight") and Voids in Aggregate*, ASTM International, West Conshohocken, PA, 2017, [www.astm.org](http://www.astm.org)
- ASTM C127-15, *Standard Test Method for Relative Density (Specific Gravity) and Absorption of Coarse Aggregate*, ASTM International, West Conshohocken, PA, 2015, [www.astm.org](http://www.astm.org)
- ASTM D854-14, *Standard Test Methods for Specific Gravity of Soil Solids by Water Pycnometer*, ASTM International, West Conshohocken, PA, 2014, [www.astm.org](http://www.astm.org)
- ASTM D1140-17, *Standard Test Methods for Determining the Amount of Material Finer than 75- $\mu$ m (No. 200) Sieve in Soils by Washing*, ASTM International, West Conshohocken, PA, 2017, [www.astm.org](http://www.astm.org)
- ASTM D2216-19, *Standard Test Methods for Laboratory Determination of Water (Moisture) Content of Soil and Rock by Mass*, ASTM International, West Conshohocken, PA, 2019, [www.astm.org](http://www.astm.org)

- ASTM D2487-17e1, *Standard Practice for Classification of Soils for Engineering Purposes (Unified Soil Classification System)*, ASTM International, West Conshohocken, PA, 2017, [www.astm.org](http://www.astm.org)
- ASTM D4254-16, *Standard Test Methods for Minimum Index Density and Unit Weight of Soils and Calculation of Relative Density*, ASTM International, West Conshohocken, PA, 2016, [www.astm.org](http://www.astm.org)
- ASTM D4253-16e1, *Standard Test Methods for Maximum Index Density and Unit Weight of Soils Using a Vibratory Table*, ASTM International, West Conshohocken, PA, 2016, [www.astm.org](http://www.astm.org)
- ASTM D4318-17e1, *Standard Test Methods for Liquid Limit, Plastic Limit, and Plasticity Index of Soils*, ASTM International, West Conshohocken, PA, 2017, [www.astm.org](http://www.astm.org)
- ASTM D5084-16a, *Standard Test Methods for Measurement of Hydraulic Conductivity of Saturated Porous Materials Using a Flexible Wall Permeameter*, ASTM International, West Conshohocken, PA, 2016, [www.astm.org](http://www.astm.org)
- ASTM D5856-15, *Standard Test Method for Measurement of Hydraulic Conductivity of Porous Material Using a Rigid-Wall, Compaction-Mold Permeameter*, ASTM International, West Conshohocken, PA, 2015, [www.astm.org](http://www.astm.org)
- ASTM D6836-16, *Standard Test Methods for Determination of the Soil Water Characteristic Curve for Desorption Using Hanging Column, Pressure Extractor, Chilled Mirror Hygrometer, or Centrifuge*, ASTM International, West Conshohocken, PA, 2016, [www.astm.org](http://www.astm.org)
- ASTM D6913 / D6913M-17, *Standard Test Methods for Particle-Size Distribution (Gradation) of Soils Using Sieve Analysis*, ASTM International, West Conshohocken, PA, 2017, [www.astm.org](http://www.astm.org)
- ASTM D7928-17, *Standard Test Method for Particle-Size Distribution (Gradation) of Fine-Grained Soils Using the Sedimentation (Hydrometer) Analysis*, ASTM International, West Conshohocken, PA, 2017, [www.astm.org](http://www.astm.org)
- Azam, A. M., Cameron, D. A., Gabr, A. G., & Rahman, M. M. (2014). Matric suction in recycled unbound granular materials. *Geo-Congress 2014: Geo-characterization and Modeling for Sustainability*, (pp. 1367–1376).
- Ba, M., Nokkaew, K., Fall, M., & Tinjum, J. M. (2013). Effect of matric suction on resilient modulus of compacted aggregate base courses. *Geotechnical and Geological Engineering*, 31, 1497–1510.
- Bareither, C. A., & Benson, C. H. (2013). Evaluation of Bouwer-Rice large-particle correction procedure for soil water characteristic curves. *Geotechnical Testing Journal*, 36, 680–694.

- Benson, C. H., Chiang, I., Chalermmyanont, T., & Sawangsuriya, A. (2014). Estimating van Genuchten parameters  $\alpha$  and  $n$  for clean sands from particle size distribution data. In *From Soil Behavior Fundamentals to Innovations in Geotechnical Engineering: Honoring Roy E. Olson* (pp. 410–427).
- Bouwer, H., & Rice, R. C. (1984). Hydraulic Properties of Stony Vadose Zones a. *Groundwater*, 22, 696–705.
- Brooks, R. H., & Corey, A. T. (1966). Properties of porous media affecting fluid flow. *Journal of the irrigation and drainage division*, 92, 61–90.
- Bruzek, R., Stark, T. D., Wilk, S. T., Thompson, H. B., & Sussmann, T. R. (2016). Fouled Ballast Definitions and Parameters. *2016 Joint Rail Conference*.
- Budiono, D. S., McSweeney, T., Dhanasekar, M., & Gurung, N. (2004). The effect of coal dust fouling on the cyclic behaviour of railtrack ballast. *Cyclic behaviour of soils and liquefaction phenomena*, (pp. 627–632).
- Chen, J., Hopmans, J. W., & Grismer, M. E. (1999). Parameter estimation of two-fluid capillary pressure–saturation and permeability functions. *Advances in Water Resources*, 22, 479–493.
- Chrismer, S. M. (2008). Twenty-Five Years of Track Geotechnology Research. *IEEE/ASME/ASCE 2008 Joint Rail Conference*, (pp. 57–60).
- Clark, M. R., Gillespie, R., Kemp, T., McCann, D. M., & Forde, M. C. (2001). Electromagnetic properties of railway ballast. *NDT & E International*, 34, 305–311.
- De Chiara, F., Fontul, S., & Fortunato, E. (2014). GPR laboratory tests for railways materials dielectric properties assessment. *Remote Sensing*, 6, 9712–9728.
- Delage, P., Romero, E., & Tarantino, A. (2008). Recent developments in the techniques of controlling and measuring suction in unsaturated soils. In *Unsaturated Soils. Advances in Geo-Engineering* (pp. 49–68). CRC Press.
- Dombrow, W., Huang, H., & Tutumluer, E. (2009). Comparison of coal dust fouled railroad ballast behavior-granite vs. limestone. *8th International Conference on the Bearing Capacity of Roads, Railways and Airfields, BCR2A'09*, (pp. 1349–1357).
- Eching, S. O., & Hopmans, J. W. (1993). Optimization of hydraulic functions from transient outflow and soil water pressure data. *Soil Science Society of America Journal*, 57, 1167–1175.
- Edlefsen, N., Anderson, A., & others. (1943). Thermodynamics of soil moisture. *Hilgardia*, 15, 31–298.



- Feldman, F., Nissen, D., & others. (2002). Alternative testing method for the measurement of ballast fouling: percentage void contamination. *CORE 2002: Cost efficient railways through engineering*, 101.
- Fityus, S. G., & Li, J. (2006). Water retention characteristics of unsaturated coal. In *Unsaturated Soils 2006* (pp. 1415–1426).
- Fortunato, E., Pinelo, A., & Fernandes, M. M. (2010). Characterization of the fouled ballast layer in the substructure of a 19th century railway track under renewal. *Soils and foundations*, 50, 55–62.
- Fredlund, D. G. (2017). Role of the soil-water characteristic curve in unsaturated soil mechanics. *Proceedings of the 19th International Conference on Soil Mechanics and Geotechnical Engineering*, (pp. 17–22).
- Fredlund, D. G., & Houston, S. L. (2009). Protocol for the assessment of unsaturated soil properties in geotechnical engineering practice. *Canadian Geotechnical Journal*, 46, 694–707.
- Fredlund, D. G., & Rahardjo, H. (1993). *Soil mechanics for unsaturated soils*. John Wiley & Sons.
- Fredlund, D. G., & Xing, A. (1994). Equations for the soil-water characteristic curve. *Canadian geotechnical journal*, 31, 521–532.
- García-Gaines, R. A., & Frankenstein, S. (2015). USCS and the USDA soil classification system: Development of a mapping scheme.
- Garven, E. A., & Vanapalli, S. K. (2006). Evaluation of empirical procedures for predicting the shear strength of unsaturated soils. In *Unsaturated Soils 2006* (pp. 2570–2592).
- Gupta, S., Kang, D. H., & Ranaivoson, A. (2009). Hydraulic and mechanical properties of recycled materials.
- Gupta, S., Ranaivoson, A., Edil, T., Benson, C., & Sawangsuriya, A. (2007). Pavement design using unsaturated soil technology.
- Harris, T. (2016). BALLAST CLEANING TO IMPROVE DRAINAGE IN METROLINK'S VALLEY SUBDIVISION TUNNEL 25. *ARMEMA 2016 Annual Congerence & Exposition* (pp. 1386-1398). Orlando, Florida: AREMA.
- Hay, W. W. (1982). *Railroad engineering* (Vol. 1). John Wiley & Sons.
- Hollenbeck, K.-J., & Jensen, K. H. (1998). Experimental evidence of randomness and nonuniqueness in unsaturated outflow experiments designed for hydraulic parameter estimation. *Water Resources Research*, 34, 595–602.

- Hopmans, J. W., Šimůnek, J., Romano, N., & Durner, W. (2002). 3.6. 2. Inverse Methods. *Methods of Soil Analysis: Part 4 Physical Methods*, 5, 963–1008.
- Hu, W., Dano, C., Hicher, P.-Y., Le Touzo, J.-Y., Derks, F., & Merliot, E. (2011). Effect of sample size on the behavior of granular materials. *Geotechnical Testing Journal*, 34, 186–197.
- Indraratna, B., Khabbaz, H., Salim, W., & Christie, D. (2006). Geotechnical properties of ballast and the role of geosynthetics in rail track stabilisation. *Proceedings of the Institution of Civil Engineers-Ground Improvement*, 10, 91–101.
- Indraratna, B., Ngo, N. T., & Rujikiatkamjorn, C. (2011b). Behavior of geogrid-reinforced ballast under various levels of fouling. *Geotextiles and geomembranes*, 29, 313–322.
- Indraratna, B., Ngo, N. T., & Rujikiatkamjorn, C. (2013). Deformation of coal fouled ballast stabilized with geogrid under cyclic load. *Journal of Geotechnical and Geoenvironmental Engineering*, 139, 1275–1289.
- Indraratna, B., Ngo, N. T., Rujikiatkamjorn, C., & Vinod, J. S. (2014). Behavior of fresh and fouled railway ballast subjected to direct shear testing: discrete element simulation. *International Journal of Geomechanics*, 14, 34–44.
- Indraratna, B., Nimbalkar, S. S., & Tennakoon, N. (2010). The behaviour of ballasted track foundations: track drainage and geosynthetic reinforcement. In *GeoFlorida 2010: Advances in analysis, modeling & design* (pp. 2378–2387).
- Indraratna, B., Su, L.-j., & Rujikiatkamjorn, C. (2011a). A new parameter for classification and evaluation of railway ballast fouling. *Canadian Geotechnical Journal*, 48, 322–326.
- Indraratna, B., Sun, Y., & Nimbalkar, S. (2016). Laboratory assessment of the role of particle size distribution on the deformation and degradation of ballast under cyclic loading. *Journal of Geotechnical and Geoenvironmental Engineering*, 142, 04016016.
- Ishikawa, T., Fuku, S., Nakamura, T., Momoya, Y., & Tokoro, T. (2016). Influence of Water Content on Shear Behavior of Unsaturated Fouled Ballast. *Procedia engineering*, 143, 268–275.
- Kashani, H. F., Ho, C. L., & Hyslip, J. P. (2018). Fouling and water content influence on the ballast deformation properties. *Construction and Building Materials*, 190, 881–895.
- Kashani, H. F., Ho, C. L., Oden, C. P., & Smith, S. S. (2015). Model track studies by ground penetrating radar (GPR) on ballast with different fouling and geotechnical properties. *2015 Joint Rail Conference*.
- Khaleel, R., & Freeman, E. J. (1995). *Variability and scaling of hydraulic properties for 200 area soils, Hanford Site*. Tech. rep., Westinghouse Hanford Co.

- Konietzky, H., te Kamp, L., Groeger, T., & Jenner, C. (2004). Use of DEM to model the interlocking effect of geogrids under static and cyclic loading. *Numerical modeling in micromechanics via particle methods*, 3–12.
- Kool, J. B., Parker, J. C., & Van Genuchten, M. T. (1985). Determining soil hydraulic properties from one-step outflow experiments by parameter estimation: I. Theory and numerical studies. *Soil Science Society of America Journal*, 49, 1348–1354.
- Kulesza, S., Sherwood, R., & Berry, M. (2020, January 28). Estimation of Soil-Water Characteristic Curves in Fouled Ballast. Retrieved from Geosynthetica: <https://www.geosynthetica.com/fouled-ballast-soil-water-curves/>
- Leong, E. C., & Rahardjo, H. (1997). Review of soil-water characteristic curve equations. *Journal of geotechnical and geoenvironmental engineering*, 123, 1106–1117.
- Likos, W. J., & Lu, N. (2004). Hysteresis of capillary stress in unsaturated granular soil. *Journal of Engineering mechanics*, 130, 646–655.
- Liu, Z., Li, W., Zhang, Y., Wang, J., Orndorff, W., & Pan, W.-P. (2015). Influence of biomass on coal combustion based on thermogravimetry and Fourier transform infrared spectroscopy. *Journal of Thermal Analysis and Calorimetry*, 122, 1289–1298.
- McDowell, G., & Stickley, P. (2006). Performance of geogrid-reinforced ballast. *Ground Engineering*, 39, 26–30.
- Meeker, L. E. (1990). *Engineering and economic factors affecting the cost of railroad ballast*. Ph.D. dissertation, University of Nevada, Reno.
- Ngo, N. T., Indraratna, B., & Rujikiatkamjorn, C. (2017). Micromechanics-based investigation of fouled ballast using large-scale triaxial tests and discrete element modeling. *Journal of Geotechnical and Geoenvironmental Engineering*, 143, 04016089.
- Nokkaew, K., Tinjum, J. M., & Benson, C. H. (2012). Hydraulic properties of recycled asphalt pavement and recycled concrete aggregate. In *GeoCongress 2012: State of the Art and Practice in Geotechnical Engineering* (pp. 1476–1485).
- Rahardjo, H., Kim, Y., & Satyanaga, A. (2019). Role of unsaturated soil mechanics in geotechnical engineering. *International Journal of Geo-Engineering*, 10, 8.
- Rahman, A. J. (2013). *Permeability, resistivity and strength of fouled railroad ballast*. Ph.D. dissertation, University of Kansas.
- Raymond, G. P. (1985). Research on railroad ballast specification and evaluation. *Transportation Research Record*, 1006, 1–8.
- Richards, L. A. (1931, 11). Capillary Conduction of Liquids Through Porous Mediums. *Physics*, 1, 318–333. doi:10.1063/1.1745010

- Rujikiatkamjorn, C., Indraratna, B., Ngo, N. T., & Coop, M. (2012). A laboratory study of railway ballast behaviour under various fouling degree.
- Russo, D. (1988). Determining soil hydraulic properties by parameter estimation: On the selection of a model for the hydraulic properties. *Water resources research*, 24, 453–459.
- Russo, D., Bresler, E., Shani, U., & Parker, J. C. (1991). Analyses of infiltration events in relation to determining soil hydraulic properties by inverse problem methodology. *Water Resources Research*, 27, 1361–1373.
- Sadeghi, J., Motieyan-Najar, M. E., Zakeri, J. A., Yousefi, B., & Mollazadeh, M. (2018). Improvement of railway ballast maintenance approach, incorporating ballast geometry and fouling conditions. *Journal of Applied Geophysics*, 151, 263–273.
- Sahin, H. (2014). *Nondestructive test methods for rapid assessment of flexible base performance in transportation infrastructures*. Ph.D. dissertation.
- Sahu, S. G., Sarkar, P., Chakraborty, N., & Adak, A. K. (2010). Thermogravimetric assessment of combustion characteristics of blends of a coal with different biomass chars. *Fuel Processing Technology*, 91, 369–378.
- Sapko, M. J., Cashdollar, K. L., & Green, G. M. (2007). Coal dust particle size survey of US mines. *Journal of Loss Prevention in the Process Industries*, 20, 616–620.
- Sawangsurriya, A. (2006). *Stiffness-suction-moisture relationship for compacted soils*. The University of Wisconsin-Madison.
- Selig, E. T., & Waters, J. M. (1994). *Track geotechnology and substructure management*. Thomas Telford.
- Selig, E. T., DelloRusso, V., & Laine, K. J. (1992). Sources and causes of ballast fouling. *Association of American Railroad (AAR), Report No.*
- Sharma, P. P., Carter, F. S., & Halvorson, G. A. (1993). Water retention by soils containing coal. *Soil Science Society of America Journal*, 57, 311–316.
- Sherwood, R. R., Kulesza, S. E., & Bernhardt-Barry, M. L. (2020). Unsaturated Characteristics of Fouled Ballast to Support In Situ Identification of Fouling. *Geo-Congress 2020: Geo-Systems, Sustainability, Geoenvironmental Engineering, and Unsaturated Soil Mechanics*, (pp. 320–329).
- Simunek, J., Sejna, M., Van Genuchten, M. T., Šimunek, J., Šejna, M., Jacques, D., . . . Sakai, M. (1998). HYDRUS-1D. *Simulating the one-dimensional movement of water, heat, and multiple solutes in variably-saturated media, version, 2*.
- Soilmoisture Equipment Corp. (2020, June 3). *Porous Ceramics*. Retrieved from soilmoisture.com: <https://www.soilmoisture.com/1/4-inch-Thick-Ceramic-Plates-0604-SERIES/>

- SoilWater Retention LLC. (2018, October). Transient Release and Imbibitions Method (TRIM). *User's Manual*. SoilWater Retention LLC.
- Sussmann Jr, T. R. (1999). *Application of ground-penetrating radar to railway track substructure maintenance management*.
- Sussmann, T. R., Ruel, M., & Chrismer, S. M. (2012). Source of ballast fouling and influence considerations for condition assessment criteria. *Transportation Research Record*, 2289, 87–94.
- Sussmann, T. R., Selig, E. T., & Hyslip, J. P. (2003). Railway track condition indicators from ground penetrating radar. *NDT & e International*, 36, 157–167.
- Tennakoon, N., Indraratna, B., Rujikiatkamjorn, C., Nimbalkar, S., & Neville, T. (2012). The role of ballast-fouling characteristics on the drainage capacity of rail substructure. *Geotechnical Testing Journal*, 35, 629–640.
- Tuller, M., Or, D., & Hillel, D. (2004). Retention of water in soil and the soil water characteristic curve. *Encyclopedia of Soils in the Environment*, 4, 278–289.
- Tutumluer, E., Dombrow, W., & Huang, H. (2008). Laboratory characterization of coal dust fouled ballast behavior. *AREMA 2008 Annual Conference & Exposition*, (pp. 21–24).
- Tutumluer, E., Moaveni, M., Read, D., Li, D., Lees, H., & Clark, D. (2011). Investigation of coal dust composition affecting railroad ballast behavior. *International Heavy Haul (IHHA) specialist technical sessions 2011: railroading in extreme conditions, 2011, Calgary, Alberta, Canada*.
- U.S. Department of the Interior, U.S. Geological Survey. (2017, December 18). *USGS Groundwater Information*. Retrieved from USGS science for a changing world: <https://water.usgs.gov/ogw/unsaturated.html>
- Van Genuchten, M. T. (1980). A closed-form equation for predicting the hydraulic conductivity of unsaturated soils 1. *Soil science society of America journal*, 44, 892–898.
- Van Genuchten, M. T., Leij, F. J., Yates, S. R., & others. (1991). The RETC code for quantifying the hydraulic functions of unsaturated soils.
- Vanapalli, S. K., Sillers, W. S., & Fredlund, M. D. (1998). The meaning and relevance of residual state to unsaturated soils. *51st Canadian Geotechnical Conference*, (pp. 4–7).
- Walker, P. J. (1997). Measurement of total suction and matric suction in pavement materials at Dandenong ALF site. *Road and transport research*, 6.
- Wallace, A. J. (2003). Permeability of fouled rail ballast. *UG Thesis, School of Civil, Mining and Environmental Engineering, University of Wollongong, New South Wales, Australia*.

- Wayllace, A., & Lu, N. (2012). A transient water release and imbibitions method for rapidly measuring wetting and drying soil water retention and hydraulic conductivity functions. *Geotechnical Testing Journal*, 35, 103–117.
- Yang, H., Rahardjo, H., Leong, E.-C., & Fredlund, D. G. (2004). Factors affecting drying and wetting soil-water characteristic curves of sandy soils. *Canadian Geotechnical Journal*, 41, 908–920.
- Zachmann, D. W., Du Chateau, P. C., & Klute, A. (1982). Simultaneous approximation of water capacity and soil hydraulic conductivity by parameter identification1. *Soil Science*, 134, 157–163.
- Zachmann, D. W., Duchateau, P. C., & Klute, A. (1981). The Calibration of the Richards Flow Equation for a Draining Column by Parameter Identification 1. *Soil Science Society of America Journal*, 45, 1012–1015.
- Zhang, Q., Gascoyne, J., & Eriksen, A. (2011). Characterisation of ballast materials in trackbed using ground penetrating radar: Part 1.
- Zhang, W., Jiang, S., Hardacre, C., Goodrich, P., Wang, K., Shao, H., & Wu, Z. (2015). A combined Raman spectroscopic and thermogravimetric analysis study on oxidation of coal with different ranks. *Journal of analytical methods in chemistry*, 2015.

# **Appendix A - A Comprehensive Record of Experimental Results**

## ***Contents:***

### **A.1 Ballast Fouling Materials**

Geotechnical Data and GSD Curves

TGA Results

TGA of P40 Portion of Fouling Materials Containing Coal Dust

TGA of P40 and P200 Portion of CL-2 the Fouling Material Containing Coal Dust

Unsaturated Characteristics

### **A.2 Fouled Ballast Predictions**

Geotechnical Data and GSD Curves

Bouwer-Rice Coefficients and Unsaturated Characteristics

### **A.3 Fouled Ballast and the Large TRIM**

Geotechnical Data and GSD Curves

Unsaturated Characteristics

### **A.4 Example Numerical Solution of Richards' Equation**

Introduction

Theory

Discretization Scheme

Model

Solution

## A.1 Ballast Fouling Materials

**Table A.1: Geotechnical Results**

No.	Percent Gravel	Percent Sand	Percent Fines	D <sub>10</sub> (mm)	D <sub>50</sub> (mm)	LL	PI	Cc	Cu	USCS	Gs
1	47.2	51.7	1.10	0.31	4.39	-	-	1.16	18.5	SW	2.66
2	44.8	54.3	0.90	0.30	4.11	-	-	1.88	17.6	SW	2.63
3	41.3	57.7	1.00	0.27	3.36	-	-	1.38	17.9	SW	2.63
4	42.3	56.8	0.90	0.33	3.82	-	-	1.52	15.3	SW	2.60
5	41.3	56.7	2.00	0.20	3.26	-	-	0.697	24.7	SP	2.62
6	25.4	72.3	2.30	0.12	1.31	-	-	0.416	19.5	SP	2.62
7	33.7	65.0	1.30	0.16	2.23	-	-	0.634	24.0	SP	2.63
8	26.8	55.7	17.5	0.03	0.80	20	2	1.07	75.3	SM	2.60
9	9.80	35.3	54.9	0.002	0.046	38	27	2.12	50.1	ML	2.70
10	16.7	43.0	40.3	0.002	0.24	24	6	0.340	380	SC-SM	2.67
11	16.7	44.1	39.2	0.001	0.25	24	6	0.334	524	SC-SM	2.58
12	15.7	38.5	45.8	0.002	0.13	24	6	0.318	170	SC-SM	2.66
13	11.0	33.5	55.5	0.001	0.028	27	7	0.287	199	CL	2.60
14	10.8	30.5	58.7	0.001	0.018	28	8	0.393	160	CL	2.56

**Table A.2: Permeability Methods and Results**

USCS	ASTM	Method	B-value	$K_s$ (cm/s)	$\rho_d$ (g/cm <sup>3</sup> )
SP	D5856	A-Constant Head	-	6.90E-02	1.66
SC-SM	D5084	C-Falling Head	1.00	1.47E-04	1.68
CL	D5084	C-Falling Head	0.99	2.69E-05	1.67



### *GSD Curves for Ballast Fouling Materials*

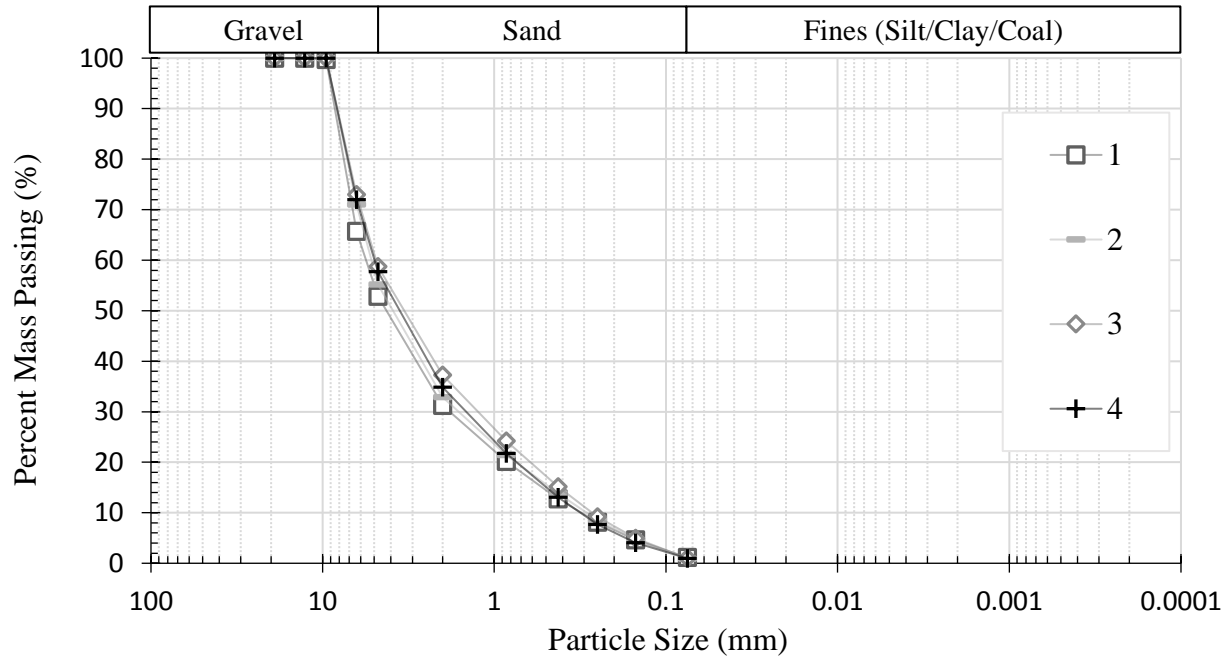


**Figure A.1: GSD of SW Fouling Materials.**

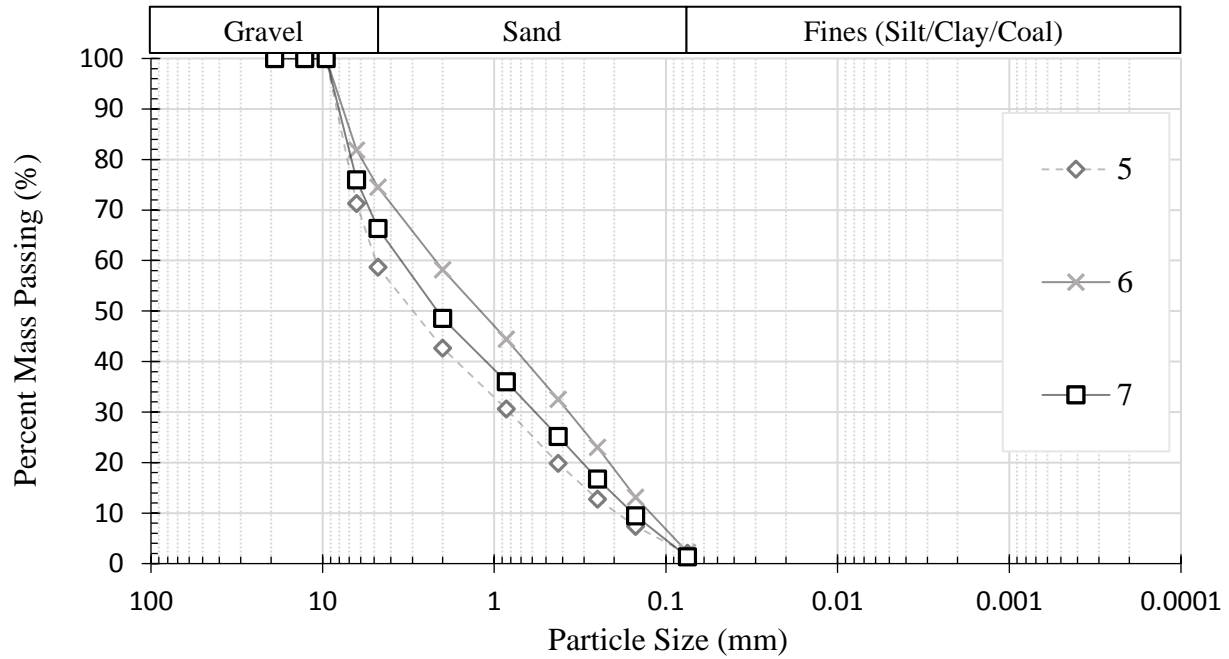


**Figure A.2: GSD of SP Fouling Materials.**

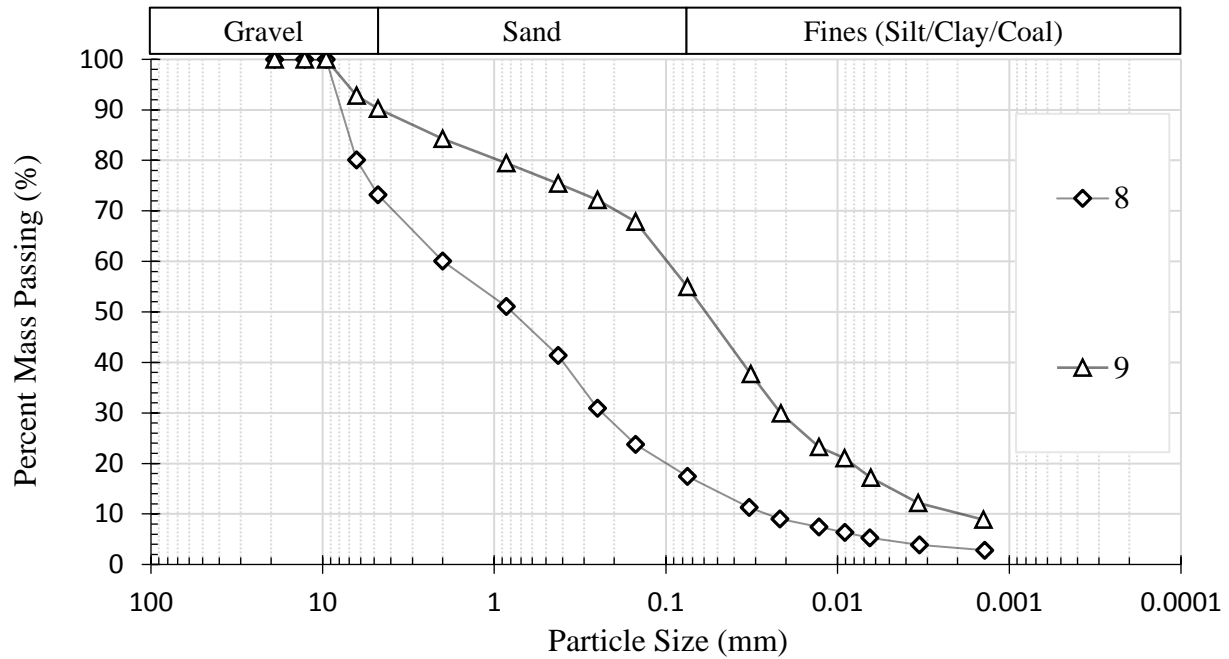


**Figure A.3: GSD of SM (No. 8) and ML (No. 9) Fouling Materials.**

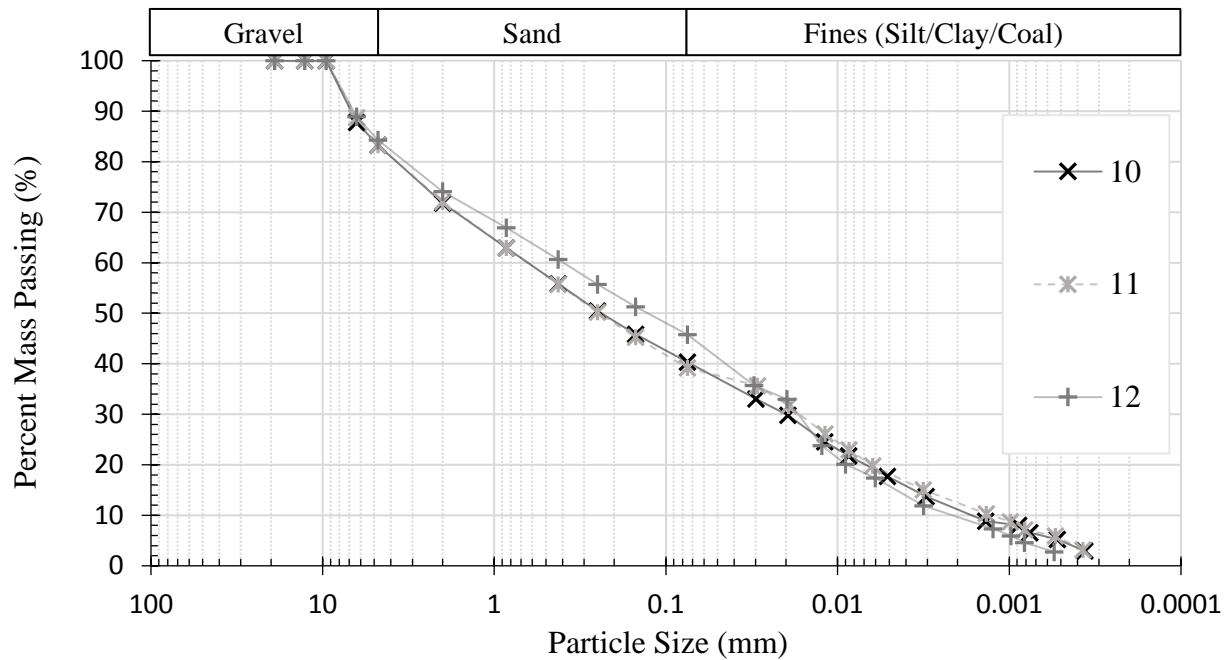


**Figure A.4: GSD of SC-SM Fouling Materials with Coal Dust.**

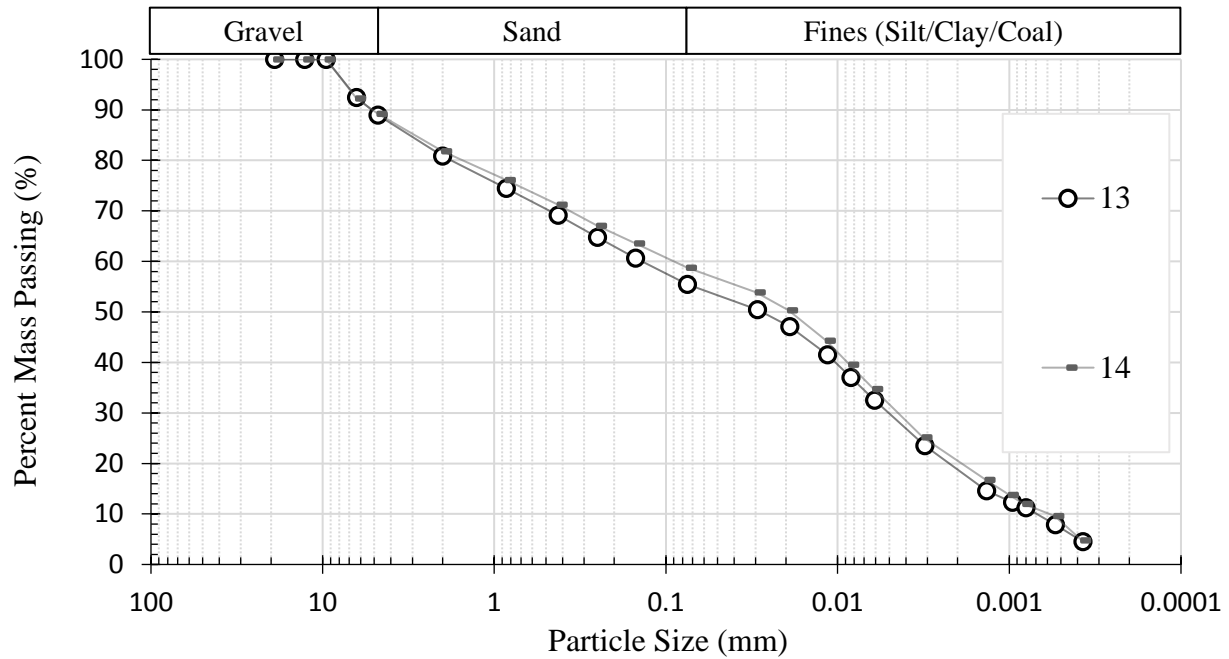


Figure A.5: GSD of CL Fouling Materials with Coal Dust.

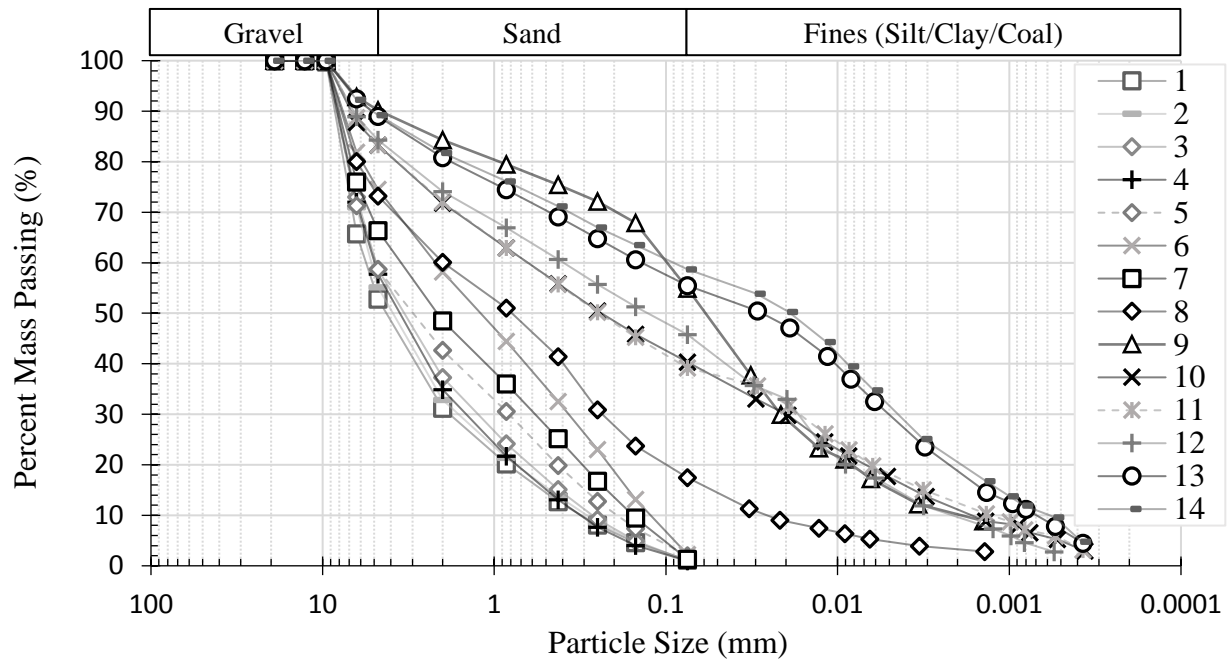


Figure A.6: GSD of all Fouling Materials.

### *TGA Analysis on Fouling Materials Containing Coal Dust*

**Table A.3: Example of TGA System Information**

<b>Mode</b>	TGA 1000 °C
<b>RunSerial</b>	1087
<b>Instrument</b>	TGA Q50 V20.10 Build 36
<b>Module</b>	TGA
<b>InstSerial</b>	0050-1065
<b>FurnaceType</b>	Standard
<b>Sample</b>	SC-SM 1
<b>Size</b>	9.65 mg
<b>ProcName</b>	Ramp
<b>Method</b>	Ramp
<b>Comment</b>	
<b>Xcomment</b>	Pan: Platinum
<b>Xcomment</b>	Gas1: Nitrogen
<b>Xcomment</b>	Gas2: Air
<b>Xcomment</b>	Balance Gas: Nitrogen 20.0 ml/min
<b>Xcomment</b>	Sample Gas: Nitrogen 80.0 ml/min
<b>Text</b>	Ramp to 850°C to test the presence of Coal Dust in Ballast Samples.
<b>Kcell</b>	1
<b>TempCal</b>	1
<b>InstCalDate</b>	Weight Date 2020-02-21 21:40:37
<b>Controls</b>	Gas 1 Event Off Sampling 0.5
<b>Nsig</b>	4
<b>Sig1</b>	Time (min)
<b>Sig2</b>	Temperature (°C)
<b>Sig3</b>	Weight (mg)
<b>Sig4</b>	Deriv. Weight (%/°C)
<b>AirCoolTime</b>	10.0 min
<b>Date</b>	3/3/2020
<b>Time</b>	16:27:59
<b>OrgMethod</b>	1: Ramp 10.00 °C/min to 850.00 °C

**Table A.4: TGA sample sizes**

<b>Sample</b>	<b>SC-SM-1</b>	<b>SC-SM-2</b>	<b>SC-SM-3</b>	<b>CL-1</b>	<b>CL-2</b>
<b>Size (mg)</b>	9.650	9.104	9.321	13.182	10.733

### TGA Results for the P40 Portion of each Ballast Fouling Material Containing Coal Dust

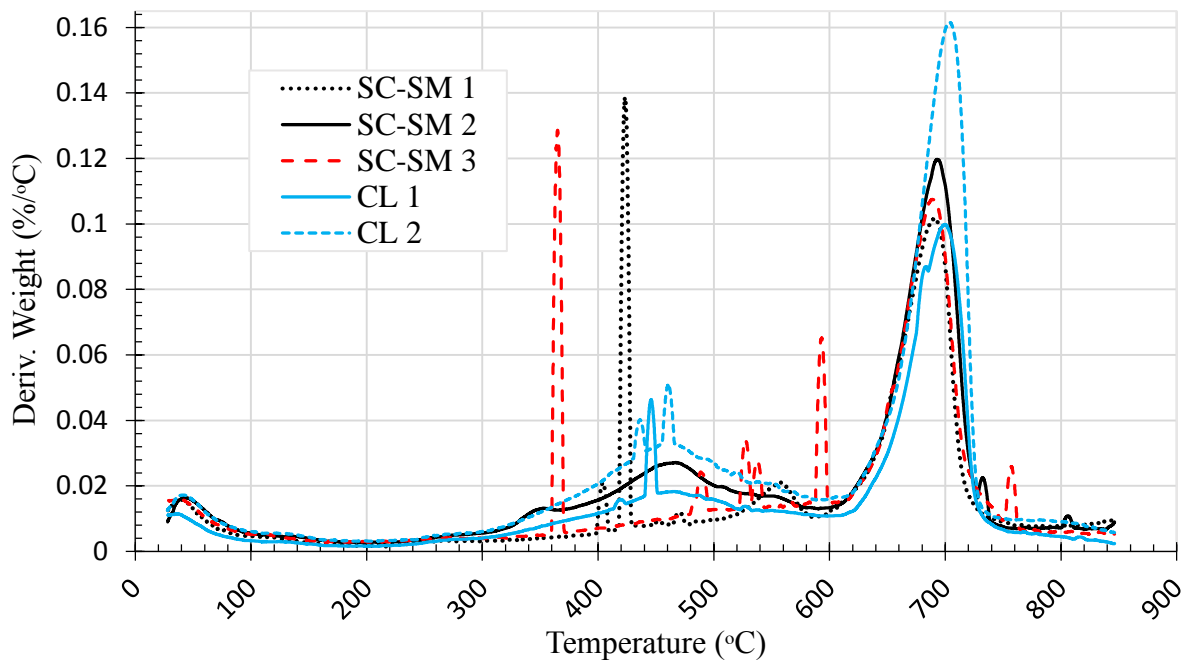


Figure A.7: TGA, Deriv. Weight (%/C) vs. Temp. (C) for the P40 Portion of Fouling Materials Containing Coal Dust.

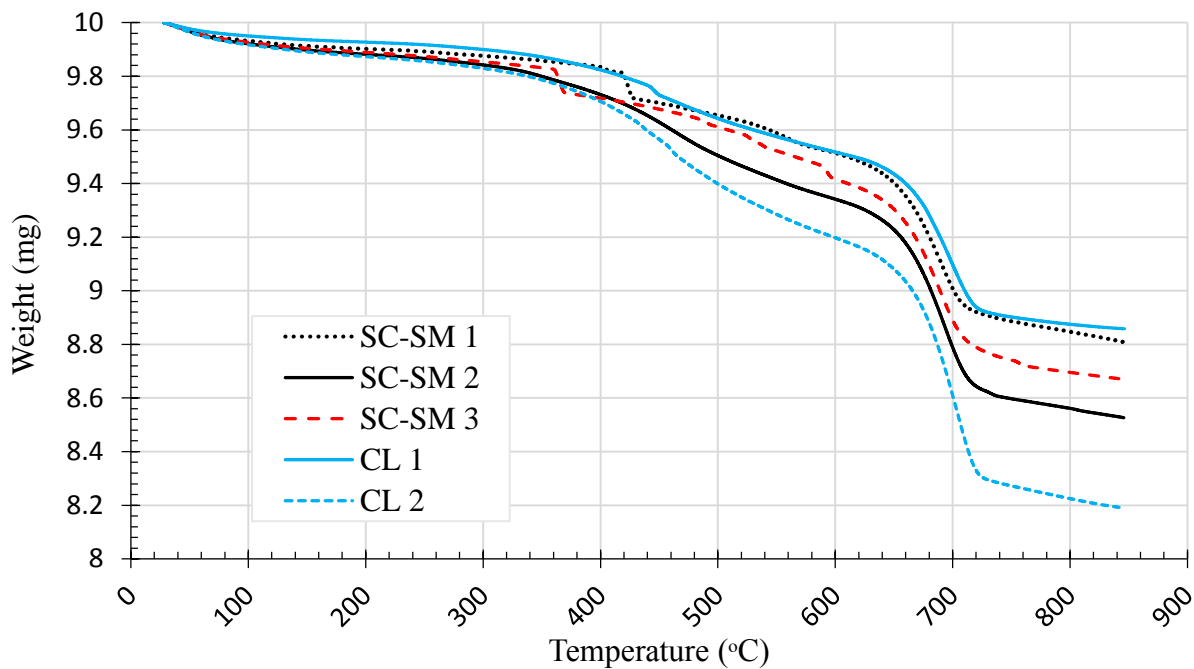
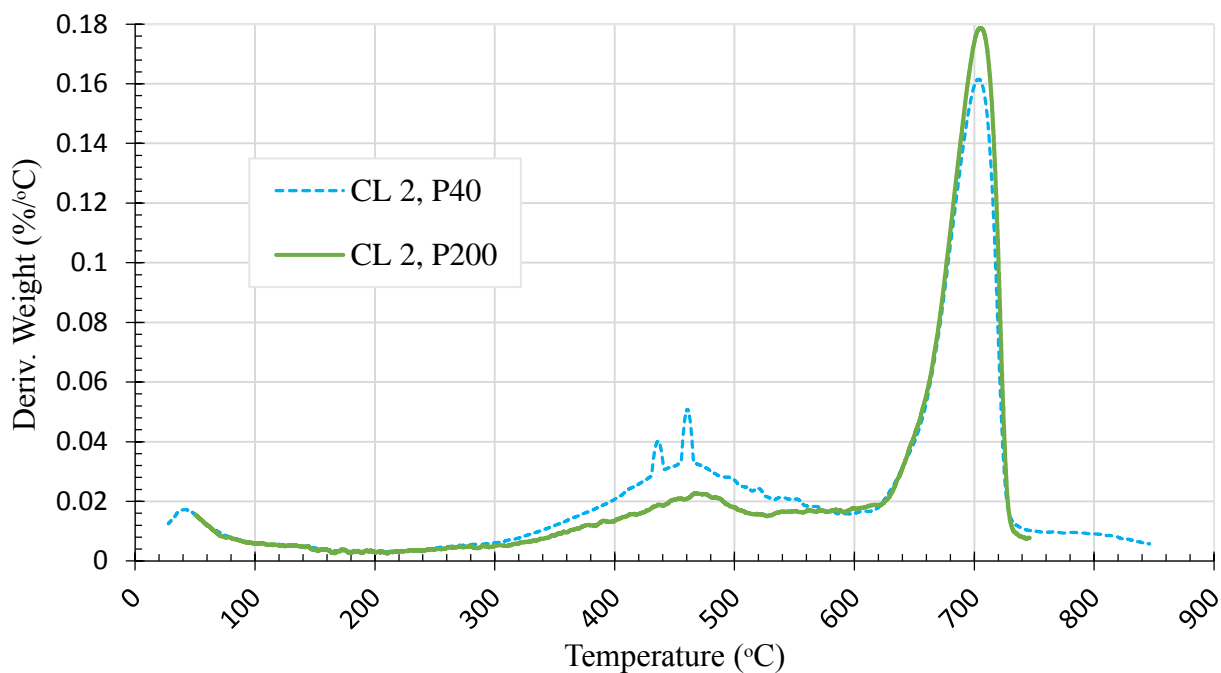
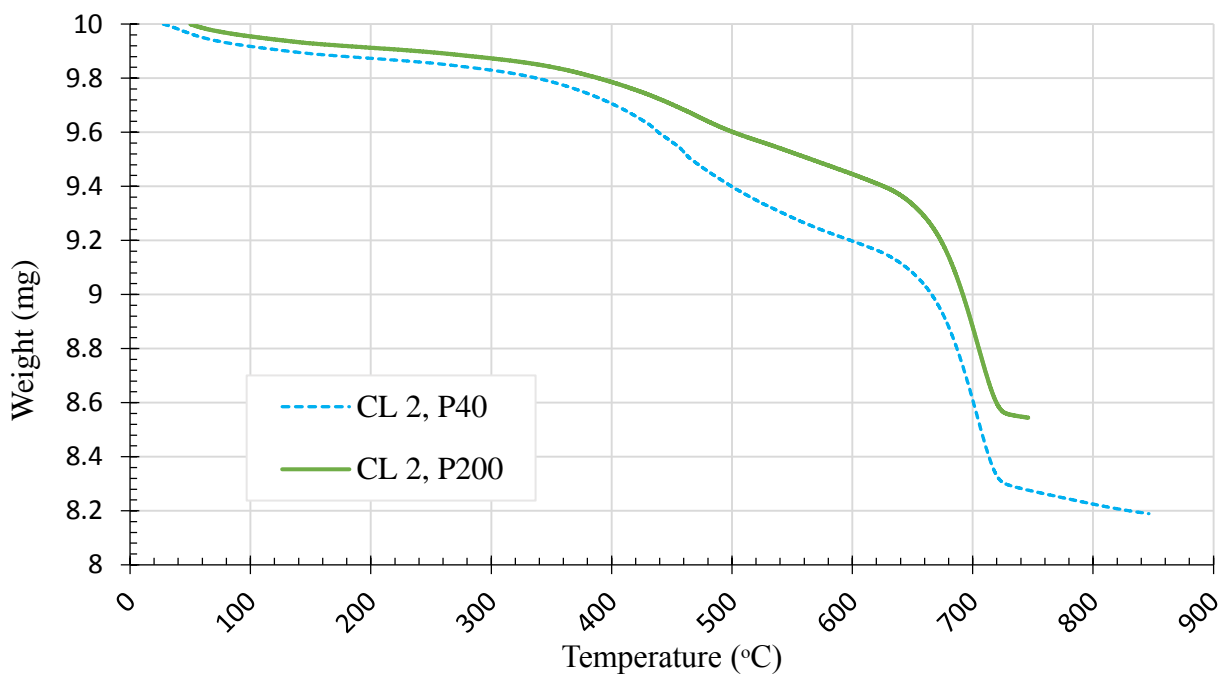


Figure A.8: TGA, Weight (mg) vs. Temp. (C) for the P40 Portion of Fouling Materials Containing Coal Dust.

### TGA Results for the P200 Portion of the CL-2 Ballast Fouling Material with Coal Dust



**Figure A.9:** TGA, Deriv. Weight (%/C) vs. Temp. (C) for the P40 and P200 Portions of the CL-2 Fouling Material.



**Figure A.10:** TGA, Weight (mg) vs. Temp. (C) for the P40 and P200 Portions of the CL-2 Fouling Material.

### *Unsaturated Characteristics of Ballast Fouling Materials*

**Table A.5: van Genuchten Hydraulic Parameters with Model Fit Statistics**

No.	$\theta_r$	$\alpha$ (1/cm)	n	m	$K_s$ (cm/s)	R <sup>2</sup>	SSQ
1	0.056	0.069	3.50	0.714	1.71E-02	0.94	1.21E-02
2	0.059	0.190	3.33	0.700	1.12E-02	1.00	1.66E-03
3	0.063	0.164	5.00	0.800	1.60E-03	1.00	6.81E-02
4	0.063	0.238	1.98	0.496	2.56E-02	1.00	5.34E-03
5	0.063	0.107	4.06	0.754	8.14E-03	1.00	1.46E-03
6	0.082	0.066	6.73	0.851	7.36E-04	1.00	2.91E-03
7	0.062	0.128	2.26	0.557	6.39E-03	1.00	1.13E-03
8	0.067	0.0587	2.61	0.616	5.10E-04	1.00	7.28E-04
9	0.121	0.00492	1.82	0.451	8.70E-05	1.00	6.84E-04
10	0.162	0.0130	3.50	0.714	9.52E-05	1.00	3.85E-03
11	0.169	0.0128	3.50	0.714	2.01E-04	0.99	9.88E-03
12	0.180	0.0217	3.50	0.714	1.18E-04	1.00	4.88E-03
13	0.148	0.0124	3.50	0.714	4.51E-05	0.99	5.77E-03
14	0.155	0.0022	1.61	0.379	3.50E-05	0.98	1.90E-02

**Table A.6: Density and Porosity of TRIM Specimens**

No.	USCS	Density (g/cm <sup>3</sup> )	Porosity (%)
1	SW	1.56	41
2	SW	1.64	38
3	SW	1.76	33
4	SW	1.66	36
5	SP	1.56	41
6	SP	1.65	37
7	SP	1.70	36
8	SM	1.70	36
9	ML	1.68	37
10	SC-SM	1.67	37
11	SC-SM	1.64	36
12	SC-SM	1.68	37
13	CL	1.67	36
14	CL	1.57	39

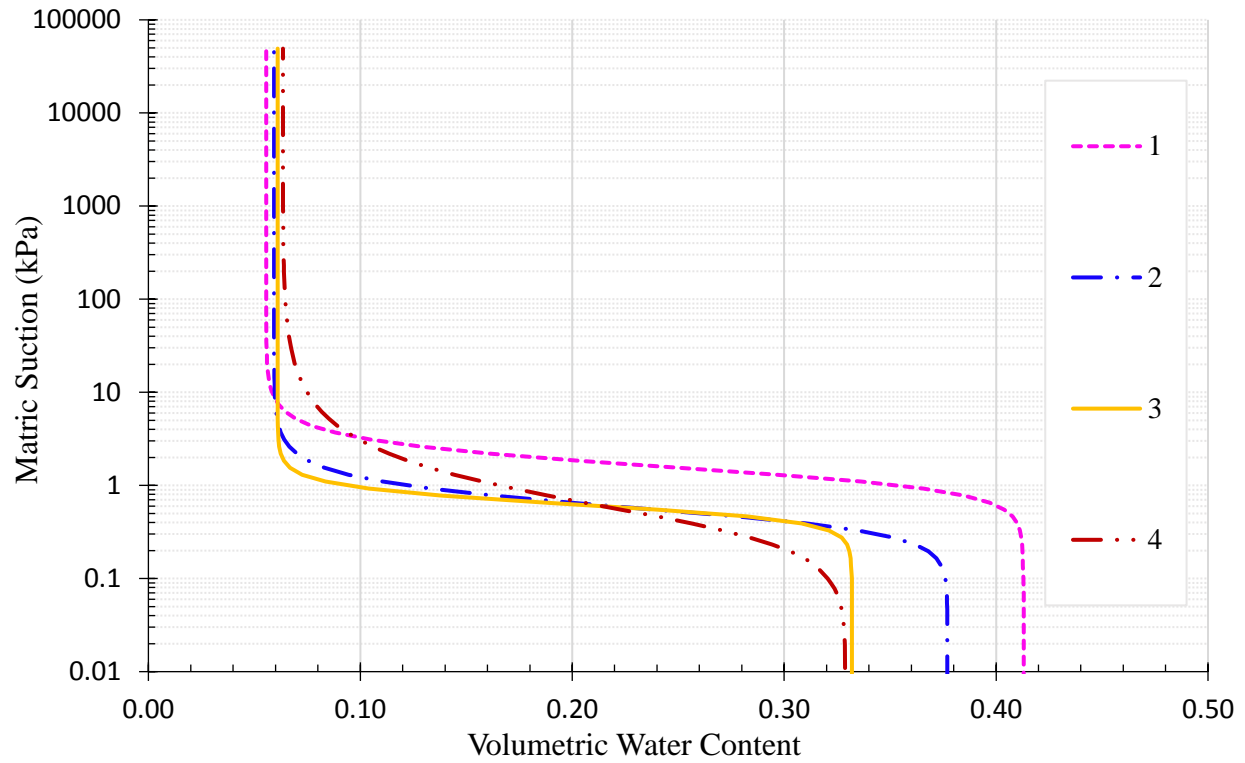


**Figure A.11: SWCCs of SW Fouling Materials.**

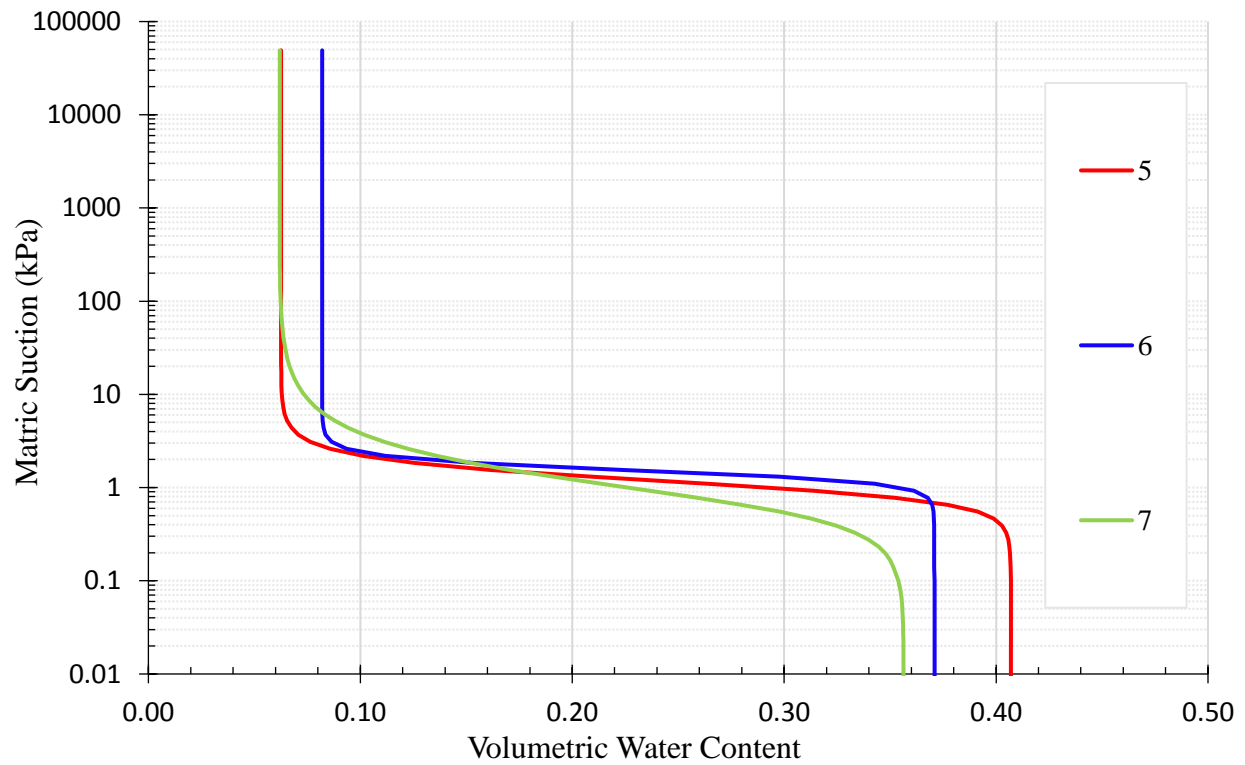


**Figure A.12: SWCCs of SP Fouling Materials..**



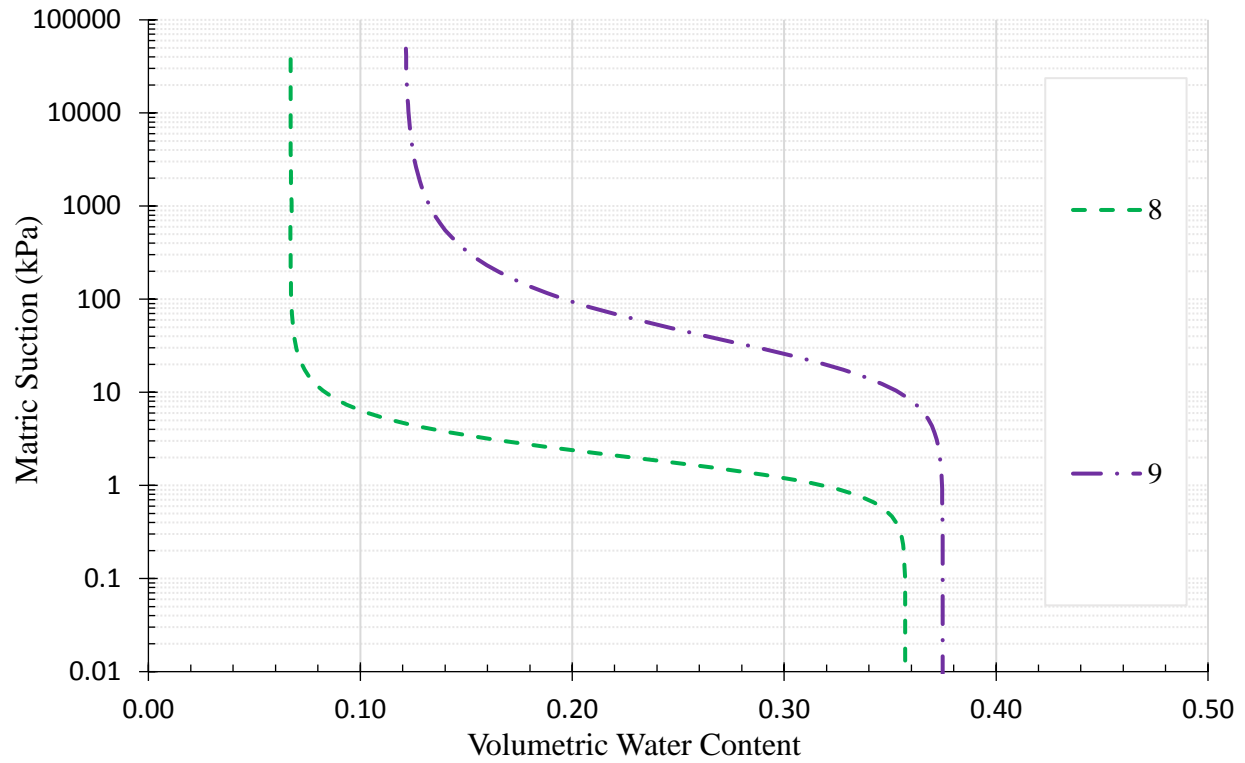


**Figure A.13: SWCCs of SM (8) and ML (9) Fouling Materials.**

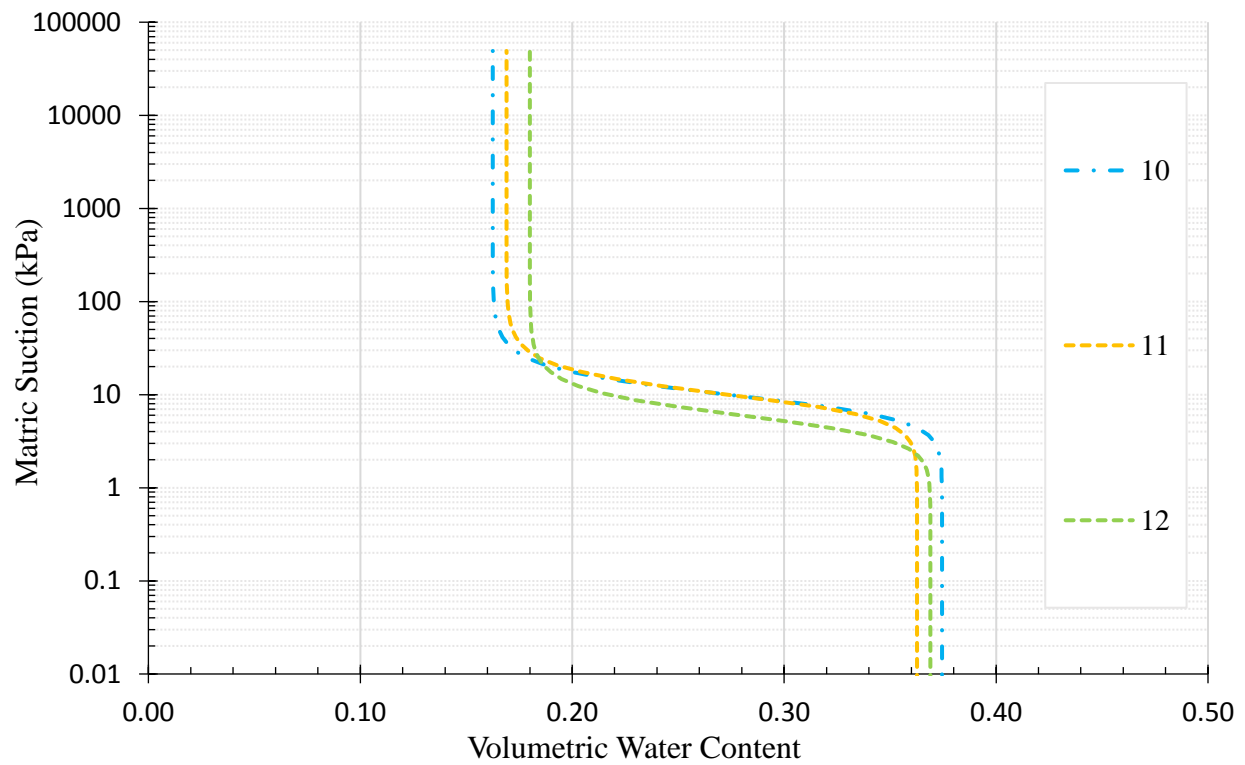


**Figure A.14: SWCCs of SC-SM Fouling Materials with Coal Dust.**

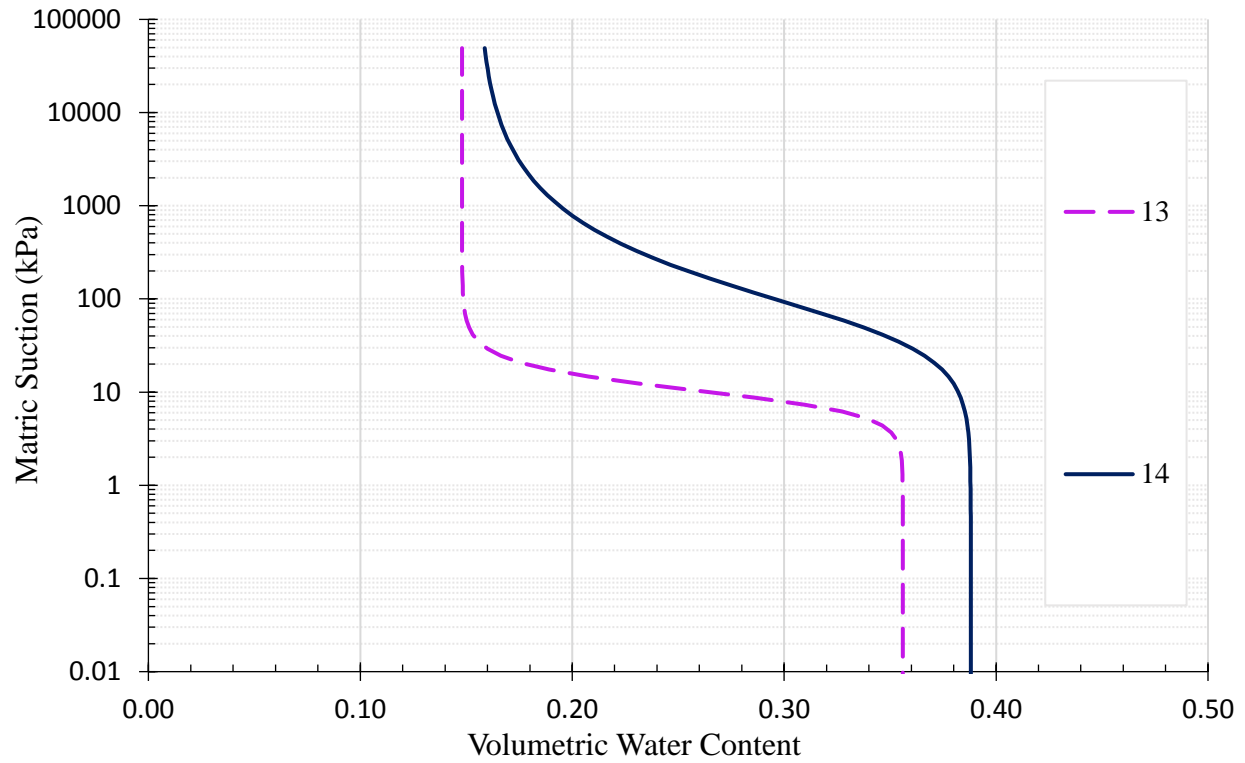


**Figure A.15: SWCCs for CL Fouling Materials with Coal Dust.**

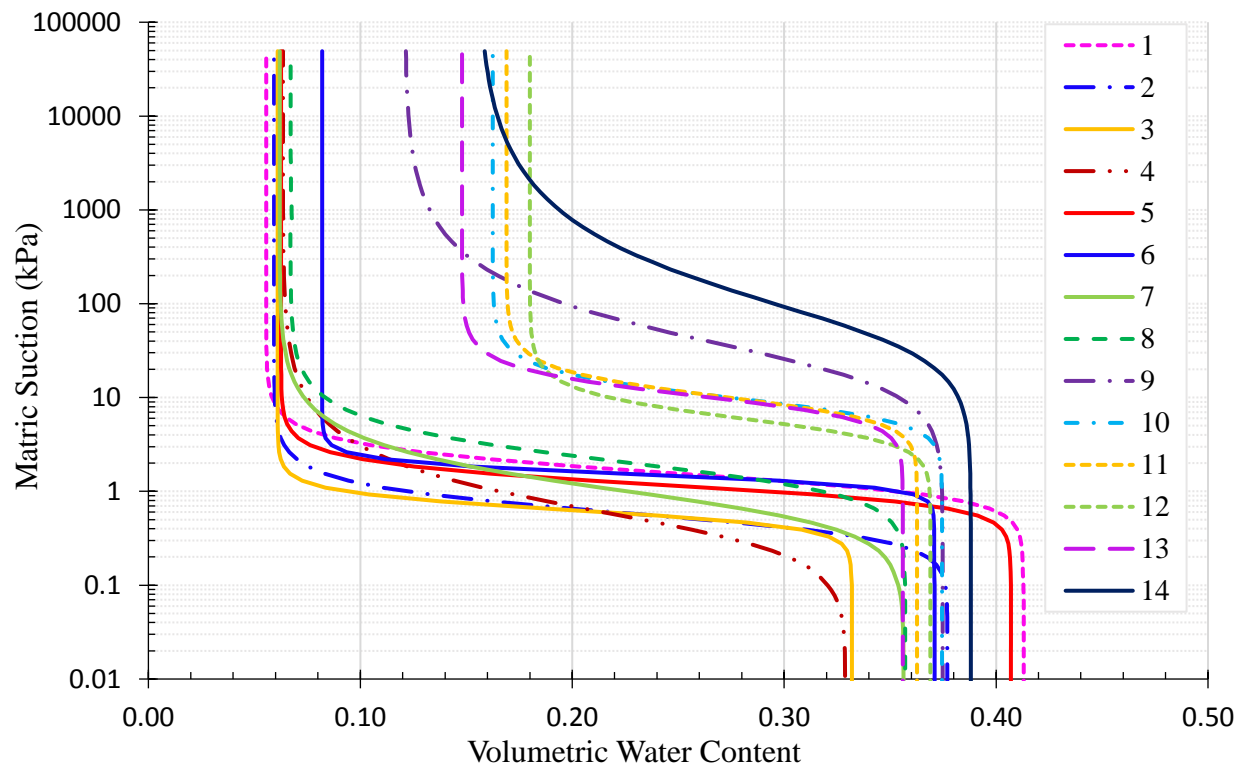


**Figure A.16: SWCCs of Fouling Materials.**

## A.2 Theoretical Fouled Ballast

**Table A.7: Geotechnical Data of Fouled Ballast**

No.	Percent Gravel	Percent Sand	Percent Fines	D <sub>10</sub> (mm)	D <sub>50</sub> (mm)	C <sub>c</sub>	C <sub>u</sub>	F <sub>1</sub> (%)	G <sub>s</sub>
SP-22	85.3	14.4	0.3	1.69	27.5	8.33	17.8	15	2.64
SP-35	76.8	22.7	0.5	0.558	24.9	3.72	50.3	24	2.64
SP-50	66.7	32.7	0.6	0.315	8.60	1.86	75.2	34	2.64
SP-60	60.2	39.0	0.8	0.248	7.33	2.07	39.0	41	2.64
SW-35	79.8	19.9	0.3	1.45	24.8	1.50	19.9	21	2.63
SW-50	71.1	28.4	0.5	0.699	17.2	1.47	34.6	29	2.62
SW-60	65.3	34.1	0.6	0.602	7.63	2.60	15.5	35	2.62
SM-35	74.4	19.5	6.1	0.217	24.8	8.41	132	32	2.63
SM-50	63.4	27.9	8.7	0.105	9.84	1.56	226	45	2.62
SM-60	56.0	33.5	10.5	0.0653	6.86	1.06	142	54	2.62
ML-35	68.4	12.3	19.2	0.0172	24.9	14.4	1670	51	2.66
ML-50	54.9	17.6	27.4	0.00774	9.60	0.0592	3080	73	2.67
ML-60	45.9	21.2	33.0	0.00577	1.77	0.0697	1650	87	2.67
SC-SM-35	70.9	15.0	14.1	0.00151	24.8	72.9	1910	43	2.65
SC-SM-50	58.4	21.5	20.1	0.00737	9.58	2.58	3240	62	2.65
SC-SM-60	50.1	25.8	24.2	0.00531	4.78	1.07	1850	74	2.66
CL1-35	68.9	11.7	19.4	0.00478	24.9	98.2	6015	51	2.62
CL1-50	55.5	16.7	27.7	0.00242	9.54	0.345	9864	72	2.62
CL1-60	46.6	50.1	33.3	0.00176	2.85	0.0464	5402	87	2.61
CL2-35	68.8	10.7	20.5	0.00418	24.8	101	6880	52	2.61
CL2-50	55.4	15.2	29.4	0.00203	9.65	0.188	1170	74	2.60
CL2-60	46.5	18.3	35.2	0.00140	2.58	0.0270	6800	89	2.59

**Table A.8: Geotechnical Data of Clean Ballast**

$\gamma_{d,max}$ (pcf)	$\gamma_{d,min}$ (pcf)	$e_{max}$	$e_{min}$	G <sub>s</sub>
97.4	83.0	0.985	0.691	2.64

### *GSD Curves for Theoretical Fouled Ballast Specimens*

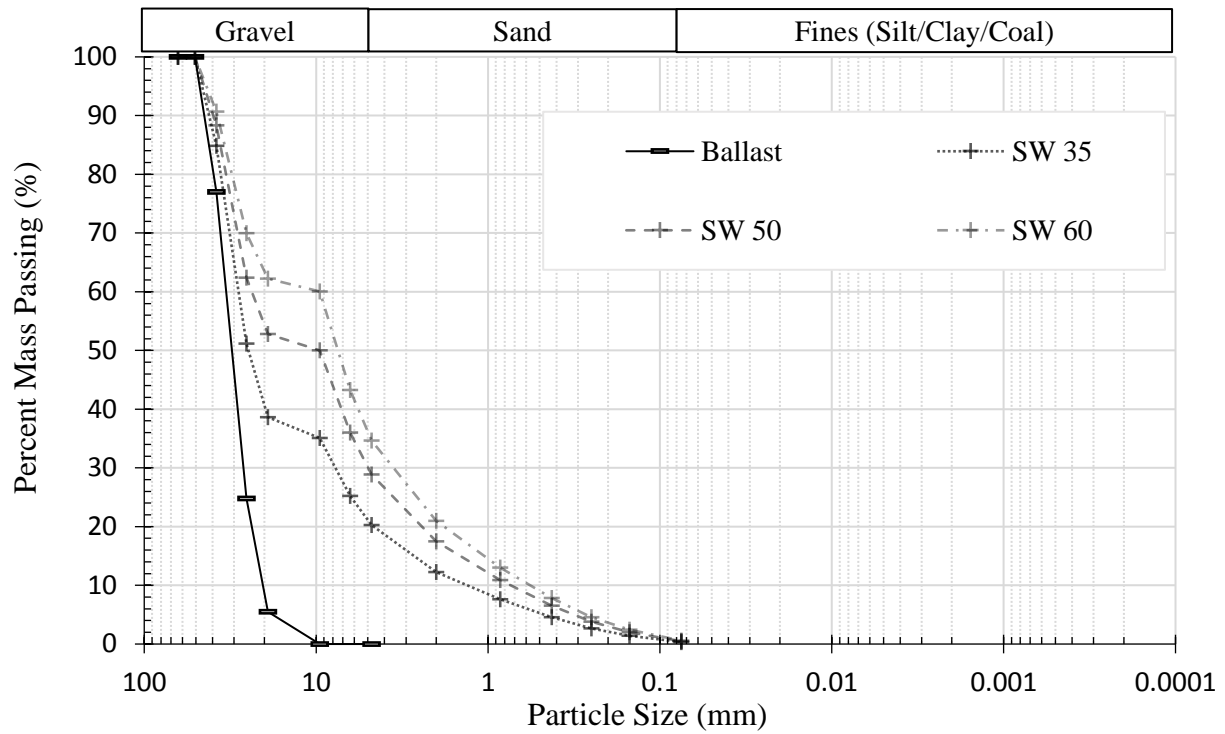


**Figure A.17: GSD of Theoretical SW Fouled Ballast Specimens.**

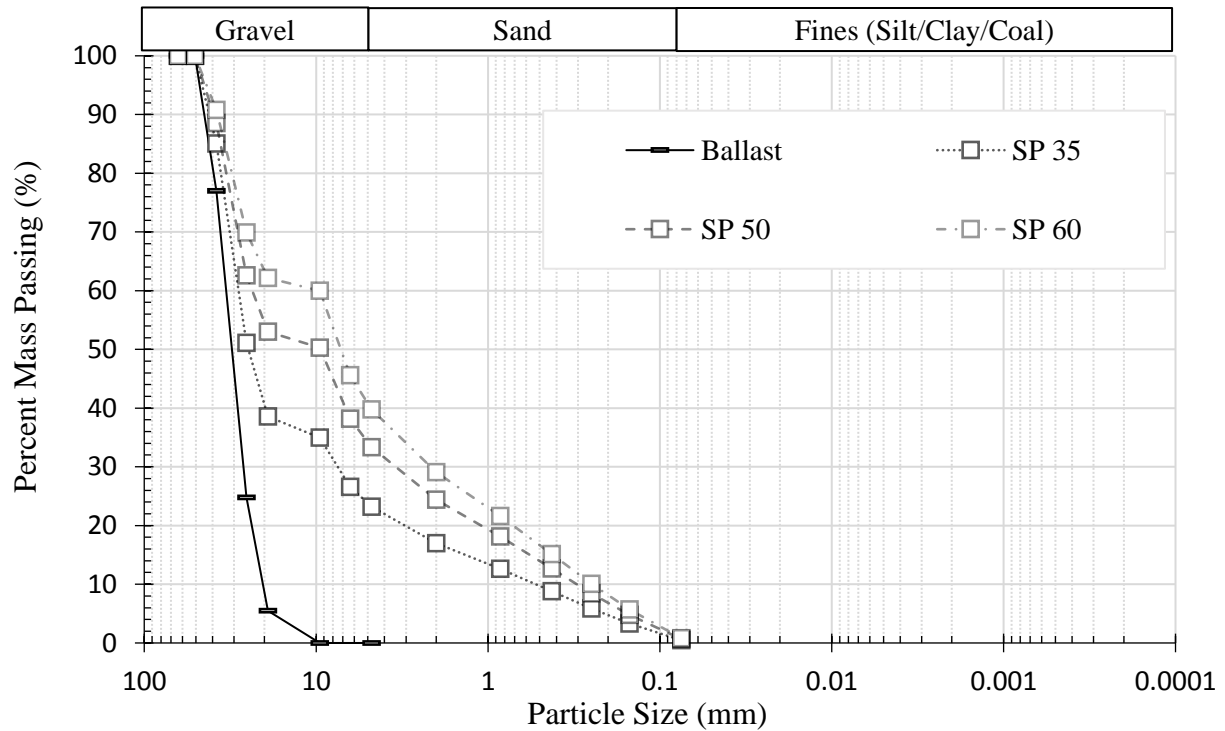


**Figure A.18: GSD of Theoretical SP Fouled Ballast Specimens.**

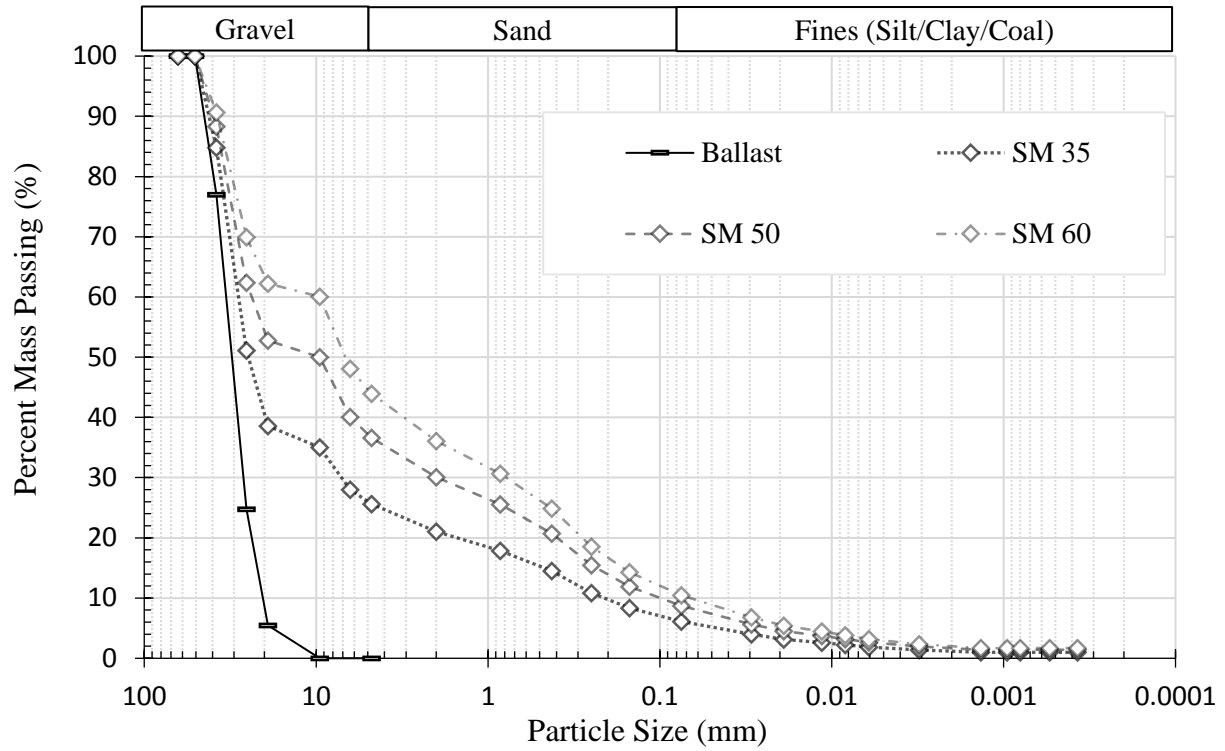


Figure A.19: GSD of Theoretical SM Fouled Ballast Specimens.

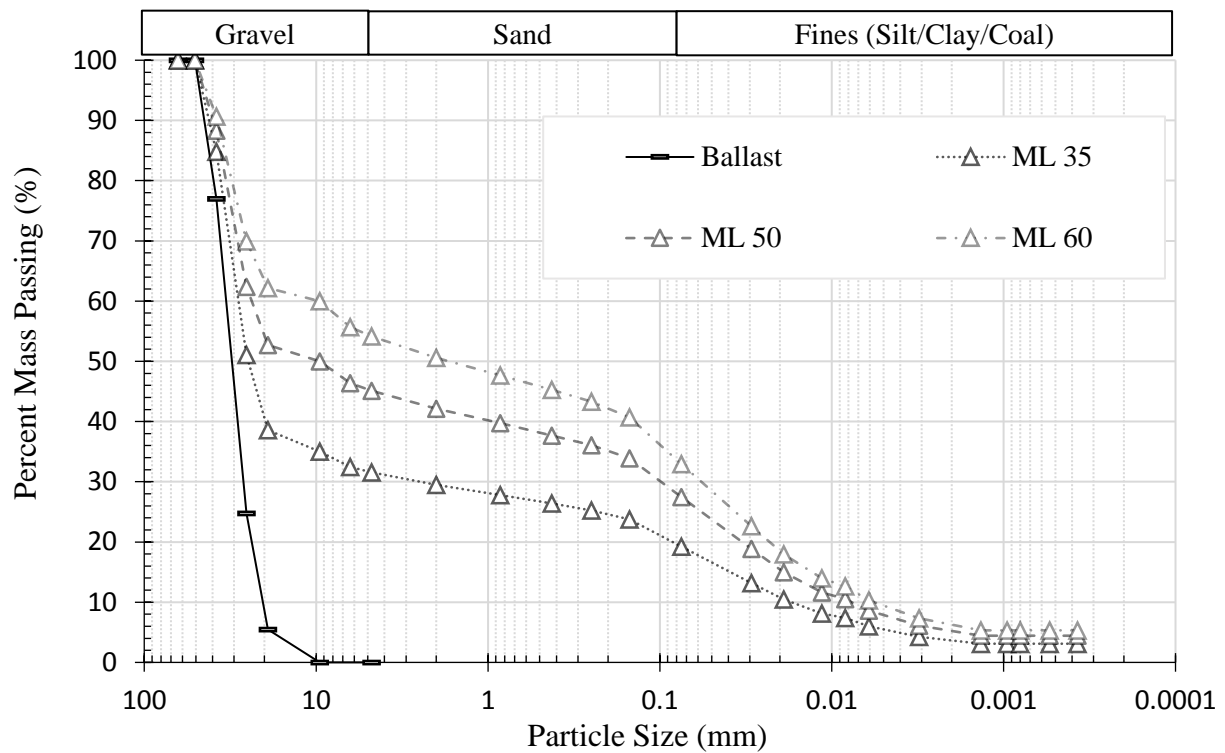
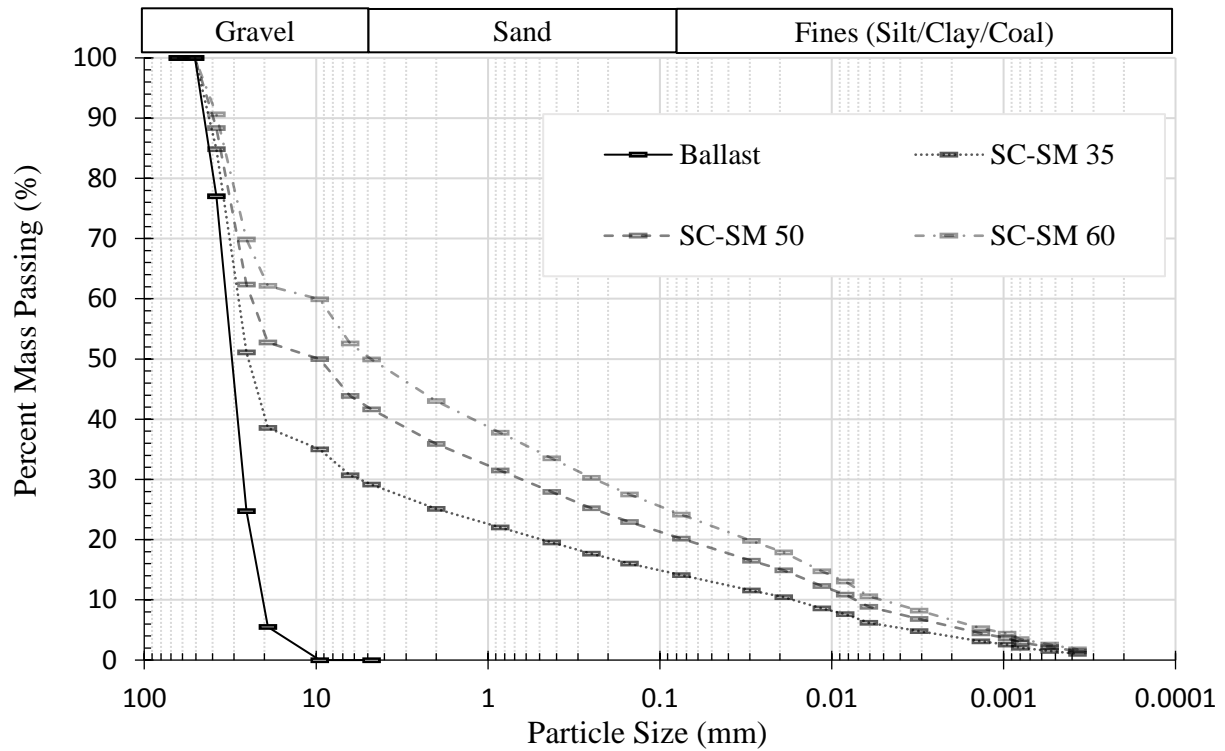
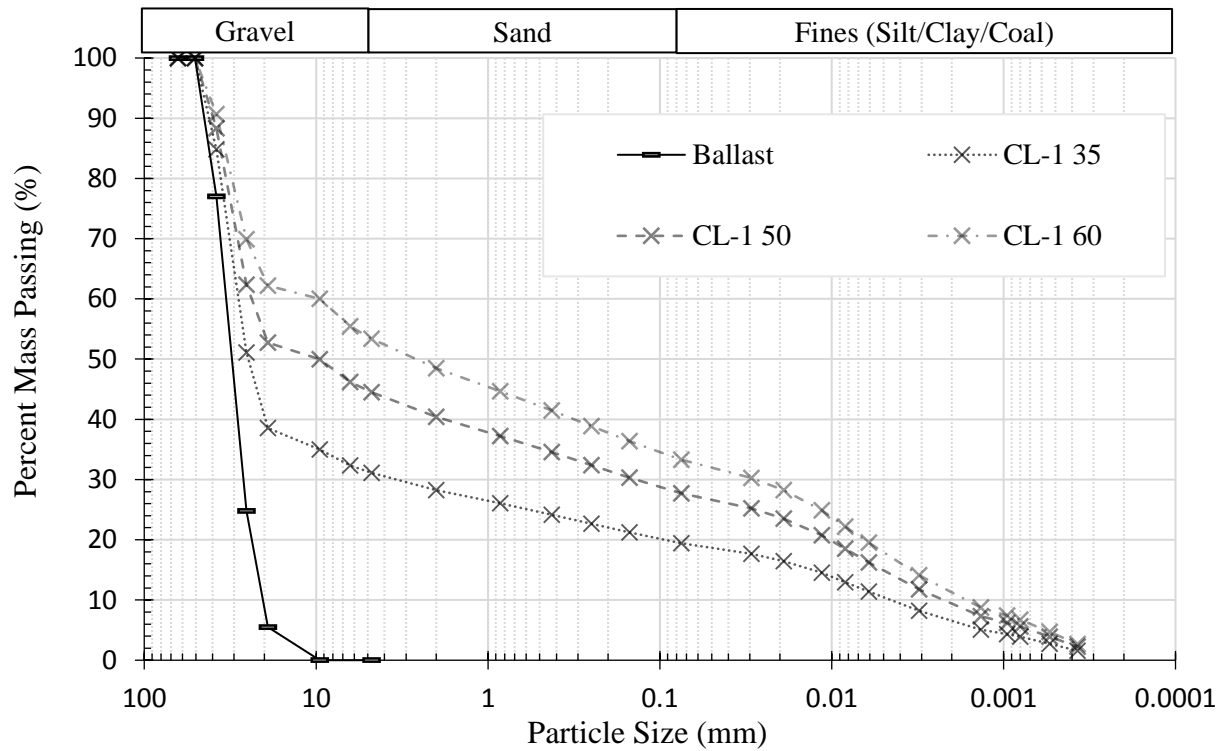


Figure A.20: GSD of Theoretical ML Fouled Ballast Specimens.



**Figure A.21: GSD of Theoretical SC-CM Fouled Ballast Specimens.**



**Figure A.22: GSD of Theoretical CL-1 Fouled Ballast Specimens.**

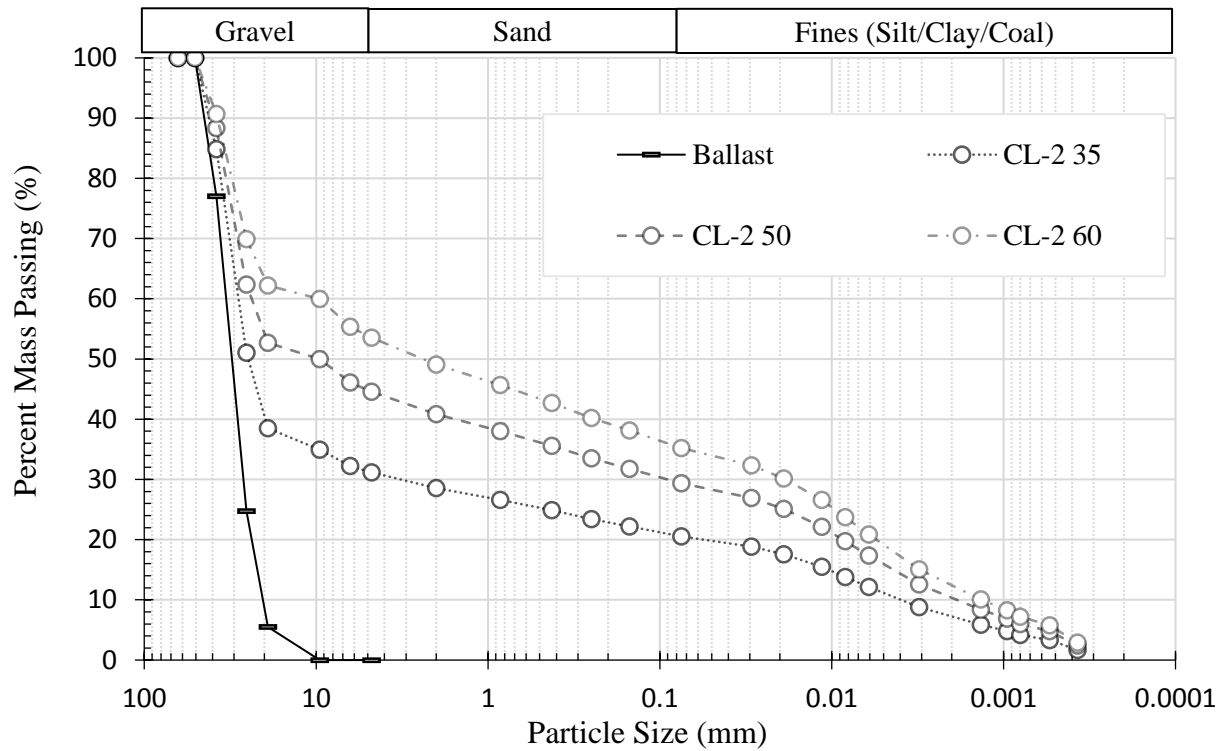


**Figure A.23: GSD of Theoretical CL-2 Fouled Ballast Specimens.**

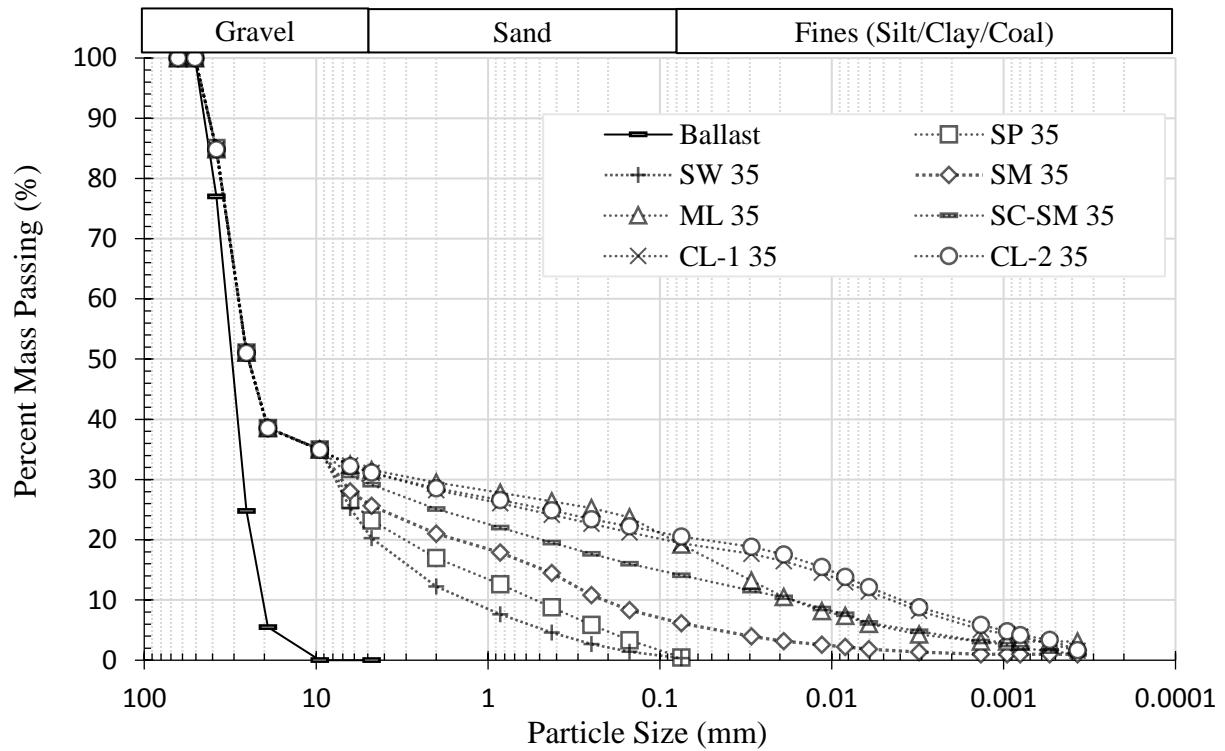


**Figure A.24: GSD Summary of 35% Fouled Ballast Specimens.**

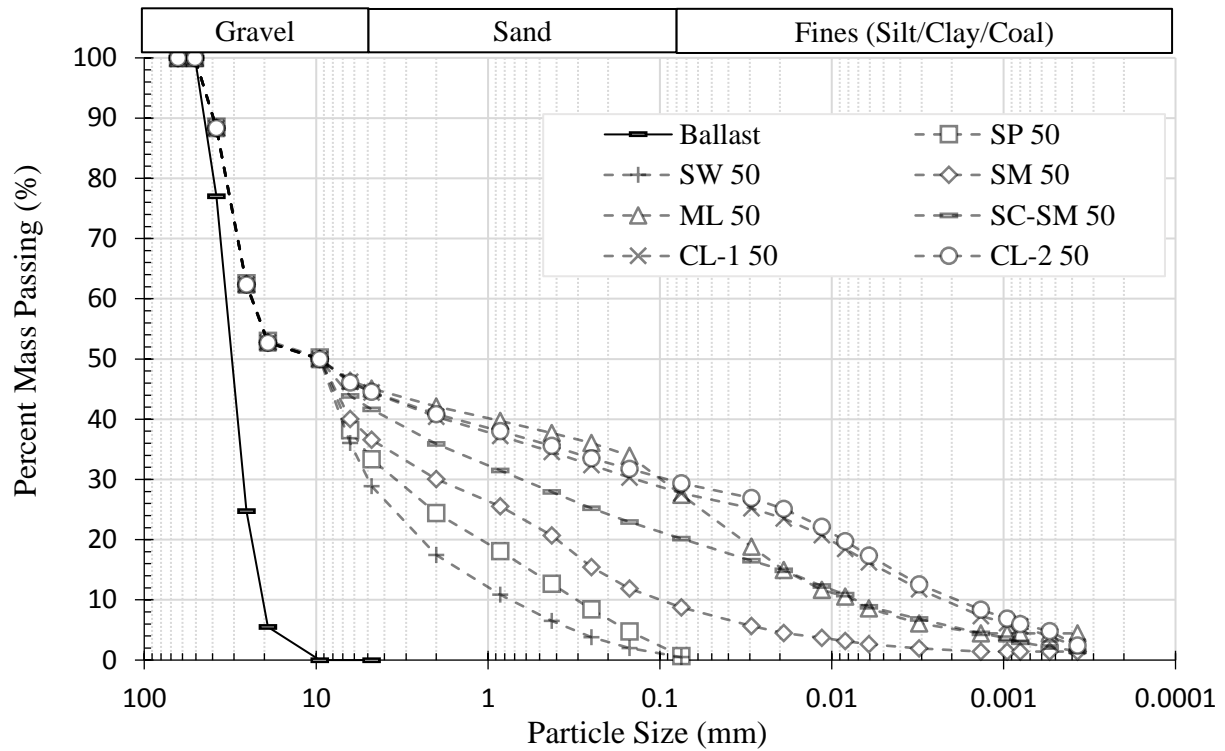


**Figure A.25: GSD Summary of 50% Fouled Ballast Specimens.**

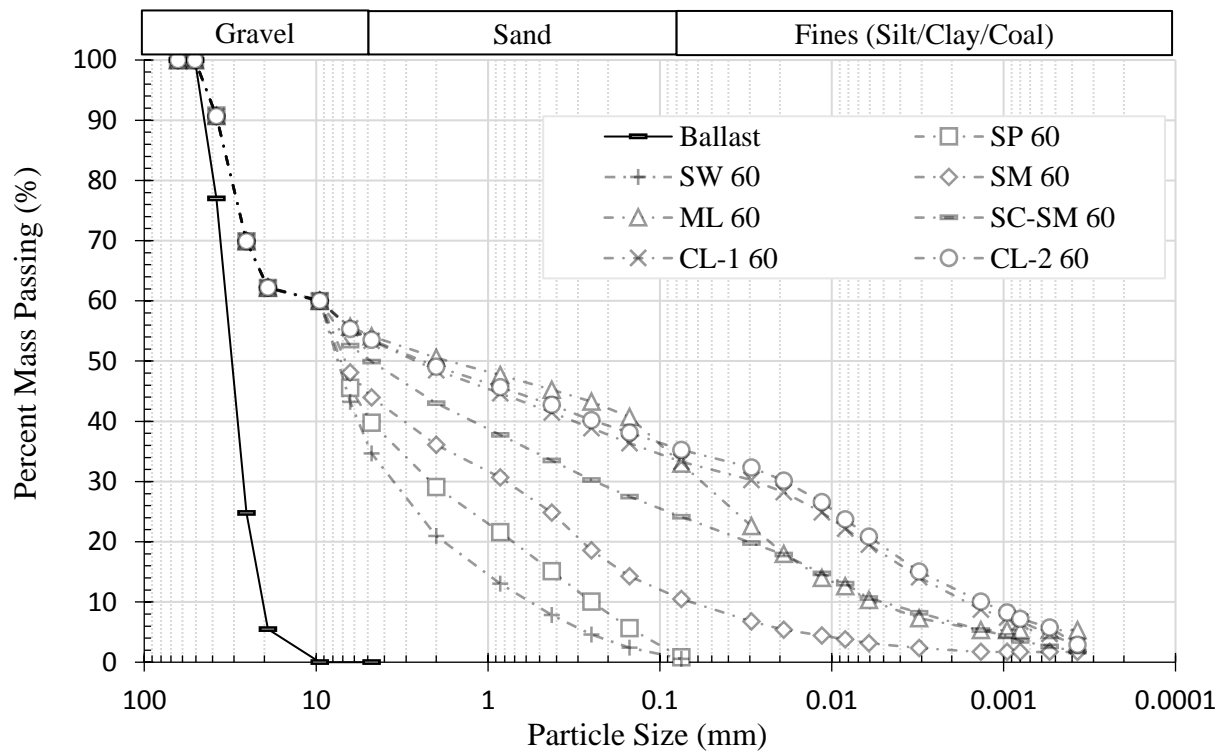


**Figure A.26: GSD Summary of 60% Fouled Ballast Specimens.**



### *Bouwer-Rice Coefficients and Unsaturated Characteristics of Fouled Ballast*

**Table A.9: Calculated Bouwer-Rice Correction Coefficients ( $V_R$ ) for Predicting Fouled Ballast SWCCs from Fouling Material SWCCs**

Fouling Condition (% Passing 3/8-inch sieve)	Contain no coal dust.				Contain coal dust.		
	SW	SP	SM	ML	SC-SM	CL-1	CL-2
<b>60</b>	0.700	0.700	0.693	0.702	0.703	0.703	0.716
<b>50</b>	0.608	0.612	0.600	0.610	0.613	0.612	0.627
<b>35</b>	0.456	0.456	0.447	0.458	0.460	0.459	0.475

**Table A.10: Hydraulic and Specimen Parameters of Theoretical Fouled Ballast Specimens**

Specimen Name	$\theta_r$	$\theta_s$	$\alpha(cm^{-1})$	n	m	$\rho_{d,fb} \left( \frac{g}{cm^3} \right)$	$\rho_{d,f} \left( \frac{g}{cm^3} \right)$	VCI
<b>SW 35</b>	0.03	0.15	0.238	1.98	0.496	2.21	1.66	1.00
<b>SW 50</b>	0.04	0.20				2.06	1.66	1.00
<b>SW 60</b>	0.04	0.23				1.97	1.66	1.00
<b>SP 35</b>	0.03	0.16	0.128	2.26	0.557	2.21	1.70	1.00
<b>SP 50</b>	0.04	0.22				2.07	1.70	1.00
<b>SP 60</b>	0.04	0.25				1.98	1.70	1.00
<b>SM 35</b>	0.03	0.16	0.0587	2.61	0.616	2.25	1.75	1.00
<b>SM 50</b>	0.04	0.21				2.11	1.75	1.00
<b>SM 60</b>	0.05	0.25				2.03	1.75	1.00
<b>ML 35</b>	0.06	0.17	0.00492	1.82	0.451	2.20	1.68	1.00
<b>ML 50</b>	0.07	0.23				2.06	1.68	1.00
<b>ML 60</b>	0.09	0.26				1.97	1.68	1.00
<b>SC-SM 35</b>	0.09	0.20	0.0130	3.50	0.714	2.19	1.67	1.00
<b>SC-SM 50</b>	0.10	0.23				2.04	1.67	1.00
<b>SC-SM 60</b>	0.10	0.24				1.96	1.67	1.00
<b>CL-1 35</b>	0.07	0.16	0.124	3.50	0.714	2.19	1.67	1.00
<b>CL-1 50</b>	0.09	0.22				2.05	1.67	1.00
<b>CL-1 60</b>	0.10	0.25				1.96	1.67	1.00
<b>CL-2 35</b>	0.08	0.18	0.0022	1.61	0.379	2.13	1.57	1.00
<b>CL-2 50</b>	0.10	0.24				1.97	1.57	1.00
<b>CL-2 60</b>	0.11	0.28				1.87	1.57	1.00

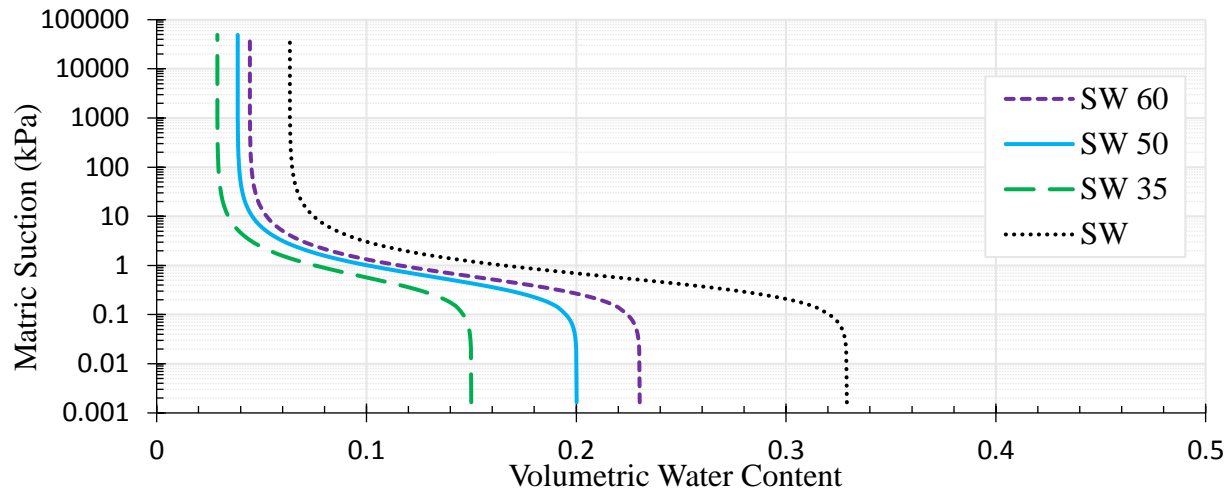


**Figure A.27: Predicted SWCCs for SW Fouled Ballast Specimens.**

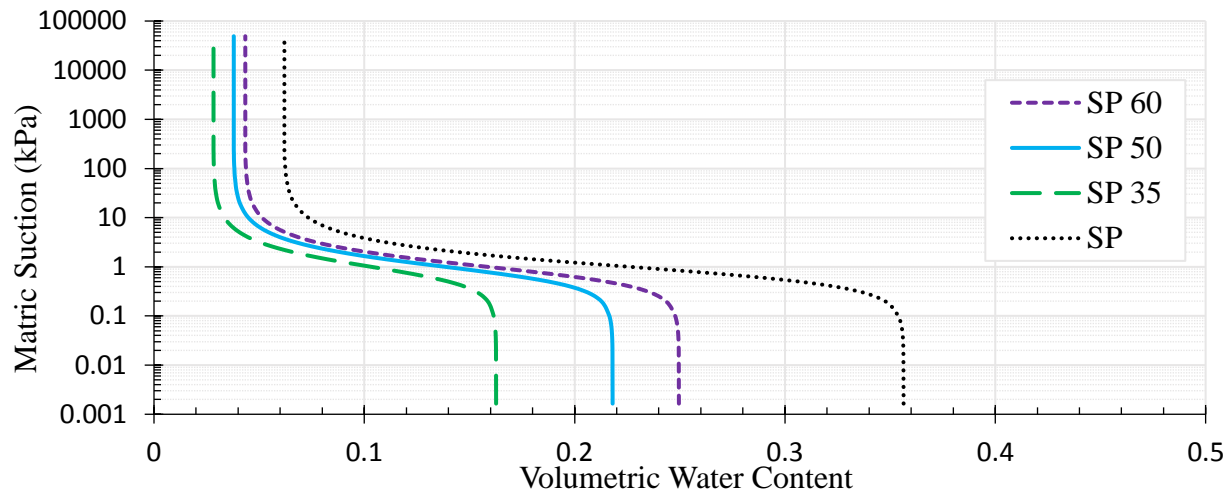


**Figure A.28: Predicted SWCCs for SP Fouled Ballast Specimens.**

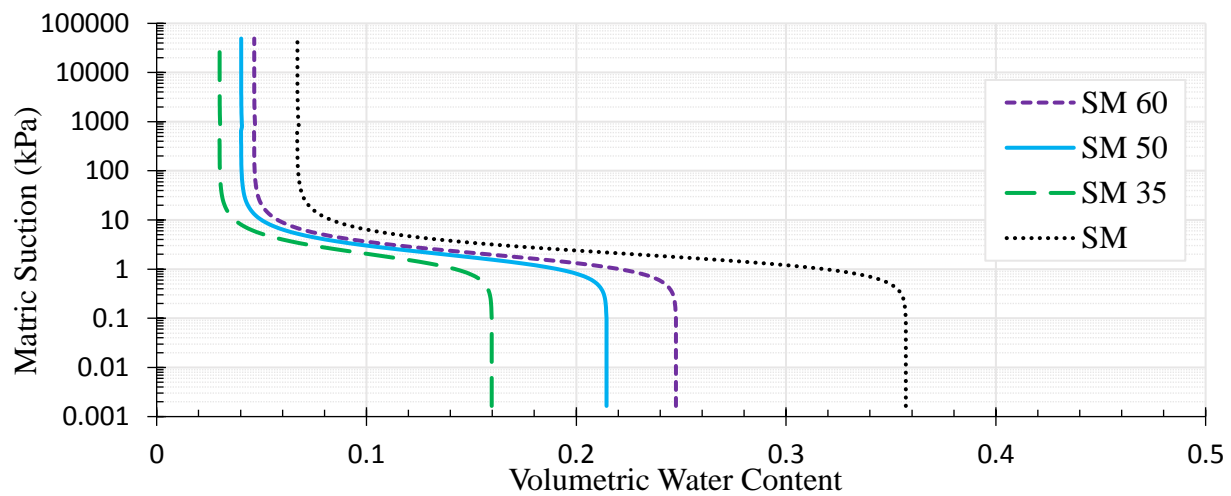


**Figure A.29: Predicted SWCCs for SM Fouled Ballast Specimens.**

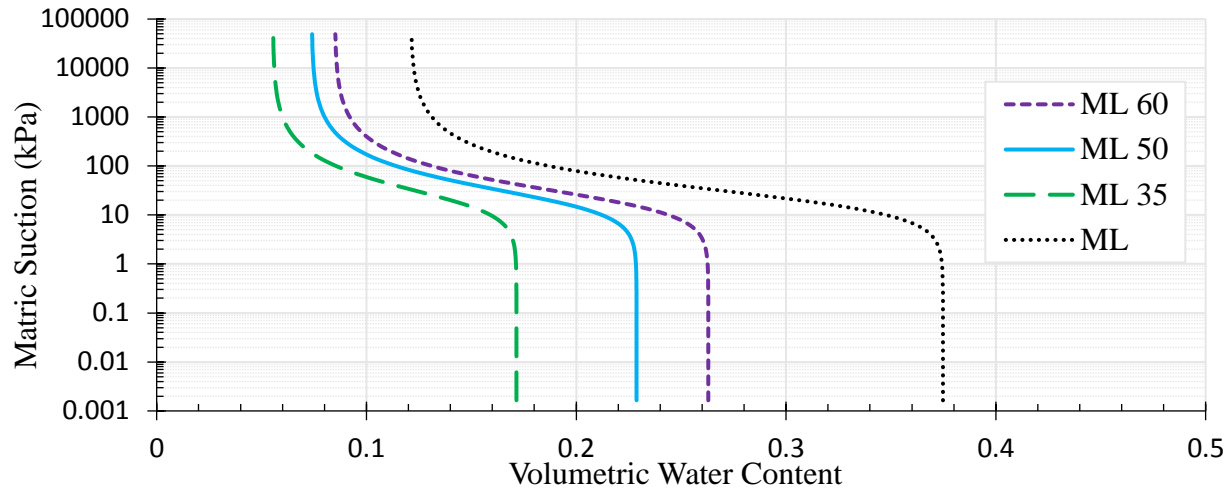


**Figure A.30: Predicted SWCCs for ML Fouled Ballast Specimens.**

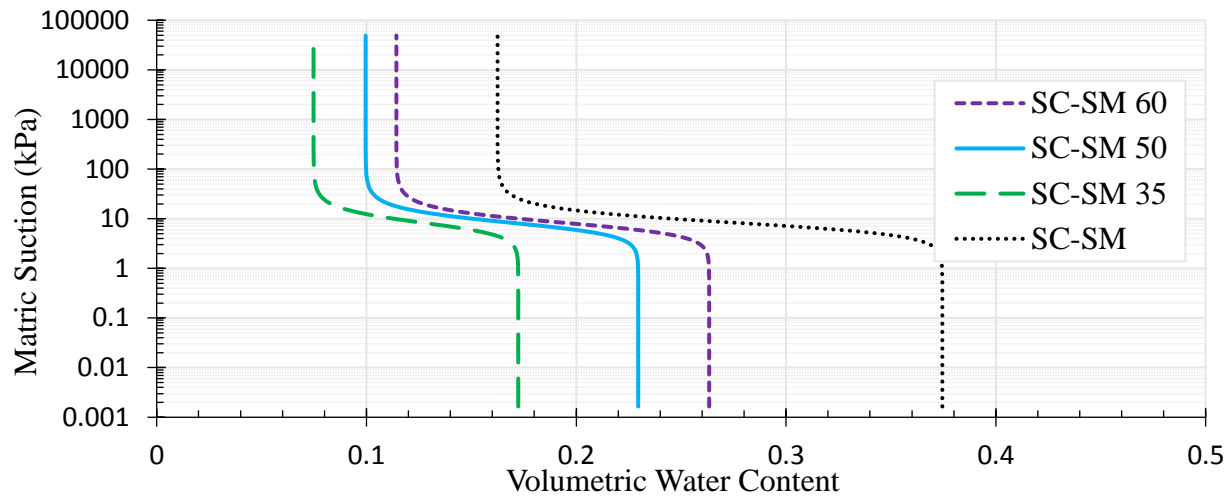


**Figure A.31: Predicted SWCCs for SC-SM Fouled Ballast Specimens.**

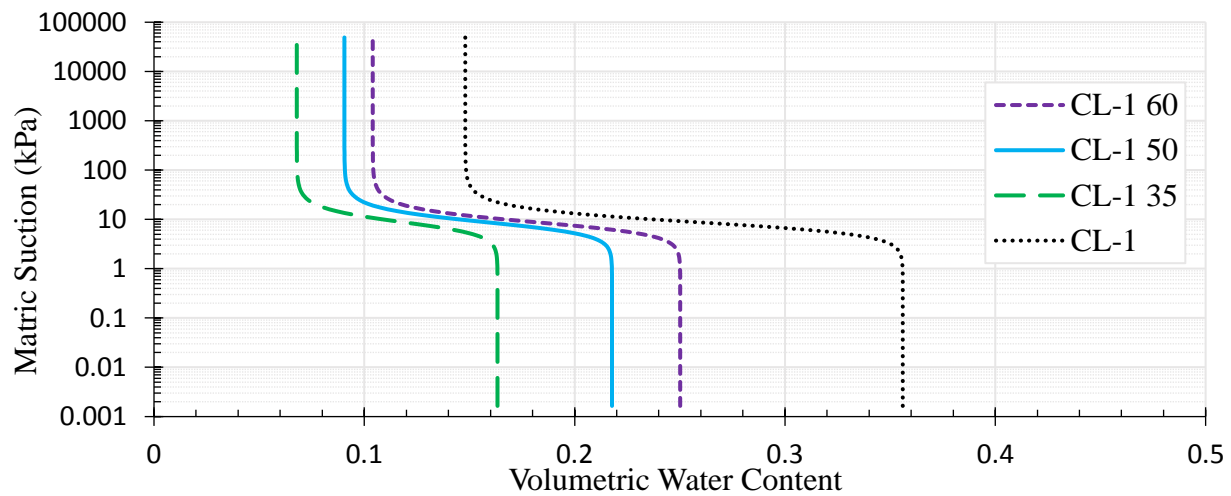


**Figure A.32: Predicted SWCCs for CL-1 Fouled Ballast Specimens.**

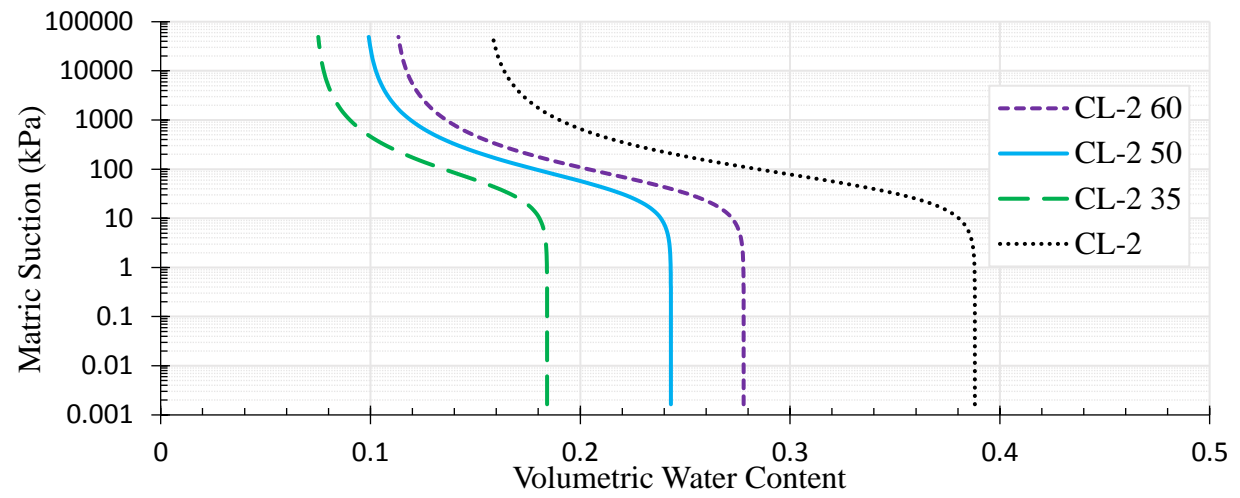


**Figure A.33: Predicted SWCCs for CL-2 Fouled Ballast Specimens.**

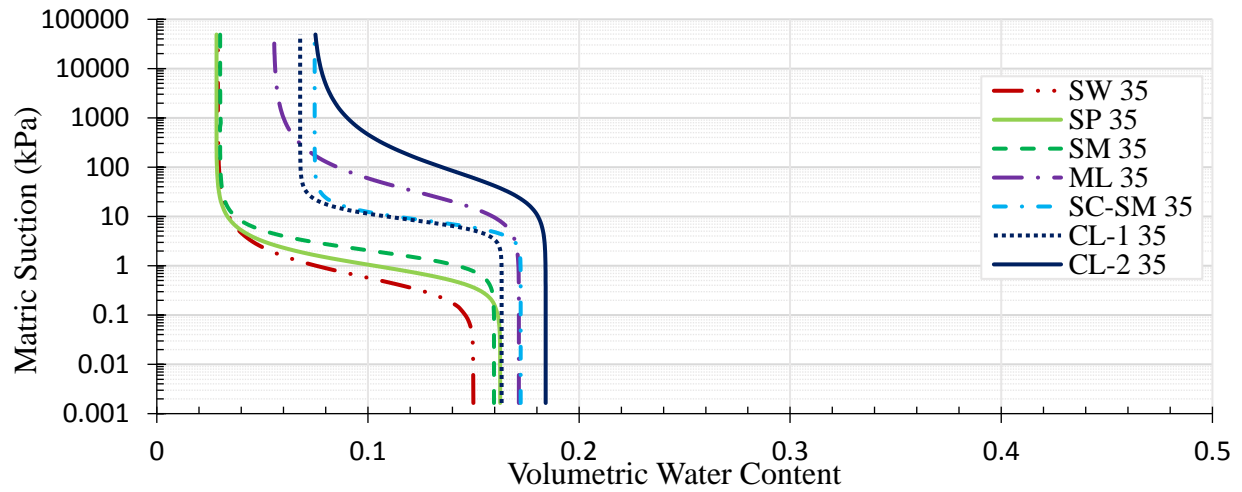


**Figure A.34: SWCC Summary for 35% Fouled Ballast Specimens.**

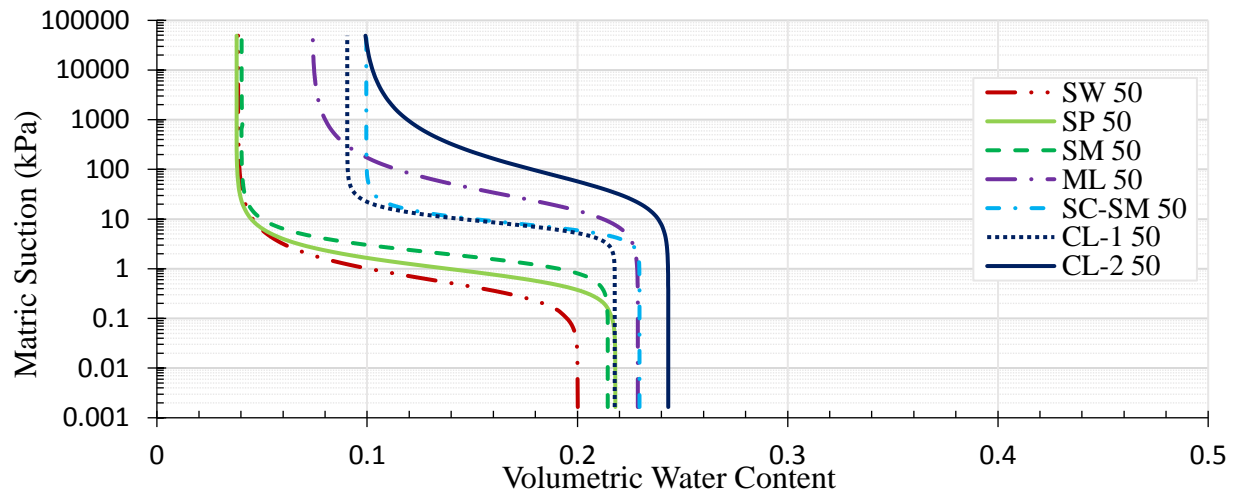


**Figure A.35: SWCC Summary for 50% Fouled Ballast Specimens.**

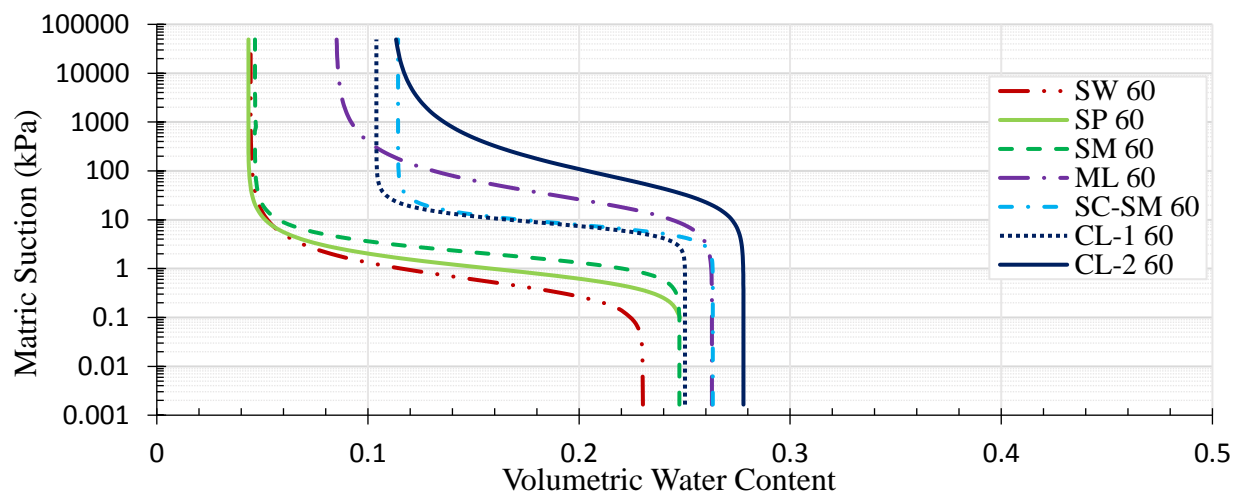


**Figure A.36: SWCC Summary for 60% Fouled Ballast Specimens.**

### A.3 Fouled Ballast in the Large TRIM Device

Table A.11: Large TRIM Specimen Properties

Specimen Name	% Passing 3/8-inch sieve	F1	VCI	Density (g/cm <sup>3</sup> )	Porosity (%)	G <sub>s</sub>
SP	100	-	-	1.74	34	2.64
SP 50	50	36	100	1.94	26	2.64
SP 22	22	15	65	1.94	27	2.64

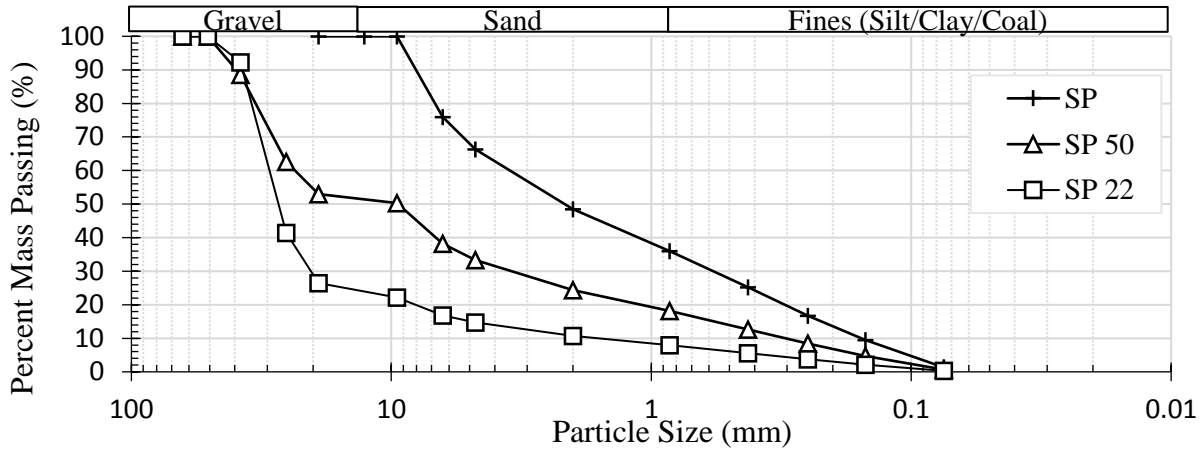


Figure A.37: GSD of Fouled Ballast Tested in the Large TRIM.

Table A.12: van Genuchten Hydraulic Parameters with Model Statistics

Specimen Name	$\theta_r$	$\alpha$ (1/cm)	n	m	$K_s$ (cm/s)	R <sup>2</sup>	SSQ
SP	0.045	0.147	2.21	0.548	1.80E-03	1.00	2.44E-03
SP 50	0.054	0.122	2.97	0.664	1.14E-02	1.00	1.11E-03
SP 22	0.020	0.287	3.50	0.714	8.98E-03	0.99	9.95E-03

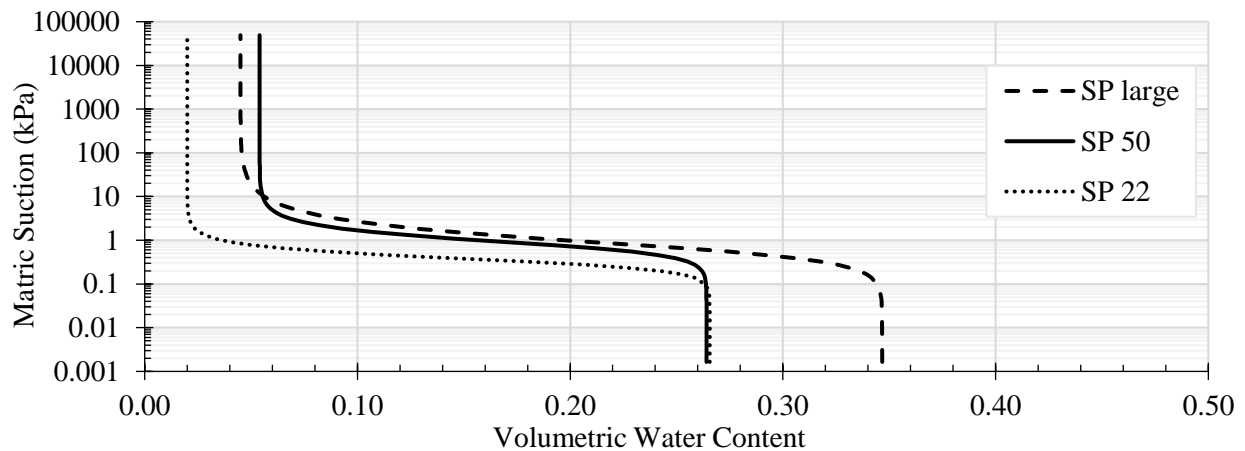


Figure A.38: SWCCs of Specimens Tested using the Large TRIM.

## A.4 Example Solution of Richards' Equation using a Backwards Implicate Finite Difference Method

### INTRODUCTION

The transient water release and imbibition method (TRIM) (Wayllace and Lu, 2012) is a testing and modeling process designed to quickly determine the drying and wetting soil water characteristic curves (SWCC) and hydraulic conductivity functions (HCF). This example focuses on the drying state. During the testing portion of the method, the two-step transient cumulative water outflow is measured for a soil sample. Then the transient cumulative outflow data is used as an objective function in an inverse modeling process. (Wayllace and Lu, 2012) The modeling process involves three general steps:

- 1) First, a model is selected (i.e., van Genuchten-Mualem) and the fitting parameters (i.e.,  $n$ ,  $m$ , and  $\alpha$ ) of the model are estimated. The van Genuchten-Mualem models for the SWCC and the HCF are defined as:

$$\theta(h) = \theta_r + \left[ \frac{\theta_s - \theta_r}{1 + (\alpha|h|)^n} \right]^m \quad \text{Equation A.1}$$

$$K(h) = K_s \frac{[1 - |\alpha h|^{n-1}(1 + |\alpha h|^n)^{-m}]^2}{(1 + |\alpha h|^n)^{m/2}} \quad \text{Equation A.2}$$

where  $\theta(h)$  is the SWRC,  $\theta_r$  is the residual volumetric water content,  $\theta_s$  is the saturated volumetric water content,  $n$ ,  $m$ , and  $\alpha$  are empirical fitting parameters,  $h$  is the suction head,  $K(h)$  is the HCF, and  $K_s$  is the saturated hydraulic conductivity (van Genuchten 1980).

- 2) Second, the transient/cumulative outflow curve is estimated using a finite difference approximation of Richards' Equation:

$$\frac{\delta\theta(h)}{\delta h} \frac{\delta h}{\delta t} = \frac{\delta}{\delta z} \left[ K(h) \frac{\delta h}{\delta z} \right] - \frac{\delta K(h)}{\delta z} \quad \text{Equation A.3}$$

where  $\theta(h)$  is the SWRC,  $h$  is the suction head,  $t$  is time,  $z$  is depth into the soil (oriented positive downward), and  $K(h)$  is the HCF.

- 3) Third, the error between the measured transient outflow curve and the estimated transient outflow curve are calculated (e.g., root mean squared error).

These three steps are executed iteratively, and the fitting parameters are optimized after each iteration reducing the error between the estimated and measured data.

The objective of this document is to describe the second step of the TRIM modeling process through an example solution of Richards' equation. The text begins with the application of one method (the backward difference method) to Richards' equation. Then boundary conditions (which describe the TRIM test) are defined and followed by a discretized model domain. Next, the numerical models' linear equations are defined, and the hydraulic properties of an example soil specimen listed. Lastly, the model solution is shown.

## **THEORY**

**Backward Implicit Approximation.** Finite difference methods approximate ordinary and partial derivatives using the truncated Taylor series of each derivative. The dropped portion of the truncated series becomes an error between the approximated and exact solution, but this error can be made sufficiently small. Several differencing methods exist (e.g., classic explicit, backward implicit, and Crank-Nicolson methods); the backward implicit method was used in this example because the initial physical conditions of the transient outflow curve to be modeled are well known. The following describes how to prepare Richards' equation for application of this method.

First, the left-hand side of Richards' equation (i.e., Eq. [3]) can be simplified by rewriting it in terms of Specific Capacity. Specific capacity is the derivative of the SWCC in respect to head, and expressed as



$$C(h) = \frac{nm. \alpha (\theta_s - \theta_r)}{(1 + (|\alpha h|)^n)^{m+1}} |\alpha h|^{n-1} \quad \text{Equation A.4}$$

where  $C(h)$  is the specific capacity,  $n, m$ , and  $\alpha$  are empirical fitting parameters,  $\theta_r$  is the residual volumetric water content,  $\theta_s$  is the saturated volumetric water content, and  $h$  is the suction head.

The rewritten form of Richards' equation becomes:

$$C(h) \frac{\delta h}{\delta t} = \frac{\delta}{\delta z} \left[ K(h) \frac{\delta h}{\delta z} \right] - \frac{\delta K(h)}{\delta z} \quad \text{Equation A.5}$$

where  $C(h)$  is the specific capacity,  $h$  is the suction head,  $t$  is time,  $z$  is depth into the soil (oriented positive downward), and  $K(h)$  is the HCF. In this form, Richards equation can be solved by approximating each side of the equation. The left-hand side is a first order partial derivative; a first order backward difference approximation of the left-hand side of Eq. [5], centered at  $(z_i, t^{n+1})$ , yields

$$C_i^{n+1} \left( \frac{h_i^{n+1} - h_i^n}{\Delta t} \right) \quad \text{Equation A.6}$$

where  $i$  serves as an index for discrete depths ( $z$ ) and  $n$  serves as an index for discrete times ( $t$ );  $C$  is still specific capacity,  $h$  is head, and  $\Delta t$  is the time step. The right-hand side of Eq. [5] is a second order partial derivative. A second order backward difference approximation for the right-hand side of Eq. [5] yields

$$\frac{K_{i+1/2}^{n+1}(h_{i+1}^{n+1} - h_i^{n+1}) - K_{i-1/2}^{n+1}(h_i^{n+1} - h_{i-1}^{n+1})}{(\Delta z)2} - \frac{K_{i+1/2}^{n+1} - K_{i-1/2}^{n+1}}{\Delta z} \quad \text{Equation A.7}$$

where  $K(h)$  is the HCF and  $\Delta z$  is the depth increment.

There are two obstacles presented in these approximations. First,  $C^{n+1}$  and  $K^{n+1}$  terms are functions of an unknown parameter to be solved for ( $h^{n+1}$ ), making equations [6] and [7] non-linear. If both terms are forced back to the previous time step, i.e., from  $C^{n+1}$  to  $C^n$  and from  $K^{n+1}$

to  $K^n$ ; then both approximations become linear; this step is called explicate linearization therefore this example uses the backward implicate approximation with explicate linearization. The second obstacle is found in equation [7] where the hydraulic conductivity must be evaluated in a half space: at  $i + 1/2$  and  $i - 1/2$ . This obstacle is overcome by approximating the hydraulic conductivity in the half space as the average of the hydraulic conductivity at the upper and lower indexed depths (i.e., the trapezoidal rule):

$$K_{i+1/2}^n = \frac{K_{i+1}^n + K_i^n}{2}, \quad K_{i-1/2}^n = \frac{K_i^n + K_{i-1}^n}{2} \quad \text{Equation A.8}$$

The general expression of the backward implicit approximation of Richards' equation with explicit linearization is:

$$\frac{C_i^n}{\Delta t} (h_i^{n+1} - h_i^n) = \left[ \frac{K_{i+1}^n + K_i^n}{2(\Delta z)^2} ((h_{i+1}^{n+1} - h_i^{n+1}) - \Delta z) - \frac{K_i^n + K_{i-1}^n}{2(\Delta z)^2} ((h_i^{n+1} - h_{i-1}^{n+1}) - \Delta z) \right] \text{Eq. A.9}$$

In computational form, Eq. [9] is

$$-b_i h_{i-1}^{n+1} + (a_i + b_i + c_i) h_i^{n+1} - c_i h_{i+1}^{n+1} = a_i h_i^n + (b_i - c_i) \Delta z \quad \text{Equation A.10}$$

where

$$a_i = \frac{C_i^n}{\Delta t}, \quad b_i = \frac{K_i^n + K_{i-1}^n}{2(\Delta z)^2}, \quad c_i = \frac{K_{i+1}^n + K_i^n}{2(\Delta z)^2} \quad \text{Equation A.11}$$

**Boundary Conditions.** Boundary conditions are selected to model the physical conditions of the soil specimen at the start and throughout the duration of the TRIM testing process. At the start of the test, the stone and the soil in the TRIM cell are fully saturated with water. The head distribution in the saturated sample is known to be linear and can follow one of two suites:

$$h_0(z) = z - L \text{ [cm]}; \quad h_0(z) = z \text{ [cm]} \quad \{z > 0, \quad t = 0\} \quad \text{Equation A.12}$$

where  $h_0$  is initial head,  $z$  is depth (oriented positive down), and  $L$  is total length of the system.

Throughout the testing phase of the experiment, no liquid water enters the surface of the sample, but water drains out of the sample through base plate. Therefore, a zero-liquid-flux

condition is maintained at the surface. This physical phenomenon is modeled by a Neumann boundary condition at the surface of the domain ( $z = 0$ ); that boundary condition is defined as:

$$q(0, t) = \left[ -K(h) \frac{\delta h}{\delta z} + K(h) \right] = q_a \left\{ q_a = 0 \left[ \frac{cm^3}{cm^2 s} \right] \quad t > 0 \right\} \quad \text{Equation A.13}$$

where  $K(h)$  is the HCF,  $\delta h$  is the change in head,  $\delta z$  is the change in depth,  $q_a$  is liquid-flux, and  $t$  is time.

Also, throughout the testing phase two-steps of constant pneumatic head are applied at the surface of the sample to force water to drain from the system. Nasta et. al (2011) showed that the pneumatic pressure (which is applied at the top of the soil) can be simulated as a suction head applied at the base of the system, a Dirichlet boundary condition at the bottom of the domain:

$$h(L, t) = -|h_b| \left\{ \begin{array}{ll} h_b = 0.00 [cm] & t < 10 [sec] \\ h_b = 6.12 [cm] & 10 [sec] \leq t < 1 [day] \\ h_b = 2550 [cm] & 1 [day] \leq t \leq 5 [days] \end{array} \right\} \quad \text{Equation A.14}$$

where  $L$  is the length of the domain,  $h_b$  is the applied suction head at the bottom of the system, and  $t$  is time.

## DISCRETIZATION SCHEME

With a Neumann condition at the surface and the Dirichlet condition at the bottom, the following mesh (figure 1) with  $m + 1$  equally spaced nodes discretize the depth of the sample in the  $z$ -direction. The use of  $m + 1$  nodes allows for convenient indexing of  $z_i$ :  $i = 1, 2, \dots, m + 1$  where  $z_1 = 0$  and  $z_{m+1} = L$ . The distance between nodes is given by  $\Delta z = \frac{L}{m}$ . In the  $t$ -direction,  $t_1$  corresponds to the start time of the model; that is to say  $t_1 = 0$ . The end time or time of interest is denoted as  $t_{N+1}$ . Closed points in Figure A.39 denote known values; open points denote values to be solved for.

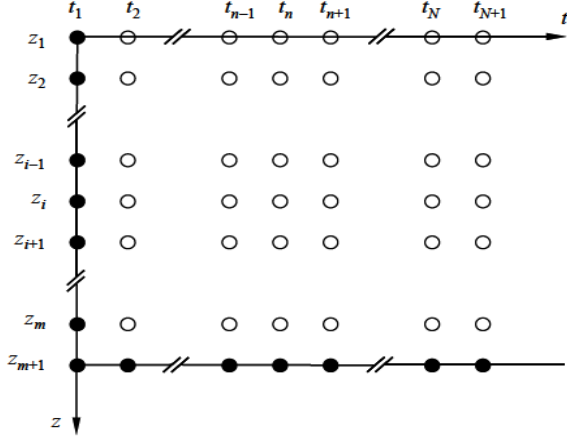


**Figure A.39: Node diagram for the Backward Implicit Finite Difference solution of Richards' equation with a Neumann boundary condition at the surface and Dirichlet boundary condition at the bottom.**

Note. Reprinted from “Node Diagram Summary Sheet”, by Kluitenberg 2019

## MODEL

**Model Equations.** After adding the boundary conditions to Richards' equation and after simplifying, the m-linear equations are

$$h_2^{n+1} - h_1^{n+1} = \Delta z \quad \text{Equation A.15}$$

$$-b_i h_{i-1}^{n+1} + (a_i + b_i + c_i) h_i^{n+1} - c_i h_{i+1}^{n+1} = a_i h_i^n + (b_i - c_i) \Delta z \quad \text{Equation A.16}$$

$$\{i = 2, 3, \dots, m-1\}$$

$$-b_m h_{m-1}^{n+1} + (a_m + b_m + c_m) h_m^{n+1} = a_m h_m^n + (b_m - c_m) \Delta z + c_m h_b \quad \text{Equation A.17}$$

where

$$a_i = \frac{c_i^n}{\Delta t}, \quad b_i = \frac{K_i^n + K_{i-1}^n}{2(\Delta z)^2}, \quad c_i = \frac{K_{i+1}^n + K_i^n}{2(\Delta z)^2} \quad \{i = 1, 2, \dots, m-1\};$$

$$c_m = \frac{K_{lower}^n + K_m^n}{(\Delta z)^2} \quad \text{Equation A.18}$$

In this example, two methods are used to calculate cumulative bottom flux. The first method is derived from Darcy's Law:

$$Q1 = \Delta t \sum_{n=1}^{N+1} \left( -K_{lower} \frac{\delta h}{\delta z} + K_{lower} \right) \quad \text{Equation A.19}$$

where  $\Delta t$  is the time step,  $K_{lower}$  is the hydraulic conductivity at the base of the HAE porous stone, and  $\frac{\delta h}{\delta z}$  is the hydraulic gradient at the base of the HAE porous stone.

The second method integrates the change in volumetric water content over the sample's depth:

$$Q2 = -\frac{\Delta z}{2}(\theta_1^{N+1} - \theta_1^1) + \Delta z \sum_{i=2}^m (\theta_i^{N+1} - \theta_i^1) + \frac{\Delta z}{2}(\theta_{lower}^{N+1} - \theta_{lower}^1) \quad \text{Equation A.20}$$

where  $\Delta z$  is the distance between nodes,  $\theta_1^{N+1}$  and  $\theta_1^1$  are the final and initial volumetric water contents at the surface of the system,  $\theta_i^{N+1}$  and  $\theta_i^1$  are final and initial volumetric water contents at discrete depths throughout the sample excluding the boundaries, while  $\theta_{lower}^{N+1}$  and  $\theta_{lower}^1$  are the final and initial volumetric water contents at the base of the HAE porous stone. A weighting term of  $\frac{1}{2}$  is applied to the surface and base volumetric water contents because each of these nodes represents half the depth of the interior nodes.

Richards' equation was solved using a mesh of 100 nodes ( $m = 100$ ) and a time-step of 0.5 seconds ( $\Delta t = 0.5$ ). Results are calculated and plotted for end-times ( $t_{N+1}$ ) of *5 sec., 1 minute, 1 hour, 5 hours, ½ day, 0.999 days (end of first step), 1 day, 1.05 days, 1.15 days, 1 ½ days, 2.9 days, and 5 days*. The 'end of first step' refers to the end of the first step in the two-step testing procedure of the TRIM. The last evaluation time was set to five days because the experimental data used for this example was from a 5-day test.

The hydraulic properties listed in Table 1 were determined by the author using the TRIM: saturated hydraulic conductivity ( $K_s$ ), air entry and the van Genuchten fitting parameters  $\alpha$ ,  $n$ , saturated volumetric water content ( $\theta_s$ ), and residual volumetric water content ( $\theta_r$ ). The van Genuchten fitting parameter  $m$  in Eq. [1] was approximated using  $m = 1 - 1/n$  (e.g., van Genuchten, 1980).

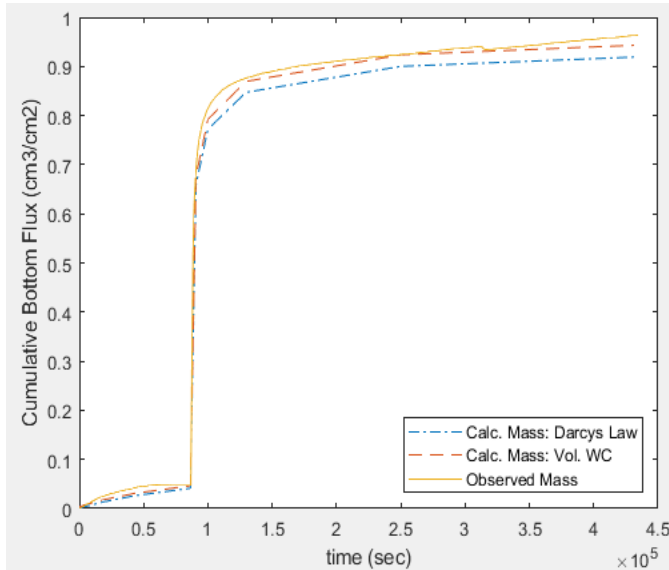
**Table A.13: Material Properties and van Genuchten Fitting Parameters**

Material Name	$Ks$ [cm/s]	Air Entry [cm H <sub>2</sub> O]	$\alpha$ [1/cm]	$n$	$\theta_s$	$\theta_r$
HAE Stone	$5.80 \text{ E}^{-8}$	3060	$1.50 \text{ E}^{-4}$	7.00	0.340	0.0700
Silty Sand	$5.10 \text{ E}^{-4}$	0.00	$5.89 \text{ E}^{-2}$	2.60	0.357	0.0670

The air entry value for the soil was assumed to be 0.00 cm of H<sub>2</sub>O. The length of the example sample was 3.8 centimeters in total: 3.4 centimeters of soil and 0.4 centimeters of HAE porous stone; therefore,  $L = 3.8$  centimeters. Model results follow.

## SOLUTION

Figure A.40 shows the end solution: cumulative bottom flux derived from Darcy's Law plotted as a blue dot-dash line and that from the volumetric water content plotted as an orange dashed line. The measured flux is plotted as a solid yellow line. The model captures both lobes of the measured curve (i.e., the outflow from each of the two constant pneumatic heads applied to the sample).

**Figure A.40: Predicted and Measured Cumulative Bottom Flux vs Time.**

In the inverse modeling process, a similar numerical approximation is executed to estimate the cumulative outflow, compare it to the measured outflow data, and then optimize the van Genuchten fitting parameters until the model results closely resemble the measured curve.

## REFERENCES

- Kluitenberg G.J. (2019) "Node Diagram Summary Sheet." AGRON 916 (Advanced Soil Physics). Kansas State University.
- Nasta, P., Huynh, S., & Hopmans, J. W. (2011). "Simplified multistep outflow method to estimate unsaturated hydraulic functions for coarse-textured soils." *Soil Science Society of America Journal*, 75(2), 418-425.
- Van Genuchten, M. T. (1980). "A closed-form equation for predicting the hydraulic conductivity of unsaturated soils 1." *Soil science society of America journal*, 44(5), 892-898.
- Wayllace, A. and Lu, N. (2012). "A Transient Water Release and Imbibitions Method for Rapidly Concurrent Measurements of Soil-water Retention, Hydraulic Conductivity, and Suction Stress Functions Under Drying and Wetting Conditions." *Geotech. Test. J.*, 35:1, 40-54.